Title
Technologies for Blood Diagnostics

Author
Waldeisen, John Robert

Publication Date
2012

Peer reviewed|Thesis/dissertation

Technologies for Blood Diagnostics

by

John Robert Waldeisen

A dissertation submitted in partial satisfaction of the

requirements for the degree of

Joint Doctor of Philosophy
with University of California, San Francisco

in

Bioengineering

in the

Graduate Division

of the

University of California, Berkeley

Committee in charge:

Professor Luke P. Lee, Chair
Professor Zev J. Gartner
Professor Lee W. Riley

Fall 2012

Abstract

Technologies for Blood Diagnostics

by

John Robert Waldeisen

Joint Doctor of Philosophy in Bioengineering
with University of California, San Francisco

University of California, Berkeley

Professor Luke P. Lee, Chair

For over three decades, the lateral flow assay (LFA) has remained the diagnostic gold standard for immunodetection. In the developed world, the diverse capabilities of these assays is relatively unknown. However in resource-limited settings, LFAs are the best diagnostic tool a clinician currently has other than a microscope to diagnose disease. Although most diseases are treatable and preventable, three diseases alone are responsible for killing more than 5 million people each year: HIV, malaria, and tuberculosis (TB). A devastating lack of diagnostic accessibility in the developing world prohibits accurate diagnosis leading to poor therapeutic administration of drugs on-hand and the increased incidence of drug resistance. Even here in the U.S., the dissemination of broad-spectrum antibiotics has led to the emergence of virulent strains of drug-resistant sepsis and mortality rates have spiked to greater than 35-50%.

This dissertation is part of an endeavor to alleviate the health disparities that are prevalent throughout our world. A recently realized mechanism for fluid actuation, degas-driven fluid flow, is applied for the development of point-of-care devices. The mechanism of degas-driven fluid flow is similar to capillary action, as the material properties of the device inherently determine fluidic actuation. However, larger fluid volumes can be controlled and advance fluidic logic can be programed, allowing the adaption of molecular diagnostic assays for pathogenic biomarker detection. Here, a 1D Fickian model of degas-driven fluid flow is present that is capable of predicting fluid movement. The understanding learned from this model is then applied for the development of polymeric point-of-care microfluidic diagnostic devices. Three specific diagnostic devices are discussed. The first is a blood sample preparation device capable of extracting nucleic acid and protein biomarkers for the simultaneous detection of HIV, malaria, and TB. Detection of TB is demonstrated on-chip with isothermal loop-mediated amplification. The second device is a hybrid LFA that employs sedimentation-based plasma separation, powered by degas-driven fluid flow, to assay for elevated levels of anti-phospholipid IgM antibodies in blood. This device is intended for the monitoring of patient response to TB drug therapy in resource-limited settings. Finally, the third device is intended for the self-monitoring of patients on anticoagulation prophylaxes.

The device simultaneously measures hematocrit in addition to the INR value thus enabling the recognition of asymptomatic hemorrhage, an often-fatal side effect common to anticoagulant therapy. All devices are capable of naked-eye visual readout eliminating the need for external equipment.

Next, the disassembly of colloidal-based nanoparticle assemblies is optimized for the visual naked-eye detection of biomolecules on microfluidic devices. The cleavage of the nanoassemblies disengages the plasmon coupling between nanoparticles and shifts the observed dark field scattered light from orange to green. The integration of this detection scheme is incorporated for point-of-care biorecognition. Finally, the dissertation concludes with the presentation of the real-time PCR antibiogram for diagnosing drug-resistant sepsis. This method combines universal phenotypic susceptibility testing with the rapid diagnostic capabilities of PCR. Detection, susceptibility testing, minimum inhibitory concentration determination, and identification are achieved in less than 24 hours.

In summary, several technologies for performing blood diagnostics at the point-of-care and in the clinical diagnostic laboratory are introduced. The ideas presented in this dissertation are an effort to transform point-of-care testing by enabling the early detection of disease and mitigating health inequalities across the world.

"OF ALL THE FORMS OF INEQUALITY,
INJUSTICE IN HEALTH CARE
IS THE MOST SHOCKING AND INHUMANE."

DR. MARTIN LUTHER KING JR., 1966

† To my Parents †

DESPITE STRUGGLES WITH
THEIR OWN EDUCATION,
PUSHED ME TO COMPLETE MINE

TABLE OF CONTENTS

CHAPTER 1: THE STATE OF POINT-OF-CARE

1.1 Introduction…….. 1
1.2 Organization of Dissertation…… 4
1.3 References…… 4

CHAPTER 2: SIMULATION OF DEGAS-DRIVEN FLUID FLOW

2.1 Abstract…….....…….…… 7
2.2 Introduction…….....…….…….. 7
2.3 Mechanism and Applications of Degas-driven Fluid Flow……..... 8
2.4 The Need for a Predictive Model……..…… 10
2.5 Theory……..…… 10
2.6 Simulation Results……..…….. 13
2.7 The Influence of Material Permeability…..…….. 13
2.8 Parameter Analysis of Degas-driven Devices……..…….. 15
2.9 Model Validation……..…….. 19
2.10 Conclusion……...…….. 20
2.11 Acknowledgements……...…… 21
2.12 References……...…….. 21

CHAPTER 3: UNIVERSAL BLOOD SAMPLE PREPARATION DEVICE

3.1 Abstract……..……..…….. 25
3.2 Introduction……..…….. 25
3.3 Sedimentation-based Microfluidic Blood Fractionation……..…….. 29
3.4 Electrochemical Lysis of Pathogenic Cells/Virons in Blood…….…….. 35
3.5 Integration and Mass Manufacturability of Devices……..…….. 36
3.6 Biomarker Detection…..……..... 38
3.7 Conclusion and Future Directions..……..... 42
3.8 Acknowledgements……...…… 42
3.9 References……...……...…….. 43

CHAPTER 4: BLOOD COAGULATION CHIP FOR INR VALUE AND HEMATOCRIT DETERMINATION

4.1 Abstract……..……..…….. 48
4.2 Introduction……..…….. 48
4.3 The Blood Coagulation Chip……..……..….. 51
4.4 Prototype Design and Fabrication…..……..... 53
4.5 Results and Discussion……..…… 54
4.6 Conclusion……..…… 56
4.7 Acknowledgements……...…… 56
4.8 References……...……...…….. 56

CHAPTER 5: HYBRID LATERAL FLOW ASSAY TO MONITOR TUBERCULOSIS PATIENT RESPONSE

5.1 Abstract……..……..…….. 58

5.2 Introduction…….. 58
5.3 The Hybrid Lateral Flow Assay…….. 59
5.4 Analysis of Anti-phospholipid Antibodies in Patient Samples…….. 63
5.5 Conclusion…….. 64
5.6 Acknowledgements…….. 64
5.7 References…….. 65

CHAPTER 6: A CORE-SATELLITE NANOASSEMBLED SUBSTRATE FOR COLORIMETRIC BIOMOLECULAR DETECTION

6.1 Abstract…….. 67
6.2 Introduction…….. 67
6.3 Substrate Assembly…….. 70
6.4 Scattering Properties of Gold Nanoparticles…….. 71
6.5 Results and Discussion…….. 72
6.6 Determining the Optimal Core-Satellite Geometry…….. 74
6.7 Comparison with Mie Theory Simulations…….. 76
6.8 Determination of Proteolytic Enzyme Kinetics…….. 78
6.9 Future Directions…….. 82
6.10 Conclusion…….. 83
6.11 Acknowledgements…….. 83
6.12 References…….. 83

CHAPTER 7: A REAL-TIME PCR ANTIBIOGRAM FOR DRUG-RESISTANT SEPSIS

7.1 Abstract…….. 87
7.2 Introduction…….. 87
7.3 Experimental Overview…….. 89
7.4 The Real-time PCR Antibiogram…….. 89
7.5 Susceptibility and Minimum Inhibitory Concentration Testing…….. 91
7.6 Pan-bacterial Detection and Identification…….. 93
7.7 Comparison to Commercial Techniques…….. 94
7.8 Conclusion…….. 95
7.9 Acknowledgements…….. 95
7.10 References…….. 95

CHAPTER 8: FUTURE DIRECTIONS

8.1 Conclusion…….. 98

APPENDIX

Appendix A: Simulation of Degas-driven Fluid Flow…….. 100
Appendix B: Universal Blood Sample Preparation Device…….. 107
Appendix C: Blood Coagulation Device for INR Value and Hematocrit Determination…….. 111
Appendix D: Hybrid Lateral Flow Assay to Monitor Tuberculosis Patient Response…….. 112
Appendix E: A Core-Satellite Nanoassembled Substrate for Colorimetric Biomolecular Detection…….. 114
Appendix F: A Real-time PCR Antibiogram for Drug-resistant Sepsis…….. 123
Appendix References…….. 130

CHAPTER 1

THE STATE OF POINT-OF-CARE

1.1 INTRODUCTION

Rarely are new mechanisms of fluidic actuation discovered, however in 2004 a Japanese group at RIKEN published the first paper that utilized degas-driven fluid flow to power a microfluidic device.[1] This method, which the authors ambiguously labeled "power-free," utilizes the porous nature of a silicone commonly used in microfluidics to store vacuum and degas the channels of a microfluidic device. The autonomous creation of a pressure gradient and the mobility enabled with tether-free devices stored in vacuum packaging is a substantial improvement upon the current methods of fluid actuation for point-of-care devices. Unfortunately, the microfluidics community has overlooked this revolutionary work and only recently has this method started to be adopted by researchers.

The realization of the degas-driven fluid flow mechanism has come at a time when improvements in commercially available point-of-care devices appear to have stagnated in recent years. The limitations of capillary action and pneumatic pumping, two of the most common platforms for fluid actuation in handheld devices, have constrained technology advancement. Capillary action in particular is the workhorse method for fluid actuation in lateral flow assays (LFAs), the gold standard technique for most front-line *in vitro* diagnostic tests. Commercial LFAs are reliable, robust, easy-to-operate, and can assay for a variety of diseases and health states ranging from Unigold's HIV assay to First Response's pregnancy test. For more than three decades this technology has provided an inexpensive and adaptable means of immunoassay-based target identification in biological samples.[2] However, advanced fluid logic is not possible with this mechanism preventing integration of more complex assays. Standard diagnostic assays, such as ELISA, that are more sensitive than immunoassay require the loading of multiple reagents and wash steps that are incapable of being performed on an LFA platform. Pneumatic pumping is one approach taken by companies such as Cepheid, Micronics, and Abbott to circumvent this limitation.[3] Handheld devices such as the I-STAT (Abbott) are capable of more complex fluid handling and consequently more advanced biological assays. However, the added functionality for actuation of multiple fluids has resulted in systems that are larger and more expensive than their LFA counterpart. Other issues exist with the added complexity such as battery replacement, internal component failure, frequent calibration, data interfacing, and technician training. PCO_2, creatinine, and troponin testing failures of the I-STAT handheld device have led to the discontinuation of its use at many hospitals and contributed to the apprehension of using handheld platforms.[4,5] The adoption of two component cartridge-reader platforms has slowed, particularly in clinical diagnostic laboratories where transition is essential for market penetration. Other technologies such as CD-based centrifugal and electrokinetic

actuation are promising, but also require external platforms to enable fluid movement and analyte detection. Abaxis, a company that utilizes CD-based centrifugal microfluidics for blood diagnostics, was founded in 1989 and has had slow market growth. Thus, even with the extraordinary advancement of microfluidic component technology over the past decade, the translation of applicable devices and capabilities has been disappointing.

Herein lies the promise of utilizing degas-driven fluid flow for point-of-care device actuation. Like capillary action, this method is a passive pumping mechanism inherently determined by the material properties of the device. Thus problems associated with pneumatic actuation such as pump failure, power requirements, and operator learning are eliminated. Devices have the capacity to be self-supporting and disposable to minimize biohazard exposure. Additionally, degas-driven fluid flow allows fluidic movement at the μL volumes necessary for common biomolecular assays that are currently performed manually. Preliminary results have demonstrated sequential loading of multiple reagents and alternative vacuum-assisted methods to stabilize transiently decaying flow rates are promising. In comparison with capillary action and pneumatic actuation, degas-driven fluid flow is a middle ground between both mechanisms, eliminating cumbersome external pumps while facilitating the passive actuation of multiple reagents.

Point-of-care diagnostics has recently become a very attractive research area. This explosion of interest is due in part to the injection of funding by organizations such as Defense Advanced Research Projects Agency (DARPA), the Bill & Melinda Gates Foundation, and the highly publicized Qualcomm Tricorder X Prize competition. The Bill & Melinda Gates Foundation may be one of the greatest contributors to the newfound interest the microfluidic community has for point-of-care diagnostics. In 2005, the Foundation awarded $450M to 43 proposals for a five-year grant period. Two of the community's best-known researchers, Paul Yager and George M. Whitesides, were part of this funding initiative and their work has helped bring point-of-care diagnostics to the forefront of microfluidic research today. This has been a significant change for the field. An analysis of the number of diagnostic devices published in *Lab on a Chip* over the past decade reveals how the microfluidic community failed to identify point-of-care diagnostics as an application until nearly 2007. (Fig. 1.1) Since then, the number of diagnostic device publications in *Lab on a Chip* has increased 8-10x per year. The size of this field will certainly continue to grow as more researchers recognize the influence microfluidics can have to advance diagnostic technology.

Advancements in LFA research have only recently been embraced by the microfluidic community, with significant momentum invigorated by Whitesides' conceptualization of "paper-based microfluidics."[6-10] This rejuvenation of the LFA arrives with a new perception of the platform as researchers have integrated many new technologies with the traditional LFA concept. Screen-printed electrodes have been directly integrated within microfluidic paper-based analytical devices for the determination of glucose, lactate, and uric acid levels in human serum and off-the-shelf commercial glucometers have been employed to provide quantitative amperometric analysis.[11-13] This reconceptualization has led some researchers to deviate from the

traditional linear flow path by creating three-dimensional devices based upon the principles of origami and multi-layered fabrication.[8,9,14-16] Others have incorporated LFAs directly with microfluidic finger-actuated pumps capable of delivering multiple buffers for essential dilution and wash steps.[17] Outside the point-of-care diagnostics realm, paper-based thermochromatic electronically-powered displays and piezoresistive MEMS (micro-electro-mechanical systems) force sensors may enable cheaper incorporation of technologies that have traditionally relied upon extensive microfabrication processes.[18,19] In light of these revolutionary advances to the LFA, fluid actuation depends upon the same workhorse as it did in the past: the mechanism of capillary action.

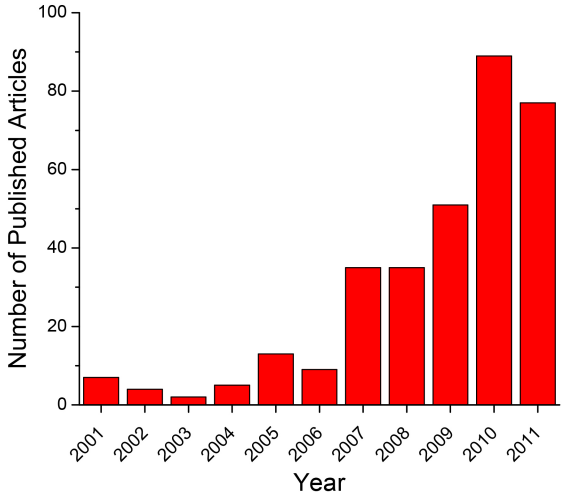

Figure 1.1: The explosion of interest in microfluidic point-of-care devices is evident by the number of published articles in *Lab on a Chip* over the past decade.

Point-of-care diagnostics platforms other than LFAs are almost always two-component systems where the assay is performed in a cartridge and a reader platform actuates fluid flow and monitors reactions via fluorescence or electrochemical detection. The I-STAT is one example of this two-component model. Additional reader systems have been engineered for molecular diagnostic devices with advanced assay capabilities. The Gene-Z is a platform for monitoring the fluorescence during Loop-mediated Amplification (LAMP) reactions that can interface with a smartphone (iPhone).[20] Primers are dehydrated on the chip, the reaction mixture is manually loaded into the device with a pipette, and an onboard aluminum heater enables isothermal amplification. In another paper, the Qiagen Rotor-Gene 2000 was modified to interface Lab-on-a-Foil CD-based chips with the commercial thermocycling device for on-chip PCR.[21] Other groups have adapted the ESE-Quant Tube Scanner for similar purposes.[22] One of the most advanced platforms is the Samsung Blood Analyzer. This system incorporates an infrared laser so that the release of ferrowax microvalves can be controlled on a CD-based microfluidic chip. It can also perform plasma separation, reagent metering, mixing, incubation, washing, and absorbance-based detection at 10 different wavelengths to monitor several different reaction protocols.[23] A commonality amongst these reader/fluidic actuation platforms is that they will undoubtedly fail in resource-limited environments. Operator training, battery charging, calibration, cartridge storage, exposure to extreme environments, storage of extra components for repair, and price,

among many other requirements prevent such platforms from translating successfully into developing regions of the world where need is greatest.

The realization of degas-driven fluid flow has opened the possibility of eliminating the two-component model by allowing autonomous fluidic actuation without the need of a platform for fluidic actuation. Additionally, the recent development of new isothermal amplification techniques such as LAMP, cross priming amplification, and recombinase polymerase amplification, suggests that qualitative and quantitative assays may be developed without the need of a fluorometer.[24-26] The diagnostic devices developed in Chapter 3 of this dissertation have USB and SD interfaces with the vision that devices may eventually communicate and be powered by a personal computer. Thus, a median may one day be reached that merges the performance of standard assays systems with the simplicity and robustness of the LFA.

1.2 Organization of Dissertation

This dissertation begins with the development and characterization of an extensive numerical model to predict degas-driven fluid flow in microfluidic devices (Chapter 2). The understanding gained in this chapter is utilized to design diagnostic devices that employ degas-driven fluid flow in the following three chapters. Chapter 3 describes the development of a universal blood sample module that extracts pathogenic nucleic acid and protein biomarkers for infectious diseases testing. Chapter 4 explains the development of a polymeric device that monitors coagulation time and hematocrit level. Chapter 5 details the progress made on a hydrid LFA device that combines sedimentation-based plasma extraction with an LFA to monitor patient response to tuberculosis drug therapy. At this point the dissertation switches gears in Chapter 6 and explores the naked-eye detection of biomolecules using gold nanoparticle assemblies. This recognition scheme can be integrated into degas-driven devices and used to monitor specific pathways of the coagulation cascade. Chapter 7 returns to blood-based diagnostics, but at the macroscale. Here, the concept of the real-time PCR antibiogram is introduced for determining the susceptibility of drug-resistant sepsis. Finally, Chapter 8 concludes the dissertation.

1.3 References

1. Hosokawa, K., Sato, K., Ichikawa, N. & Maeda, M. Power-free poly(dimethylsiloxane) microfluidic devices for gold nanoparticle-based DNA analysis. *Lab Chip* **4**, 181–185 (2004).
2. O'Farrell, B. *Lateral Flow Immunoassay*. 1–33 (Humana Press: Totowa, NJ, 2008).doi:10.1007/978-1-59745-240-3_1
3. Chin, C. D., Linder, V. & Sia, S. K. Commercialization of microfluidic point-of-care diagnostic devices. *Lab Chip* **12**, 2118–2134 (2012).
4. Ng, V. L., Kraemer, R., Hogan, C., Eckman, D. & Siobal, M. The rise and fall of i-STAT point-of-care blood gas testing in an acute care hospital. *Am. J. Clin. Pathol.* **114**, 128–138 (2000).
5. Papadea, C. *et al.* Evaluation of the i-STAT Portable Clinical Analyzer for point-

of-care blood testing in the intensive care units of a university children's hospital. *Ann. Clin. Lab. Sci.* **32**, 231–243 (2002).
6. Martinez, A. W., Phillips, S. T., Whitesides, G. M. & Carrilho, E. Diagnostics for the developing world: microfluidic paper-based analytical devices. *Anal Chem* **82**, 3–10 (2010).
7. Lu, Y., Shi, W., Qin, J. & Lin, B. Fabrication and characterization of paper-based microfluidics prepared in nitrocellulose membrane by wax printing. *Anal Chem* **82**, 329–335 (2010).
8. Martinez, A. W., Phillips, S. T. & Whitesides, G. M. Three-dimensional microfluidic devices fabricated in layered paper and tape. *P Natl Acad Sci Usa* **105**, 19606–19611 (2008).
9. Martinez, A. W. *et al.* Programmable diagnostic devices made from paper and tape. *Lab Chip* **10**, 2499–2504 (2010).
10. Fu, E. *et al.* Enhanced sensitivity of lateral flow tests using a two-dimensional paper network format. *Anal Chem* **83**, 7941–7946 (2011).
11. Dungchai, W., Chailapakul, O. & Henry, C. S. Electrochemical detection for paper-based microfluidics. *Anal Chem* **81**, 5821–5826 (2009).
12. Nie, Z. *et al.* Electrochemical sensing in paper-based microfluidic devices. *Lab Chip* **10**, 477–483 (2010).
13. Nie, Z., Deiss, F., Liu, X., Akbulut, O. & Whitesides, G. M. Integration of paper-based microfluidic devices with commercial electrochemical readers. *Lab Chip* **10**, 3163–3169 (2010).
14. Liu, H. & Crooks, R. M. Three-dimensional paper microfluidic devices assembled using the principles of origami. *J Am Chem Soc* **133**, 17564–17566 (2011).
15. Govindarajan, A. V., Ramachandran, S., Vigil, G. D., Yager, P. & Böhringer, K. F. A low cost point-of-care viscous sample preparation device for molecular diagnosis in the developing world; an example of microfluidic origami. *Lab Chip* (2012).doi:10.1039/c1lc20622b
16. Siegel, A. C. *et al.* Foldable Printed Circuit Boards on Paper Substrates. *Adv. Funct. Mater.* **20**, 28–35 (2010).
17. Qiu, X. *et al.* Finger-actuated, self-contained immunoassay cassettes. *Biomed Microdevices* **11**, 1175–1186 (2009).
18. Siegel, A. C., Phillips, S. T., Wiley, B. J. & Whitesides, G. M. Thin, lightweight, foldable thermochromic displays on paper. *Lab Chip* **9**, 2775–2781 (2009).
19. Liu, X., Mwangi, M., Li, X., O'brien, M. & Whitesides, G. M. Paper-based piezoresistive MEMS sensors. *Lab Chip* **11**, 2189–2196 (2011).
20. Stedtfeld, R. D. *et al.* Gene-Z: a device for point of care genetic testing using a smartphone. *Lab Chip* (2012).doi:10.1039/c2lc21226a
21. Focke, M. *et al.* Microstructuring of polymer films for sensitive genotyping by real-time PCR on a centrifugal microfluidic platform. *Lab Chip* **10**, 2519–2526 (2010).
22. Lucchi, N. W. *et al.* Real-Time Fluorescence Loop Mediated Isothermal Amplification for the Diagnosis of Malaria. *PLoS ONE* **5**, e13733 (2010).
23. Lee, B. S. *et al.* Fully integrated lab-on-a-disc for simultaneous analysis of biochemistry and immunoassay from whole blood. *Lab Chip* **11**, 70–78 (2011).
24. Tomita, N., Mori, Y., Kanda, H. & Notomi, T. Loop-mediated isothermal

amplification (LAMP) of gene sequences and simple visual detection of products. *Nat Protoc* **3**, 877–882 (2008).
25. Xu, G. *et al.* Cross Priming Amplification: Mechanism and Optimization for Isothermal DNA Amplification. *Scientific Reports* **2**, – (2012).
26. Piepenburg, O., Williams, C. H., Stemple, D. L. & Armes, N. A. DNA Detection Using Recombination Proteins. *PLoS Biol* **4**, e204 (2006).

CHAPTER 2

SIMULATION OF DEGAS-DRIVEN FLUID FLOW

2.1 ABSTRACT

Degas-driven flow is a potentially revolutionary mechanism for autonomous fluid actuation in tether-free microfluidic devices. However, the absence of a comprehensive predictive model describing fluid movement will hinder the development and adoption of the method. A numerical model is presented that employs 1D Fickian diffusion to accurately determine fluid flow and channel pressure within a device. The model enables evaluation of device properties and their influence on device performance. Materials applicable to mass fabrication, such as polymethylpentene (TPX), synthetic rubber, polycarbonate, and low-density polyethylene (LDPE), have been identified as potential materials for future degas-driven devices. Channel length, channel cross-section, degassing layer thickness, and contact angle were investigated, in addition to other parameters such as initial device-packaging pressure, idle time before fluid loading, and fluid viscosity. Manipulation of these variables can create devices with predetermined loading times and flow rates that may enable the use of degas-driven flow in applications such as point-of-care diagnostics, environmental monitoring, and commercial analytical laboratories. Additionally, values for each parameter that limit utility or render a device non-functional have been recognized. We expect that a greater understanding of degas-driven flow will facilitate the development of component technology enabling advanced fluid logic for processes necessitating greater complexity.

2.2 INTRODUCTION

Significant advancements have been achieved in microfluidic component technology over the past decade, however the limited number of methods for portable fluidic actuation has restrained adoption of such progress. Thus the employment of these developments in functional, stand-alone devices has not occurred in settings beyond the microfluidic research laboratory. Specific applications, such as point-of-care clinical diagnostics, environmental monitoring, and commercial analytical laboratories, are areas primed for the translation of microfluidic technologies. However, a practical and compact method for versatile fluid actuation has remained elusive. A pumping method that would enable widespread adoption of microfluidic technology would be a power-free technique that would not require external accessories yet provide advanced fluid logic capabilities such as valving and sequential washes for the integration of biochemical assays. Degas-driven fluid flow is a method of autonomous fluid actuation that has the potential to liberate microfluidic applications requiring mobility from the prohibitive tether of external fluidic pumps.[1] Utilizing degas-driven fluid flow may be one way to enable adoption of the microfluidic component technology advanced in the past decade.

A number of power-free pumping methods have been developed for microfluidic actuation. Passive pumping techniques such as capillary-action,[2] evaporation,[3,4] droplet-based surface tension,[5] and gravity-based fluid flow[6] are well-studied phenomena with fundamental analytical equations that govern fluid movement. However, the utility of these techniques outside a microfluidic lab is greatly limited as such passive flows are not able to provide more complicated forms of fluid actuation necessary for analytical function. Capillary action, utilized in lateral flow assays, is the most common form of passive fluid manipulation, however channels can only fill once and surface irregularities may cause flow to be inconsistent in micron-size channels. Evaporation and droplet-based surface tension pumping necessitate that the device be primed beforehand and fluctuations in ambient temperature and humidity cause irregular fluid flow. Gravity-based flow requires device priming and external manipulation of the pressure head is necessary to produce advanced fluid logic steps. Additionally, a number of power-free technologies have been produced that create pressurized environments on-chip and are effective at manipulating crude, unprocessed fluids autonomously. These developments include the pressurized storage of reagents,[7] integration of vacuum capillary tubes,[8] chemical decomposition of H_2O_2 into pressurized O_2,[9] finger-actuated pumps,[10-13] and electrically-actuated micropumps.[14,15] Although promising, these mechanisms require advanced fabrication processes that are prohibitive to the cost-effective scaling and adoption of these technologies. Degas-driven fluid flow is a favorable alternative that is scalable for mass production and surpasses the shortcomings of other passive fluid flow mechanisms.

2.3 Mechanism and Applications of Degas-driven Fluid Flow

Polydimethylsiloxane (PDMS) is the workhorse material universally employed in the microfluidic community for the rapid prototyping of devices. It is also among the most permeable of all elastomers and polymers.[16,17] The mechanism of degas-driven fluid flow employs this inherent physical property of PDMS to create a local pressure gradient on-chip to drive fluid flow. (Fig. 1) The rapid diffusion of nitrogen and oxygen, coupled with the high solubility of these gases, enables PDMS to innately have gas concentrations 16.8% that of atmosphere under normal fabrication conditions.[18] The dissolved air in the bulk PDMS can be outgassed under vacuum (Fig 1b) and the evacuated device can be stored in vacuum packaging. (Fig 1c) Upon opening the packaging (Fig 1d), the device microchannels are exposed to atmosphere and air begins to permeate back into the PDMS. (Fig. 1e) If a fluid is loaded into the inlet of a device, thus sealing the dead-end channels within the device, the entrapped air is absorbed into the PDMS and the pressure within the enclosed channel begins to decrease. (Fig. 1f) This degassing process enables pressure-driven fluid flow by creating a lower pressure within the microchannel relative to atmospheric pressure. (Fig. 1g) Similar to capillary action, the mechanism of degas-driven fluid flow is inherently determined by the material properties of the device.

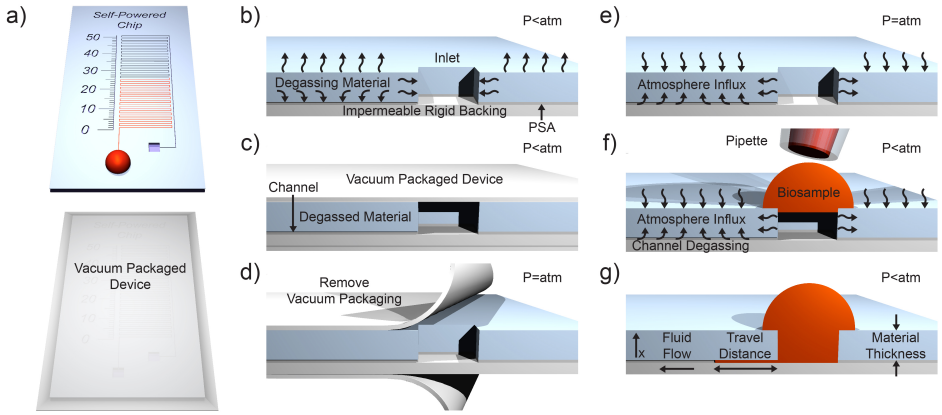

Figure 2.1: a) Schematic of a self-powered microfluidic device employed in the degas-driven flow model. The dead-end serpentine channel in the simulation has a 100 µm x 100 µm cross-section and is 1 m long. Devices can be vacuum packaged to preserve degas power for fluid actuation. b) The three-layer device can be assembled with a porous degassing layer, pressure sensitive adhesive (PSA), and an impermeable rigid backing. Fluidic channels are cut into the PSA layer. The device is outgassed and c) sealed in vacuum packaging to retain degas power. d) Upon removal of the device from vacuum packaging, e) atmosphere fluxes into the porous degassing layer. f) The introduction of the biosample into the inlet seals the fluidic channel and the pressure of the enclosed air volume decreases as the channel degasses. g) A non-steady pressure gradient establishes across the biosample and propels fluid into the degassing channel. The 1D Fickian model of diffusion is oriented in the direction of the x-axis. The relative pressure within the device channel is shown at the top right corner for each step.

Similar methods to degas-driven flow that utilize the diffusion of gas through PDMS to drive fluid flow are the channel outgas[19] and permeation pump techniques.[20] However, these approaches require external equipment since the pumping power cannot be conserved and stored on-chip as with degas-driven flow. Nevertheless, degas-driven fluid flow does have certain limitations. One drawback with degas-driven devices in comparison to conventional pumping methods (e.g. syringe, pneumatic) is that the flow rate decays as the power of the degassed chip is exhausted. This places a time constraint before flow stagnates and device function expires. Additionally, surface tension/capillary forces begin to have greater influence on fluid movement as the pressure gradient ceases, leading to flow irregularities. One option to surmount this effect is coupling capillary action with degas-driven flow to ensure complete device filling once the pressure gradient becomes exhausted. A complete analytical model describing degas-driven fluid flow is essential to evaluating the advantages and disadvantages of this technique for fluid actuation and the feasibility for its employment in the field.

The ubiquitous use of polydimethylsiloxane (PDMS) in microfluidics has enabled degas-driven fluid flow to translate smoothly as a viable means for fluid manipulation. To date, all devices that have demonstrated degas-driven fluid flow have been monolithic PDMS chips fabricated by soft-lithography. A diverse range of applications have been demonstrated with this self-powered pumping mechanism including fluorescent and nanoparticle-based DNA analysis,[1,21-23] immunoassays for C-reactive protein and prostate-specific antigen detection,[24-26] plasma extraction for whole blood analysis,[27]

modular vacuum pumps,[28,29] viscometers,[29-31] nanoliter dispensing for protein crystallization screening,[32] autonomous filling of channel junctions for electrophoretic analysis,[33,34] cell loading into microcavities,[35] and surface patterning of biomolecules for cell analysis.[36] Although a nascent technology, these demonstrations establish the versatility of degas-driven fluid flow to perform multiple applications on-chip without external equipment and the actuation of fluid flow at much faster flow-rates and with more reliability than other passive methods.

2.4 THE NEED FOR A PREDICTIVE MODEL

A predictive model that accurately describes fluid movement in degas-driven fluid flow would greatly improve chip design and device utility. Previous attempts to model degas-driven fluid flow have over-generalized Fickian mechanics[1] and relied upon corrective factors[37] to fix inaccuracies. There is a need for the development of a mechanistic model created from first principles to facilitate more complex chip design and enable advanced fluidic logic. This paper presents a numerical model that calculates fluid flow in a microchannel under the dynamic pressure gradient that occurs in degas-driven devices. The model, which applies 1D Fickian diffusion across a plane sheet, is used to investigate how geometric and material properties determine on-chip flow rates and device loading times. The simulations are validated empirically and we demonstrate how the results can be implemented for rational chip design. The findings presented in this paper correlate well with previous attempts to characterize degas-driven flow.[28,29,37]

We believe that future, commercializable degas-driven devices will be multi-laminate devices fabricated *via* roll-to-roll manufacturing, similar to the production of glucose meter strips. Therefore, we chose to model a three-layer device as shown in Fig. 1. Here, the microfluidic channels are created by sandwiching pressure sensitive adhesive (PSA) between a permeable polymer layer and an impermeable backing. It is important to note that this model can also accurately simulate the traditional monolithic devices that are fabricated from PDMS. The 1D Fickian model of diffusion employed in this study is oriented across the polymer layer, as indicated by the x-axis in Fig. 1g.

2.5 THEORY

To determine the time-dependent concentration profiles across the porous polymer membrane during degas-driven fluid flow, our model utilizes solutions for two different cases of Fick's 2nd Law:

$$\frac{\partial C}{\partial t} = D\frac{\partial^2 C}{\partial x^2} \tag{2.1}$$

The first solution is used to determine the concentration profile of the device during initial outgassing in vacuum and the subsequent influx of air during the idle time before device loading. The idle time is defined as the time period between when the chip is taken out of the vacuum packaging, thus exposing it to atmosphere, and when the inlet of the chip is sealed. The second solution applies numerical analysis to determine the pressure and fluid flow rates within the microchannel once the device is loaded.

The analytical solution for the first case, an initially constant and uniform concentration distribution C_0 across a porous degassing membrane with equal surface concentrations C_1, is:[38]

$$C = C_0 + (C_1 - C_0)\left(1 - \frac{4}{\pi}\sum_{n=0}^{\infty}\frac{(-1)^n}{2n+1}exp\left(-D\frac{(2n+1)^2\pi^2 t}{4l^2}\right)\cos\left(\frac{(2n+1)\pi x}{2l}\right)\right) \quad (2.2)$$

where D is the diffusion coefficient of the gas within the material (Table 2.1) and C is the concentration of gas within the material layer with a thickness of l at a distance of $0<x<l$. For the purposes of this model, $x=0$ is located at the sidewall of the microchannel and $x=l$ is the side of the polymer layer exposed to atmosphere. The solubility of air molecules at the exterior of the degassing material determines the surface concentration C_1. This is determined by Henry's Law $C=sP$, where s is the solubility of air in the material (Table 2.1) and P is the partial pressure of the gas. This solution to Fick's 2nd Law allows the initial gas concentration profile within the degassing material to be determined during degassing in vacuum and during the idle time from $t=0$ until device loading.

Table 2.1: Diffusion and Solubility Characteristics of Potential Device Materials[a]

Material	O_2 Diffusion Coefficient (m^2/sec)	N_2 Diffusion Coefficient (m^2/sec)	Solubility of O_2 (dimensionless)	Solubility of N_2 (dimensionless)
Polydimethylsiloxane (PDMS)	1.6×10^{-9}-3.4×10^{-9} Ref: 18,39-41	2.8×10^{-8}-1.47×10^{-9} Ref: 16,18,41,42	0.18-0.31 Ref: 18,40,41 Air: 0.168 Ref: 18	0.09-0.160 Ref: 18,39-41 Air: 0.168 Ref: 18
Poly(methyl-1-pentenylene)[b]	1.01×10^{-10}	5.5×10^{-11}	0.243	0.108
Natural Rubber[c]	1.73×10^{-10}	1.17×10^{-10} Ref: 18	0.103	0.0610 Ref: 18
Low Density Polyethylene (LDPE)	4.6×10^{-11}	3.2×10^{-11}	0.0478	0.0231
Polypropylene[d]	1.6×10^{-11}-6.6×10^{-11} Ref: 43	–	0.011-0.067 Ref: 44	–
High Density Polyethylene (HDPE)	1.7×10^{-11}	9.3×10^{-12}	0.018	0.015
Polystyrene	1.2×10^{-11}	5.5×10^{-12}	0.203	0.0679
Polycarbonate	7.5×10^{-12} Ref: 45	2.09×10^{-12} Ref: 45	0.19 Ref: 45	0.114 Ref: 45
Poly(methyl methacrylate)	1.09×10^{-12} Ref: 46	1.48×10^{-13} Ref: 46	0.015 Ref: 46	0.01 Ref: 46
Polyethylene Terephthalate (PETE)	3.6×10^{-13} Ref: 47	1.4×10^{-13} Ref: 47	0.1 Ref: 48	0.058 Ref: 48

[a]All values taken from *Polymer Handbook*[49] unless otherwise noted:
[b]Closest known material to Polymethylpentene/TPX
[c]Properties are similar to cis-1,4-Polybutadiene
[d]The properties for nitrogen could not be found

Once the channels of the device are sealed with liquid, a numerical approach must be employed because degassing causes the surface concentration at the microchannel/polymer interface to transiently decay and no analytical solution exists for a variable boundary condition. The second solution to Fick's 2nd Law is employed in

this case to determine the concentration profile across the material layer with an initial concentration distribution $f(x)$ with constant surface concentrations C_1 and C_2:[38]

$$C = C_1 + (C_2 - C_1)\frac{x}{l} + \frac{2}{\pi}\sum_{n=1}^{\infty}\frac{C_2\cos n\pi - C_1}{n}\sin\left(\frac{n\pi x}{l}\right)\exp\left(-D\frac{n^2\pi^2 t}{l^2}\right) + \frac{2}{l}\sum_{n=1}^{\infty}\sin\left(\frac{n\pi x}{l}\right)\exp\left(-D\frac{n^2\pi^2 t}{l^2}\right)\int_0^l f(x')\sin\left(\frac{n\pi x'}{l}\right)dx' \quad (2.3)$$

where the boundary conditions are given by:

$C = C_1$, $x = 0$, $t \geq 0$;
$C = C_2$, $x = l$, $t \geq 0$;
$C = f(x)$, $0 < x < l$, $t = 0$

Using this equation, our model computes the concentration profile at a new time point using the boundary conditions and concentration distribution from the previous time point. Fick's 1st Law is then used to determine the flux of the gas at the interface between the microchannel and bulk polymer material:

$$J = -D\frac{\partial C}{\partial x} \quad (2.4)$$

The microchannel is initially at atmospheric pressure, but the pressure change is numerically solved to determine the development of the pressure gradient across the fluid volume that drives flow. The pressure within the device microchannels is calculated using the ideal gas law $PV=nRT$, which is valid under the following conditions:

1) the volume the gas molecules occupy is insignificant when compared to the distance between gas molecules,
2) the intermolecular forces between gas molecules are negligible, and
3) the pressure is above the vapor pressure of the liquid. The developed pressure gradient is coupled with the equation governing the average fluid velocity within a rectangular microchannel:

$$U_{ave} = \frac{dl}{dt} = \frac{\gamma w^2}{12ul}\left(\frac{2\sigma\cos\theta(1+\alpha)}{w} + (P_{atm} - P_{channel}) + \int_{T-\varepsilon}^{T}\left(\left.\frac{dP_{channel}}{dt}\right|_{t=T}\right)dt\right) \quad (2.5)$$

where σ is the surface tension coefficient (0.0725 N/m), θ is the contact angle (~110°),[50] w and h are the width and height of the microchannel, α is the aspect ratio of the microchannel w/h, μ is dynamic viscosity ($8.9\text{x}10^{-4}$ Pa·s), l is the distance that the fluid has traveled in the channel, U_{ave} is the average flow velocity, ε is the time step, and γ is the adjustment factor for fluid flow in a rectangular microchannel:[51]

$$\gamma = 1 - 192\alpha\sum_{n=0}^{\infty}\frac{\tanh\left(\frac{(2n+1)\pi}{2\alpha}\right)}{\left((2n+1)\pi\right)^5} \quad (2.6)$$

It is important to include surface tension and the geometry of the microchannel in the model as surface tension forces influence fluid flow during the beginning and end of channel loading when the degassed pressure gradient is smaller than the capillary pressure. Equation 2.5 is a modification of a published equation that describes laminar flow in a partially filled microchannel.[52] This equation utilizes Newton's 2nd Law, where momentum change is balanced by the pressure difference, surface tension, and viscous force. However, we assume that the momentum change is not negligible in degas-driven

flow since the fluid plug has momentum and its inertia resists instantaneous changes in the flow rate. The derivation of equation 2.5 is available in Appendix A. Previous reports have utilized similar mechanisms to derive solutions for unsteady laminar flow of incompressible fluids through rectangular ducts with arbitrary pressure gradients.[53,54] In equation 2.5, the instantaneous change in the pressure gradient is subtracted from the entire pressure gradient, thus enabling inertial effects to counter sudden pressure changes within the microchannel. The simulation iterates until a solution is converged upon for pressure and fluid velocity at each time point. The model continues by computing the surface concentration of the microchannel wall at the next time point with Henry's Law and the concentration gradient across the polymer with equation 2.3. The code terminates when the channel is filled or when fluid flow stops.

2.6 Simulation Results

A number of parameters were investigated that influence the channel pressure, fluid velocity, and channel filling time of degas-driven devices. We explore how material selection, channel length, channel cross-sectional size, degassing layer thickness, initial pressure of the vacuum packaging, idle time before device loading, fluid properties, and contact angle within the channel affect flow in degas-driven devices. For all simulations the channel cross-section is 100 μm x 100 μm and the channel length is 1 m unless otherwise stated. Devices were simulated with an initial degassing pressure of 300 mTorr (4.4×10^{-4} atm), the pressure achieved with a typical two-stage mechanical vacuum pump. The idle time for simulations was 30 seconds, a delay representative of the time necessary for device handling before fluid loading and channel sealing at t=0.

2.7 The Influence of Material Permeability

Different polymer types for use in the degassing layer were first examined. The permeability of a material is governed by both the gas solubility and gas diffusion properties within the material. To date, only PDMS has been used to fabricate devices that employ degas-driven fluid flow. Here, we extend our investigation to other potential materials that may be utilized for degas-driven flow. For example, polymers such as polycarbonate that have very small diffusion coefficients, but high gas solubility, might be suitable materials for the degasing layer of devices. In Fig. 2.2, we modeled an empty channel with no fluid flow to compare the minimum pressures that can be obtained with the most permeable polymers known. Simulated devices have a degassing layer that is 1 mm thick. In Fig. 2.2a, PDMS is so permeable that atmosphere quickly diffuses through a 1 mm thick layer, quickly negating the initial decrease in pressure. However, if thicker layers of PDMS are used, degassing pressures close to 40 kPa can be obtained within the microchannel. These pressures are similar to those that have been measured previously.[29] Additionally, we observe that TPX, a thermoplastic, and synthetic rubber (cis-1,4-Polybutadiene) are potential materials that could be used to replace PDMS in devices. Such devices would degas a channel more slowly than PDMS, however pressures of ~80 kPa are obtainable within 20 minutes. Polycarbonate and LDPE are two other notable materials that could be employed in applications where significant pressure gradients are not required. In addition, we studied polystyrene, HDPE (high-density polyethylene),

PETE (polyethylene terephthalate), and PMMA (poly(methyl methacrylate)), all of which had worse degassing properties than LDPE (Figure 2.2b). For all computations, an average diffusion and solubility coefficient for the material was calculated by weighting the coefficients for nitrogen and oxygen to the proportions found in atmosphere.

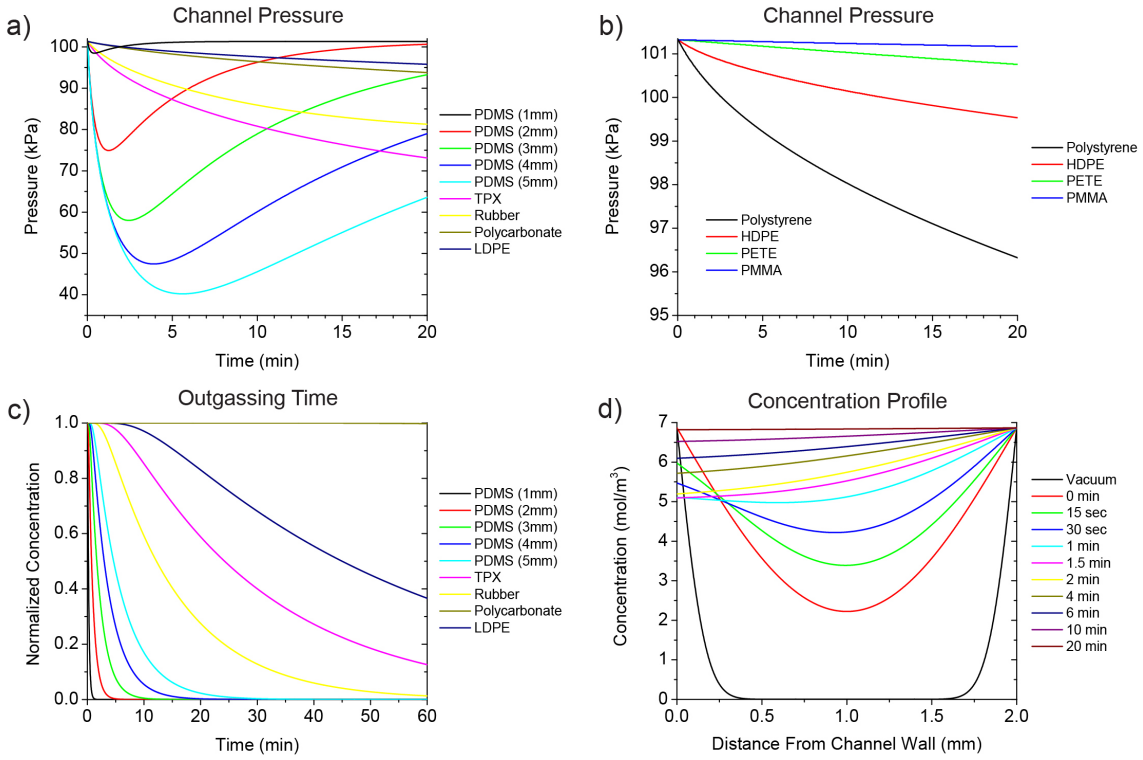

Figure 2.2: a) The pressure within an empty channel with various materials employed for the 1 mm thick degassing layer. The permeability of the material determines the air flux at the channel wall interface and the subsequent pressure within the channel. b) The pressure within an empty channel for less permeable materials that are unlikely candidates for degas-driven flow. c) The time necessary for the bulk of each material to outgas completely before vacuum packaging. The concentration is calculated at the middle of the degassing layer and is normalized to the initial concentration at t=0. d) Time-lapse, spatial concentration profile across a 2 mm PDMS degassing layer adjacent to an empty microchannel. An influx of air from the surrounding atmosphere increases the gas concentration within the bulk PDMS layer.

Next, the time necessary for each of the materials to degas completely was analyzed. This is an imperative aspect to consider for device production, as each material will have a critical degassing time before the vacuum packaging can be sealed. Fig. 2.2c depicts the local concentration at the middle of the degassing material, $x=l/2$, normalized to the concentration solubilized at standard pressure and room temperature (1 atm, 25ºC). The requisite vacuum time increases as the material thickness increases or if less permeable materials are used. All five thicknesses of PDMS can degas completely within 25 minutes, however synthetic rubber, TPX, and LDPE all take a much longer time. An interesting feature to note is that although TPX can degas a microchannel faster than synthetic rubber (Fig. 2.2a), the bulk is slower to outgas in a vacuum (Fig. 2.2c). This is because TPX has higher air solubility and a smaller diffusion coefficient for nitrogen than

synthetic rubber. This result implies that high gas solubility is a useful characteristic for degassing of a microchannel, even if the material has poor gas diffusion properties. This effect is again demonstrated when comparing LDPE and polycarbonate, both of which can degas a microchannel to ~95 kPa in 20 minutes (Fig. 2.2a). Although polycarbonate has nitrogen and oxygen diffusion coefficients 10x smaller than LDPE, the high gas solubility of polycarbonate enables its ability to degas a microchannel. However, there is negligible concentration change observed at the midpoint of polycarbonate within one hour of outgassing (Fig. 2.2c). This analysis suggests that high gas solubility can compensate for poor gas diffusion properties during degassing of a microchannel, but ultimately a high gas diffusion coefficient will lead to shorter device packaging times and higher throughput. We expect that these intricacies will be an important consideration in the material selection of future commercial devices. Furthermore, we have identified synthetic rubber and TPX, and potentially even polycarbonate and LDPE, as viable alternatives to PDMS.

Given the predominate use of PDMS for the fabrication of all degas-driven devices found in literature and its outstanding permeability properties, we decided to analyze devices employing PDMS as the degassing layer. During degas-driven fluid flow in PDMS devices, the microchannel initially depressurizes enabling fluid actuation before the subsequent influx of atmosphere through the device repressurizes the channel, as shown in Fig. 2.2a. This gas flux is visualized in Fig. 2.2d, which depicts the time-lapse, spatial concentration profile across a 2 mm PDMS degassing layer adjacent to an empty microchannel. The orientation of the 1D model is illustrated in Fig. 1g, with the origin at the microchannel wall. The device is degassed to 300 mTorr with a 30 second idle time before the channel inlet is sealed at time t=0. The vacuum time point was simulated after immediate exposure to atmosphere (~1 sec). The air concentration within the bulk PDMS has a parabolic profile at t=0 before gas diffusion produces a linear profile with constant flux, indicative of a membrane with constant, but different surface concentrations. Within 5 minutes, the concentration of the entire bulk PDMS is above 6 mol/m^3 and by 20 minutes the membrane has equilibrated with atmosphere and fluid actuation is exhausted. Concurrent with Fig. 2.2a, the gas concentration at the microchannel wall (x=0) initially decreases until atmosphere diffuses across the porous degassing layer and fluxes into the microchannel. A contour plot of the same concentration profile can be found in Fig. A1 of Appendix A.

2.8 Parameter Analysis of Degas-driven Devices

After ascertaining how material properties influence the degassing of microchannels, we examined how variation in device parameters can alter the fluidic properties in devices fabricated from a 2 mm thick PDMS degassing layer. For all simulations, the viscosity and surface tension of the fluid is equivalent to that of water at room temperature. In Fig. 2.3, dotted lines indicate the calculated pressure within a microchannel during filling and solid lines indicate the distance that the fluid has traveled. Fig. 2.3a investigates how channel length can affect device loading time. In our simulations, when the channel doubles in length, the filling time disproportionally increases due to the decay in the pressure gradient. A significant increase in device

loading time occurred in lengths greater than 100 cm and channel lengths greater than 250 cm were found to only partially fill. Therefore, devices have a maximum channel length that will fill completely although the pressure profile in each channel variation is the same. The length of the microchannel does not affect the degassing pressure since the surface area of the degassing material and channel volume increase proportionally with the channel length. These results denote the importance of considering the channel length when designing devices that require complete filling.

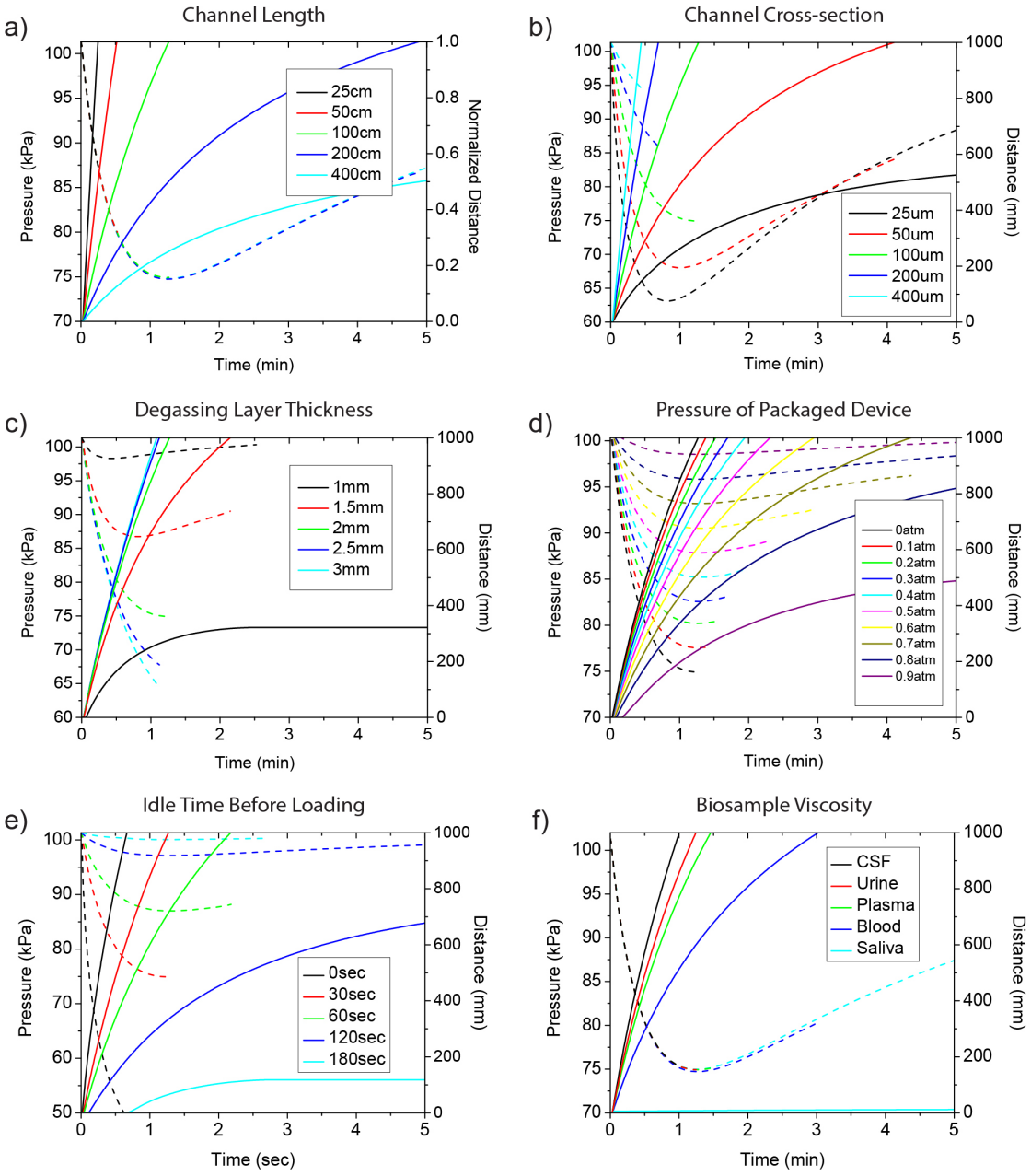

Figure 2.3: The effects that device parameters have on the channel pressure (dashed line) and distance travelled by the fluid (solid line) in devices with a 2 mm thick PDMS degassing layer. Properties of the device investigated are: a) channel length, b) channel side length, c) degassing layer thickness, d) initial degas pressure, e) idle time before fluid loading, and f) biosample viscosity.

The effects of cross-sectional area on channel filling were subsequently evaluated in square channels with sides ranging in length from 25 μm to 400 μm (Fig. 2.3b). Channels with larger cross-sectional areas filled the device much faster than channels with a smaller cross-section. This occurred because capillary pressure in the smaller channels countered the developed pressure gradient and restrained fluid flow. Interestingly, channels with a smaller cross-section reached much lower channel pressures during degassing. However, in channels with a side length of 25 μm, the larger pressure gradient was not enough to ensure complete filling. It is important to note that changes in the channel side length do not correlate proportionally to the degassed pressure within the microchannel. For example, one could hypothesize that doubling the channel side length, which effectively doubles the degassing surface area and quadruples the initial gas volume in the channel, should decrease the pressure gradient by a half. However, this linear correlation is not observed because the gas solubility at the channel/PDMS interface is proportional the partial pressure of the gas. Thus as channels with smaller cross-sections degas to lower pressures, gas flux is reduced due to lower gas solubility in the PDMS bulk, countering the degassing process.

The final geometric parameter examined was the thickness of the degassing PDMS layer (Fig. 2.3c). Layer thicknesses between 1 mm and 3 mm were investigated, with thicknesses greater than 2 mm approaching the minimum time (~65 sec) possible for complete channel loading. Thicknesses less than 2 mm had drastically longer loading times as atmosphere diffused rapidly through the layer preventing sustained pressure gradients, as discussed previously (Fig. 2.2a and Fig. 2.2d). This analysis demonstrates the significance that the layer thickness can have on device loading. As Fig. 2.3c depicts, the 0.5 mm difference between a 1.5 mm and 1 mm thick degassing layer can determine whether the device will load completely. Additionally, the minimal time necessary for complete device filling can be achieved with layers 2.5 mm thick.

An equally valuable parameter that can be regulated during device preparation is the initial pressure in which the device is packaged. We investigated packaging pressures ranging from 0 atm to 0.9 atm, which allowed pressures as low as 75 kPa to be reached within the microchannel (Fig. 2.3d). By varying the initial device pressure, the time to complete device loading can be modulated, potentially allowing timed reactions or biochemical incubations to develop. However, we found that pressures higher than 0.7 atm were not be suitable for complete device loading. In summary, parameters such as the pressure of the vacuum packaged device, channel length, channel cross-section, and thickness of the degassing layer, can be tuned to produce autonomous devices with predetermined flow rates and run times.

The current paradigm of degas-driven devices relies upon an operator to initiate the device by pipetting fluid into the inlet of the device. This method intrinsically introduces large variability into the device as the idle time before fluid loading can significantly influence device performance. Thus far, the simulations in this paper have been implemented with a 30 second idle time, however Fig. 2.3e exemplifies how idle times longer than one-minute can prevent complete device loading by significantly

decreasing the pressure gradient in the microchannel. We believe the current technique of loading degas-driven devices by hand is an obvious pitfall of the technology as slight fluctuations in the idle time lead to drastically different pressure gradients. Future advancements and commercial implementation of degas-driven devices will require an autonomous process that ruptures the degassed chip while simultaneously loading the inlet with fluid. One potential method we envision could be the incorporation of a lancet within a polymeric, vacuum-sealed device.

One essential parameter that impacts device performance is the viscosity of the fluid. Given that biochemical analysis is one area primed for the translation of degas-driven devices, we chose to evaluate the impact that different biosamples have on device loading (Fig. 2.3f). Previous simulations were conducted with a viscosity and surface tension equivalent to water; here we investigated degas-driven fluid flow with cerebral spinal fluid (CSF), urine, plasma, blood (a Newtonian fluid in capillaries), and saliva (a non-Newtonian fluid). Values for the properties of each biofluid are given in Table 2.2. Although the pressure gradient was identical in the channel for each fluid, less viscous fluids traverse the microchannel faster than their viscous counterparts. For example, plasma will fill a device in half the time that whole blood requires for complete channel loading. This result is consistent with our own observance of a plasma head developing in devices loaded with whole blood. Saliva, a shear thinning fluid, never experiences the requisite shear rate to facilitate device loading and our analysis excludes its use as a compatible biosample fluid. Furthermore, the derivation of equation 2.5 (Appendix A) yields that fluid velocity is independent of density, thus viscosity is the most important fluid property governing device loading.

Table 2.2: Properties of Common Biofluids

Biofluid	Viscosity (cP)	Surface Tension (N/m)
Cerebrospinal Fluid (CSF)	0.72 Ref: 55	0.0633 Ref: 56
Urine	0.974 Ref: 57	0.0587 Ref: 58
Plasma	1.2 Ref: 59	0.0569 Ref: 60
Blood[a]	2.7 Ref: 61	0.0583 Ref: 60
Saliva[b]	1/(-0.18991 + 0.20072*(S^0.20733)) Ref: 62	0.0589 Ref: 63

[a]Apparent viscosity remains independent of shear rate at a hematocrit of 0.45 in a capillary tube with a 94 um diameter (relative viscosity being 2.25)
[b]Saliva is a non-Newtonian fluid with viscosity dependence governed by the shear rate, S (1/sec)

One of the deficiencies of degas-driven flow is that the degassing power of the device transiently decays until it is exhausted. Coupling capillary action within degas-driven devices is an option to circumvent incomplete device loading. Surface modification of PDMS has been extensively explored for capillary electrophoresis and droplet-based microfluidic applications.[64-69] By tuning the contact angle of the degassing layer and microchannel, device loading properties can be modulated (Fig. 2.4). A 1 mm thick degassing layer, which fails to completely load in Fig. 2.3c, is simulated with

different contact angles within the microchannel (Fig. 2.4a). Hydrophilic surfaces can enable complete device loading, with smaller contact angles maintaining faster flow rates and achieving greater fill lengths. Surfaces with greater hydrophobicity exhaust earlier during degas-driven fluid flow and achieve shorter travel lengths. The shaded region in Fig. 2.4a depicts the domain in which fluid flow is exhausted for hydrophobic channels. Contact angle can also be utilized to control initial flow rates. Variations in the contact angle of hydrophilic surfaces influence the maximum fluid velocity at the beginning of device loading, with initial velocities greater than 55 mm/sec possible (Fig. 2.4b). In hydrophobic channels, the contact angle can change the initial capillary pinning pressure and time delay before the pressure gradient develops to the extent necessary to breach the capillary pinning pressure. Interestingly, all contact angles converge upon a flow velocity of ~7-10 mm/sec within 10 seconds of fluid loading as the effects of capillary pressure become insignificant and the pressure gradient develops. In summary, the contact angle within the microchannel can be utilized to regulate the time delay before fluid actuation, flow velocity, and device loading time.

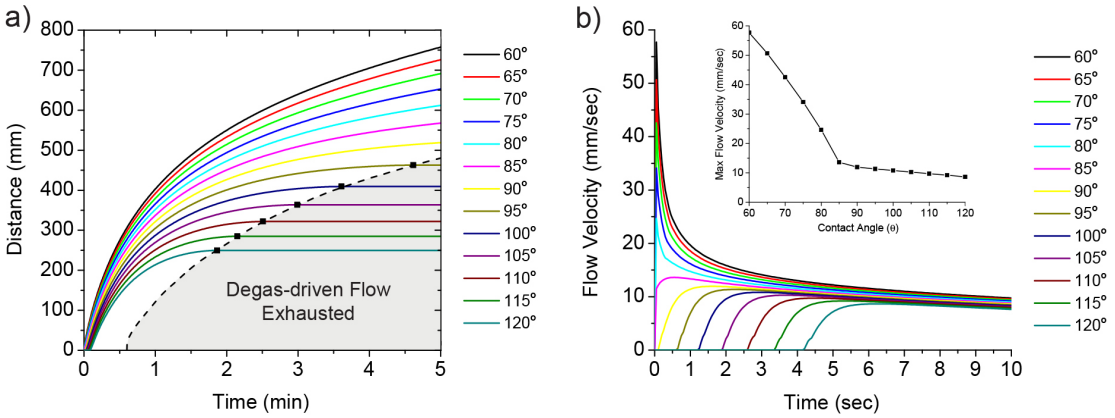

Figure 2.4: A device with a 1 mm thick PDMS degassing layer is simulated with different contact angles within the microchannel. a) Hydrophilic contact angles can ensure device loading, while hydrophobic contact angles exhaust within 5 minutes and achieve shorter travel lengths (shaded region). b) Hydrophilic contact angles can enhance initial flow velocities by 5x (inset), whereas hydrophobic contact angles can delay initial fluid flow by increasing the capillary pinning pressure.

2.9 Model Validation

The validity of our model was assessed with a traditional PDMS device fabricated *via* soft lithography as described in Appendix A. A 2 mm thick monolithic PDMS (Dow Corning Corp.) device with a 100 μm x 100 μm serpentine channel 1 m in length was oxygen plasma bonded onto a glass microscope slide. Devices were exposed to atmosphere for 48 hours to allow PDMS surface recovery from the effects of plasma treatment.[64] The devices were fabricated with a 4 mm boundary around the perimeter of the channels such that the 1D Fickian model of diffusion could be accurately tested and diffusion in the y- and z-axes would be negligible. (See Appendix Fig. A3) The model was modified to account for capillary resistance and gas flux at the three PDMS surfaces of the microchannel. Comparison of the experimental and simulation results is presented in Fig. 2.5. Devices were degassed at 300 mTorr and the travel length of the fluid with

respect to time was measured and compared to the simulation. (Fig. 2.5a) Standard deviation is depicted for a sample population of n=5. A Keyence VHX-500F digital microscope with a frame rate of 16 fps was used to record fluid movement. (Appendix Fig. A2) In Fig. 2.5, the model initially exceeds the average distance travelled by the fluid before eventually undershooting the average. The inset in Fig. 2.5a depicts the normalized residual error for the simulation, which has a maximum error of ±10%. The average fluid velocity at a given channel distance is depicted in Fig. 2.5b. Appendix A contains a representative MATLAB script used to determine fluid flow.

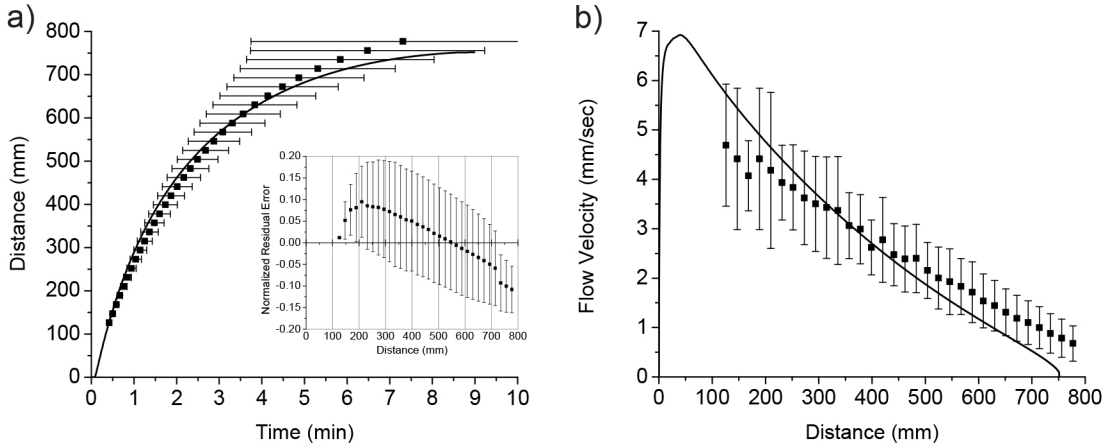

Figure 2.5: Model validation testing with a monolithic 2 mm thick PDMS device (n=5). Devices were degassed at 300 mTorr and the fluid movement was monitored to compare the a) distance travelled by the fluid and b) flow velocity to the simulation. The model (solid line) over predicts flow initially before undershooting the average at the end, however the normalized error is within ± 10% (inset).

2.10 CONCLUSION

An analytically rigorous and predictive numerical model of degas-driven fluid flow is presented and validated experimentally. The influence that geometric, material, and sample properties have on flow velocity and channel pressure were evaluated by applying a 1D Fickian model of diffusion across a plane sheet. The simulations identified alternative materials that may be employed in degas-driven fluid flow and yielded a greater understanding of the effects that diffusion and solubility have on device performance. Channel properties such as length, cross-section, and contact angle were investigated, in addition to other parameters such as the degassing layer thickness, device-packaging pressure, idle time, and fluid viscosity. The presented model facilitates a greater understanding of the potential materials and fluid samples that could be utilized in degas-driven fluid flow. The determination of compatible thermoplastic polymers suggests that translation of device fabrication towards high-throughput manufacturing may be possible using microthermoforming techniques. We anticipate that this basic understanding of degas-driven fluid flow will accelerate its use in many applications such as point-of-care diagnostics, environmental monitoring, and analytical testing in centralized laboratories.

2.11 ACKNOWLEDGEMENTS

Debkishore Mitra, Jasmin Chen, and Kristof Ivan are co-authors of this work, which will be submitted for publication. Financial support was provided by a grant from the Bill & Melinda Gates Foundation (Global Health Grant: OPP1028785). I acknowledge support from a National Science Foundation Graduate Research Fellowship and an award from the Center for Integration of Medicine and Innovative Technology (CIMIT). Kristof Ivan acknowledges support from TAMOP 4.2.1/B-10 and B-11. I would also like to thank Ivan K. Dimov, Tadej Kokalj, and SoonGweon Hong for their helpful insight and Jennifer Monski for her early contributions to the model.

2.12 REFERENCES

1. Hosokawa, K., Sato, K., Ichikawa, N. & Maeda, M. Power-free poly(dimethylsiloxane) microfluidic devices for gold nanoparticle-based DNA analysis. *Lab Chip* **4**, 181–185 (2004).
2. Juncker, D. *et al.* Autonomous microfluidic capillary system. *Anal Chem* **74**, 6139–6144 (2002).
3. Goedecke, N., Eijkel, J. & Manz, A. Evaporation driven pumping for chromatography application. *Lab Chip* **2**, 219 (2002).
4. Walker, G. M. & Beebe, D. J. An evaporation-based microfluidic sample concentration method. *Lab Chip* **2**, 57–61 (2002).
5. Walker, G. & Beebe, D. A passive pumping method for microfluidic devices. *Lab Chip* **2**, 131–134 (2002).
6. Yao, B. *et al.* A microfluidic device based on gravity and electric force driving for flow cytometry and fluorescence activated cell sorting. *Lab Chip* **4**, 603–607 (2004).
7. Weibel, D. B., Siegel, A. C., Lee, A., George, A. H. & Whitesides, G. M. Pumping fluids in microfluidic systems using the elastic deformation of poly(dimethylsiloxane). *Lab Chip* **7**, 1832–1836 (2007).
8. Weng, K.-Y., Chou, N.-J. & Cheng, J.-W. Triggering vacuum capillaries for pneumatic pumping and metering liquids in point-of-care immunoassays. *Lab Chip* **8**, 1216 (2008).
9. Qin, L., Vermesh, O., Shi, Q. & Heath, J. R. Self-powered microfluidic chips for multiplexed protein assays from whole blood. *Lab Chip* **9**, 2016–2020 (2009).
10. Moorthy, J. *et al.* Microfluidic tectonics platform: A colorimetric, disposable botulinum toxin enzyme-linked immunosorbent assay system. *Electrophoresis* **25**, 1705–1713 (2004).
11. Qiu, X. *et al.* Finger-actuated, self-contained immunoassay cassettes. *Biomed Microdevices* **11**, 1175–1186 (2009).
12. Park, S. W., Lee, J. H., Kim, K.-I., Yoon, H. C. & Yang, S. S. An electrochemical immunosensing lab-on-a-chip integrated with latch mechanism for hand operation. *J. Micromech. Microeng.* **19**, 025024 (2009).
13. Li, W. *et al.* Squeeze-chip: a finger-controlled microfluidic flow network device and its application to biochemical assays. *Lab Chip* **12**, 1587–1590 (2012).
14. Munyan, J. W., Fuentes, H. V., Draper, M., Kelly, R. T. & Woolley, A. T.

Electrically actuated, pressure-driven microfluidic pumps. *Lab Chip* **3**, 217–220 (2003).
15. Johnston, I. D., Davis, J. B., Richter, R., Herbert, G. I. & Tracey, M. C. Elastomer-glass micropump employing active throttles. *Analyst* **129**, 829–834 (2004).
16. Singh, A., Freeman, B. & Pinnau, I. Pure and mixed gas acetone/nitrogen permeation properties of polydimethylsiloxane [PDMS]. *J. Polym. Sci. B Polym. Phys.* **36**, 289–301 (1998).
17. Stern, S. A., Shah, V. M. & Hardy, B. J. Structure-Permeability Relationships in Silicone Polymers. *J. Polym. Sci. B Polym. Phys.* **25**, 1263–1298 (1987).
18. Mark, J. E. Polymer Data Handbook. *Oxford University Press, Inc.* 1–1102 (1999).
19. Monahan, J., Gewirth, A. A. & Nuzzo, R. G. A method for filling complex polymeric microfluidic devices and arrays. *Anal Chem* **73**, 3193–3197 (2001).
20. Eddings, M. A. & Gale, B. K. A PDMS-based gas permeation pump for on-chip fluid handling in microfluidic devices. *J. Micromech. Microeng.* **16**, 2396–2402 (2006).
21. He, S. *et al.* Design of a gold nanoprobe for rapid and portable mercury detection with the naked eye. *Chem. Commun.* 4885–4887 (2008).doi:10.1039/b811528a
22. Sato, Y., Sato, K., Hosokawa, K. & Maeda, M. Surface plasmon resonance imaging on a microchip for detection of DNA-modified gold nanoparticles deposited onto the surface in a non-cross-linking configuration. *Analytical Biochemistry* **355**, 125–131 (2006).
23. Hosokawa, K., Sato, T., Sato, Y. & Maeda, M. DNA Detection on a Power-free Microchip with Laminar Flow-assisted Dendritic Amplification. *Anal. Sci.* **26**, 1053–1057 (2010).
24. Hosokawa, K., Omata, M., Sato, K. & Maeda, M. Power-free sequential injection for microchip immunoassay toward point-of-care testing. *Lab Chip* **6**, 236–241 (2006).
25. Hosokawa, K., Omata, M. & Maeda, M. Immunoassay on a power-free microchip with Laminar flow-assisted dendritic amplification. *Anal Chem* **79**, 6000–6004 (2007).
26. Okada, H., Hosokawa, K. & Maeda, M. Power-Free Microchip Immunoassay of PSA in Human Serum for Point-of-Care Testing. *Anal. Sci.* **27**, 237–241 (2011).
27. Dimov, I. K. *et al.* Stand-alone self-powered integrated microfluidic blood analysis system (SIMBAS). *Lab Chip* **11**, 845–850 (2011).
28. Li, G., Luo, Y., Chen, Q., Liao, L. & Zhao, J. A 'place n play' modular pump for portable microfluidic applications. *Biomicrofluidics* **6**, 014118 (2012).
29. Tang, X. & Zheng, B. A PDMS viscometer for assaying endoglucanase activity. *Analyst* **136**, 1222–1226 (2011).
30. Han, Z., Tang, X. & Zheng, B. A PDMS viscometer for microliter Newtonian fluid. *J. Micromech. Microeng.* **17**, 1828–1834 (2007).
31. Han, Z. & Zheng, B. A poly(dimethylsiloxane) viscometer for microliter power law fluids. *J. Micromech. Microeng.* **19**, 115005 (2009).
32. Zhou, X., Lau, L., Lam, W. W. L., Au, S. W. N. & Zheng, B. Nanoliter dispensing method by degassed poly(dimethylsiloxane) microchannels and its application in protein crystallization. *Anal Chem* **79**, 4924–4930 (2007).
33. Inoue, A., Han, A., Makino, K., Hosokawa, K. & Maeda, M. SNP genotyping of

unpurified PCR products by sandwich-type affinity electrophoresis on a microchip with programmed autonomous solution filling. *Lab Chip* **9**, 3297–3302 (2009).
34. Inoue, A., Ito, T., Makino, K., Hosokawa, K. & Maeda, M. I-shaped microchannel array chip for parallel electrophoretic analyses. *Anal Chem* **79**, 2168–2173 (2007).
35. Luo, C. *et al.* A fast cell loading and high-throughput microfluidic system for long-term cell culture in zero-flow environments. *Biotechnol. Bioeng.* **101**, 190–195 (2008).
36. Nevill, J. T. *et al.* Vacuum soft lithography to direct neuronal polarization. *Soft Matter* **7**, 343 (2011).
37. Liang, D. Y., Tentori, A. M., Dimov, I. K. & Lee, L. P. Systematic characterization of degas-driven flow for poly(dimethylsiloxane) microfluidic devices. *Biomicrofluidics* **5**, 024108–024108–16 (2011).
38. Crank, J. *The mathematics of diffusion*. (1975).
39. De Bo, I. *et al.* Investigation of the permeability and selectivity of gases and volatile organic compounds for polydimethylsiloxane membranes. *J Membrane Sci* **215**, 303–319 (2003).
40. Merkel, T. C., Bondar, V. I., Nagai, K., Freeman, B. D. & Pinnau, I. Gas Sorption, Diffusion, and Permeation in Poly(dimethylsiloxane). *Polymer Science Part B* **38**, 415–434 (2000).
41. Robb, W. L. Thin silicone membranes--their permeation properties and some applications. *Annals of the New York Academy of Sciences* **146**, 119–137 (1968).
42. Tremblay, P., Savard, M., Vermette, J. & Paquin, R. Gas permeability, diffusivity and solubility of nitrogen, helium, methane, carbon dioxide and formaldehyde in dense polymeric membranes using a new on-line permeation apparatus. *J Membrane Sci* **282**, 245–256 (2006).
43. Kiryushkin, S. G. & Gromov, B. A. Measurement of the diffusion coefficient of oxygen in a polymeric substance in a polymeric substance. *Polymer Science U.S.S.R.* **14**, 1917–1920 (1972).
44. Somlai, L., Liu, R., Landoll, L., Hiltner, A. & Baer, E. Effect of orientation on the free volume and oxygen transport of a polypropylene copolymer. *J. Polym. Sci. B Polym. Phys.* **43**, 1230–1243 (2005).
45. Laot, C. M. Gas Transport Properties in Polycarbonate. *Dissertation, Virginia Polytechnic Institute and State University.* (2001).
46. Patel, V. M., Patel, C. K., Patel, K. C. & Patel, R. D. Diffusion of gases in poly (methyl methacrylate). *Makromol. Chem.* **158**, 65–79 (1972).
47. Michaels, A. S., Vieth, W. R. & Barrie, J. A. Diffusion of Gases in Polyethylene Terephthalate. *J. Appl. Phys.* **34**, 13–20 (1963).
48. Michaels, A. S., Vieth, W. R. & Barrie, J. A. Solution of Gases in Polyethylene Terephthalate. *J. Appl. Phys.* **34**, 1 (1963).
49. Pauly, S. *Polymer Handbook (4th Edition)*. John Wiley & Sons. New York, NY. (1999).
50. Mata, A., Fleischman, A. J. & Roy, S. Characterization of Polydimethylsiloxane (PDMS) Properties for Biomedical Micro/Nanosystems. *Biomed Microdevices* **7**, 281–293 (2005).
51. Tanyeri, M., Ranka, M., Sittipolkul, N. & Schroeder, C. M. A microfluidic-based hydrodynamic trap: design and implementation. *Lab Chip* **11**, 1786 (2011).

52. Song, H., Wang, Y. & Pant, K. System-level simulation of liquid filling in microfluidic chips. *Biomicrofluidics* **5**, 24107– (2011).
53. Qi, X., Scott, D. & Wilson, D. Modelling laminar pulsed flow in rectangular microchannels. *Chemical Engineering Science* **63**, 2682–2689 (2008).
54. Fan, C. & Chao, B.-T. Unsteady, laminar, incompressible flow through rectangular ducts. *Journal of Applied Mathematics and Physics (ZAMP)* **16**, 351–360 (1965).
55. Yetkin, F. *et al.* Cerebrospinal fluid viscosity: a novel diagnostic measure for acute meningitis. *South. Med. J.* **103**, 892–895 (2010).
56. Kratochvíl, A. & Hrncír, E. Correlations Between the Cerebrospinal Fluid Surface Tension Value and 1. Concentration of Total Proteins 2. Number of Cell Elements. *Gen. Physiol. Biophys.* **21**, 47–53 (2002).
57. Putnam, D. F. Composition and concentrative properties of human urine. *NASA Contractor Report*, *NASA CR-1802*. 1-107 (1971).
58. Mills, C. O., Elias, E., Martin, G. H., Woo, M. T. & Winder, A. F. Surface tension properties of human urine: relationship with bile salt concentration. *J. Clin. Chem. Clin. Biochem.* **26**, 187–194 (1988).
59. Gordon, R. J., Snyder, G. K., Tritel, H. & Taylor, W. J. Potential significance of plasma viscosity and hematocrit variations in myocardial ischemia. *Am. Heart J.* **87**, 175–182 (1974).
60. Rosina, J. *et al.* Temperature dependence of blood surface tension. *Physiol Res* **56 Suppl 1**, S93–8 (2007).
61. Reinke, W., Johnson, P. C. & Gaehtgens, P. Effect of shear rate variation on apparent viscosity of human blood in tubes of 29 to 94 microns diameter. *Circ. Res.* **59**, 124–132 (1986).
62. Rantonen, P. J. & Meurman, J. H. Viscosity of whole saliva. *Acta Odontol. Scand.* **56**, 210–214 (1998).
63. Lam, J. C. M., Kairaitis, K., Verma, M., Wheatley, J. R. & Amis, T. C. Saliva production and surface tension: influences on patency of the passive upper airway. *J. Physiol. (Lond.)* **586**, 5537–5547 (2008).
64. Maji, D., Lahiri, S. K. & Das, S. Study of hydrophilicity and stability of chemically modified PDMS surface using piranha and KOH solution. *Surf Interface Anal* **44**, 62–69 (2012).
65. Jin, M. *et al.* Super-hydrophobic PDMS surface with ultra-low adhesive force. *Macromol. Rapid Commun.* **26**, 1805–1809 (2005).
66. Lee, G.-B., Lin, C.-H., Lee, K.-H. & Lin, Y.-F. On the surface modification of microchannels for microcapillary electrophoresis chips. *Electrophoresis* **26**, 4616–4624 (2005).
67. Vickers, J. A., Caulum, M. M. & Henry, C. S. Generation of Hydrophilic Poly(dimethylsiloxane) for High-Performance Microchip Electrophoresis. *Anal Chem* **78**, 7446–7452 (2006).
68. Abate, A. R., Lee, D., Do, T., Holtze, C. & Weitz, D. A. Glass coating for PDMS microfluidic channels by sol-gel methods. *Lab Chip* **8**, 516–518 (2008).
69. Bauer, W.-A. C., Fischlechner, M., Abell, C. & Huck, W. T. S. Hydrophilic PDMS microchannels for high-throughput formation of oil-in-water microdroplets and water-in-oil-in-water double emulsions. *Lab Chip* **10**, 1814–1819 (2010).

CHAPTER 3

UNIVERSAL BLOOD SAMPLE PREPARATION DEVICE

3.1 ABSTRACT

We have developed a self-powered microfluidic module for blood sample preparation. The module separates plasma from a fingerstick (<50μL) of human blood and simultaneously extracts disease biomarkers by the electrochemical lysis of cells (blood and pathogenic). The module is intended to be incorporated upstream of nucleic acid and protein detection systems as a universal component for cell-based diagnostic platforms. Here we focus on sample preparation of infectious diseases, however the module could be coupled for cancer, autoimmune, and cardiovascular disease diagnostics. The design and fabrication of the sample preparation chip has been optimized such that plasma extraction occurs in less than 10 minutes and devices can be fabricated in less than 3 hours by multi-laminate construction. Various sedimentation-based trench geometries have been simulated, tested, and compared to the traditional SIMBAS (Self-powered Integrated Microfluidic Blood Analysis Device) trench,[1] such as profiles that load blood at the bottom of the trench and others with extraction channels at the middle and top of the trench. Additionally, separation techniques other than the sedimentation-based trench geometry have been investigated, such as nylon mesh and paper filtration methods. However, the trench-based plasma separation method remains the most efficient and reliable technique we have developed thus far. Furthermore, we have optimized the electrochemical lysis voltage, 1.9V, for whole blood and we have built a portable, battery-powered platform employing a BASIC Stamp microcontroller that enables the device to be run outside of the lab, tether-free. We have taken steps towards optimizing the integration, reliability, and manufacturability of the chip by producing multi-layer laminated devices that can be rapidly produced *via* roll-to-roll manufacturing. Finally, we demonstrate nucleic on-chip acid amplification using the isothermal Loop-mediated Amplification (LAMP) technique.

3.2 INTRODUCTION

The field of microfluidics is often described as a technology in search of an application. Constant advances are being made in academia as the low barrier-to-entry allows the rapid expansion of the microfluidic community and overall progress of the field. However, very few of these innovations are successfully translated into commercial products. One analogy put forth is that the technology is a "hammer in search of a nail."[2] Recently, funding initiatives by the Bill & Melinda Gates Foundation and DARPA (Defense Advanced Research Projects Agency) have helped re-identify point-of-care diagnostics as a potential area to apply microfluidics. The traditional realms of microfluidic research have consistently been areas such as cell analysis,[3-6]

biomolecular screening,[7,8] and high-throughput systems.[9-11] Utilizing microfluidics for point-of-care diagnostics is a concept over a decade old with only gradual advancement. Early generation blood preparation modules were proposed that used filters for cell collection/concentration and an on-chip Peltier heater/cooler for PCR thermal cycling of target DNA.[12] (Fig. 3.1a) At the heart of this endeavor is an effort to develop a sample-to-answer system that can isolate cellular biomarkers and enzymatically amplify the target to detectable levels. This concept is pursued in this chapter with the intent to create a system capable of diagnosing the three major infectious diseases endemic to resource-limited regions of the world: HIV, Malaria, and Tuberculosis (TB).[13]

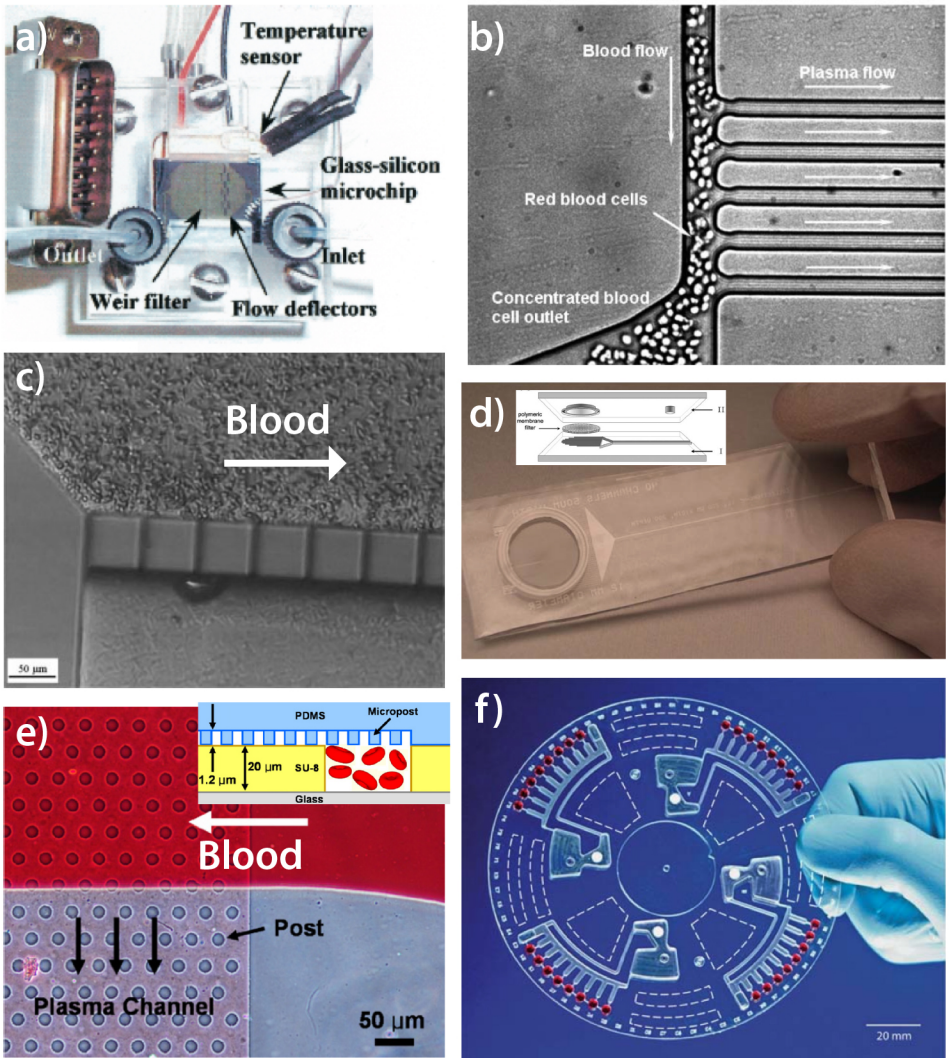

Figure 3.1: a) One of the first proposed multi-component microfluidic devices for blood sample preparation and nucleic acid amplification. The device has a filter for white blood cell isolation and an on-chip Peltier heater/cooler for PCR thermocycling.[12] Various types of plasma separation methods have been suggested including b) the Zweifach-Fung effect,[14] c) a self-clearing transverse silicon filter,[15] d) polymeric membrane filter integrated into a hydrophilic device (inset: three-layer device assembly),[16] e) pillar-based filter (inset: cross-section),[17] and f) sedimentation-based separation.[18] CD-based devices can employ different centrifugal forces and

valving to achieve multi-step sample preparation, ELISA, and nucleic acid amplification reactions.

Over the past decade, few innovations have been achieved for blood sample preparation. Plasma separation is often an intrinsic component of sample preparation as the hemoglobin in whole blood inhibits a number of nucleic acid amplification schemes.[19] Dilution of the blood sample is possible, however this adversely decreases the biomarker concentration. For diseases with DNA copy numbers approaching detectable limits of current technology such as sepsis (10-100 copies/mL) and HIV ($\geq 10^4$ copies/mL), sample dilution has deleterious effects on assay sensitivity and utility. This has motivated researchers to seek plasma filtration schemes that can be incorporated upstream of detection systems. One of the oldest forms of plasma extraction are techniques that employ the Zweifach-Fung effect.[14,20-29] (Fig. 3.1b) In these devices, microfluidic side channels branch off from a larger main channel to extract 15% to 25% of plasma from blood. The main channel has a high flow rate and less resistance than the smaller plasma skimming channels. Blood cells are maintained in the larger main channel because they are exposed to a higher pressure gradient and an asymmetric distribution of shear forces on the cell surface produces a torque on the cell that maintains the cell in streamlines of faster flow rates (also known as axial focusing).[14,30] Companies such as Roche Diagnostics Corp. are investigated employing the Zweifach-Fung effect in the diagnostic units they are developing for centralized clinical laboratories. However, due to the high flow rates that are required, the performance dependence upon hematocrit, and the accompanying methods to pump blood, this method is unlikely to be integrated into handheld diagnostic devices.

Another common method of plasma extraction is filtration. Monolithic devices consisting of "weir-type" filters etched directly into the chip, [12,15] (Fig. 3.1a) self-clearing transverse-flow micromembranes that provide reduced-clog plasma extraction, [31,32] (Fig. 3.1c) and membrane filters incorporated between device layers, across blood flow have all been employed in portable diagnostic devices.[16,33] (Fig. 3.1d) Additionally, a number of blood-based filtration membranes have recently entered the lateral flow assay market such as the Whatman® FUSION 5™ and Pall Corp. Vivid™ Plasma Separation Membrane. These membranes provide reliable capillary action while filtering blood cells without excessive hemolysis, a major inhibitor of immunoassay sensitivity. Collectively, these methods provide adequate plasma extraction for small blood volumes, but cells will eventually amass on the filter and restrict blood flow through the filter. In devices where a pressure gradient is applied (most microfluidic devices other than capillary action), cells will inevitably rupture and release lysate downstream. Monolithic filters with transverse self-clearing capabilities are reliable, but inheritably expensive to produce the micron scale geometries necessary for red blood cell filtration. Integration with commercial filters most often has integration problems, as I will address later in this chapter with the laminated devices we have developed. In general, for microfluidic devices where larger volumes of blood must pass through the filter without clogging ($\geq \mu L$), filtration is not a feasible mechanism.

Recently, pillar-based and bead-based capillary beds have been used as means for plasma separation. These methods employ capillary action to autonomously drive blood

flow through the device, allowing tether-free operation.[17,34-36] (Fig. 3.1e) A wide range of immobilization chemistries is known for biomolecule conjugation onto beads allowing specific biomarker capture. Depending upon the material use, pillar-based chips can also be conjugated for cell capture.[37] The main drawback of these techniques is that sample volume is limited for capillary action.

Finally, blood sedimentation is another method of plasma extraction that utilizes gravity or centrifugal forces to separate blood cells from plasma. Gravity-based sedimentation has long been used as a tool to measure hematocrit levels of blood mixed with anti-coagulants. Our lab has used a microfluidic trench to facilitate gravity-based sedimentation and a top channel to skim plasma from blood.[1] We utilize this method in the subsequent sections of this chapter for blood sample preparation. Recently, an angled device with an elbow connector was fabricated to enable gravity-based sedimentation for continuous plasma separation.[38] These methods require little power and can be reliable. However, sedimentation rates are slow (maximum rates of ~80-160 μm/min)[39] and if the device is disturbed, the blood will be agitated and sedimentation will have to performed again. CD-based microfluidic devices have employed centrifugal forces to accelerate cell sedimentation.[40,41] (Fig. 3.1f) These devices enable added complexity for reagent valving by altering the angular velocity. This added flexibility has been used to integrate specific bead-based DNA extraction[42] and downstream biomarker detection on-chip.[18,42-45] However, the first use of CD-based devices was over a decade ago and translation of this technology has been slow, potentially due to the constrains of requiring an external device to manipulate fluid flow.[46,47]

The second integral component of sample preparation is often cell lysis for biomarker extraction. This process is requisite for both nucleic acid and protein-based assays and is often performed with chemical lysis agents,[48] mechanical disruption of the cell membrane with barbs or magnetically-actuated beads,[49-51] electrical generation of lytic species and/or electroporation,[52,53] or application of thermal stresses to destabilize the cell membrane.[42,54,55] Until recently, thermal cell lysis was the most common technique as devices were employing on-chip PCR, which requires temperatures as high as 95°C for thermocycling. Cell lysis could be simply achieved with an initial 5 minute cycle before amplification. However, due to excessive power consumption during thermocycling and the need for devices with increased portability, isothermal nucleic acid techniques are now being investigated. These methods can be applied at much lower temperatures; 65°C for Loop-mediated Amplification (LAMP)[56] and 37°C for Recombinase Polymerase Amplification (RPA).[57] However, alternative lysis methods are now needed for these detection schemes. Chemical lysis is often a difficult method to implement on-chip as valving and advanced fluidic logic is needed for the multiple wash steps, which necessitates complex chip design. The use of magnetically-actuated beads for lysis is an attractive option because beads can be conjugated with antibodies and DNA for specific biomarker capture and concentration.[42,58] However, this technique requires mechanical readers to actuate a magnet. Electrical cell lysis techniques are promising as electrodes can be directly fabricated on-chip and devices can be designed with electrical interconnects to provide power. Electroporation is feasible, but requires a high voltage supply and biomarker extraction can be minimal.[53] One of the methods

developed in our lab, and a relatively unknown method, is the generation of hydroxide ions, or lytic species, that destabilize the fatty acid groups of membrane phospholipids and induce membrane permeability. Entire cells can be ruptured with this method, releasing much of the cytoplasmic material into the suspending fluid. Consequently, this is the method used for cell lysis in this chapter and will be discussed further later in this chapter.

The summation of the work described in this chapter is part of an effort to create a device that can effectively separate blood cells from plasma and extract protein and nucleic acid biomarkers for downstream detection. (Fig. 3.2) The target diseases are TB, HIV, and Malaria. Fig. 3.2 describes the process flow for the blood sample preparation device (yellow highlights) and subsequent downstream detection methods for TB (ELISA), HIV (ELISA and nucleic acid), and Malaria (nucleic acid).

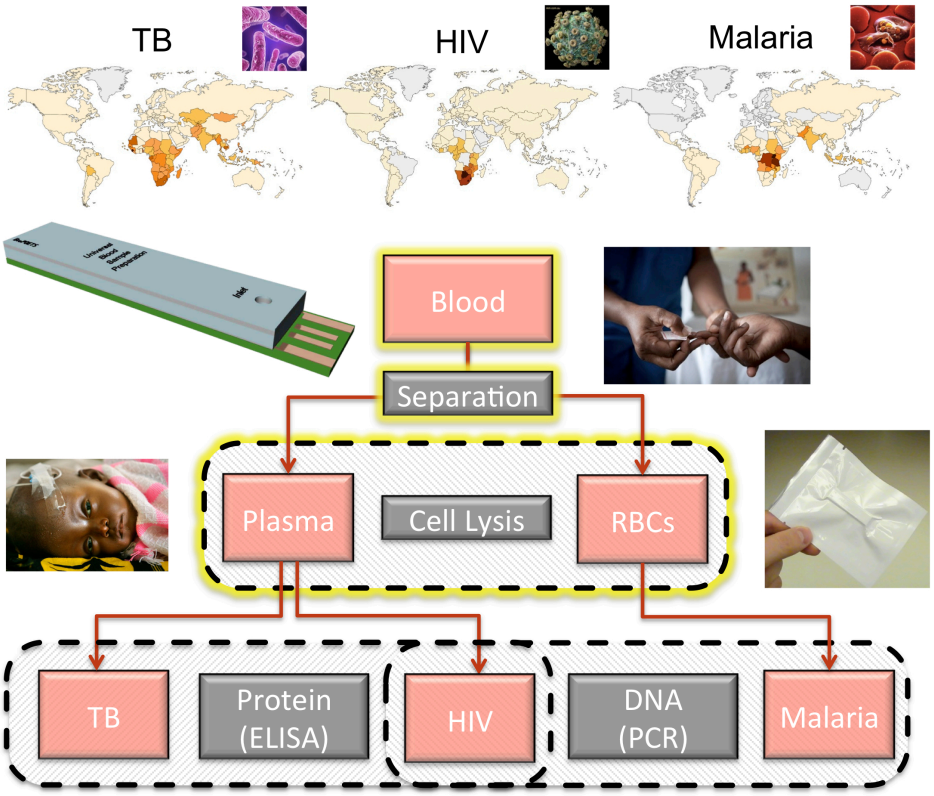

Figure 3.2: The process flow for blood sample preparation. The upstream processes covered in this chapter are highlighted in yellow, followed by the downstream detection methods.

3.3 Sedimentation-based Microfluidic Blood Fractionation

Over the course of this project, several different designs and fabrication methods were investigated for the development of our universal blood sample device. However, a multi-laminated five-layer design that uses traditional trench-based sedimentation was determined to be the most promising design for sample preparation. The current versions of the device are fabricated layer-by-layer from pressure sensitive adhesive (PSA) layers

with double-sided silicone adhesive (Adhesives Research, Inc.). Each PSA layer is cut by a CO_2 laser machining system (VersaLaser) and assembled by hand. In Fig. 3.3, the first PSA layer is an electrode contact layer with a predetermined area for fluidic contact with electrodes. This facilitates a constant amount of hydroxide generation at a given voltage. The subsequent layers are alternating layers with fluidic channels and layers with *via* interconnects. An 800 μm silicone layer (Stockwell Elastomerics, Inc.) located in the middle layer of the device enables degas-driven fluid flow. A CO_2 laser also cuts this silicone layer, although once a final device design is decided upon die punching could be utilized. The bottom substrate is standard 0.1" FR4 PCB (printed circuit board, Advanced Circuits) with copper electrodes. Finally, a top 250 μm impermeable polycarbonate layer is located at the top to act as a hermetic seal during the degassing process. We envision that devices fabricated layer-by-layer could eventually be produced using roll-to-roll fabrication techniques. Fig. 3.3 depicts one version of the device that we have produced with 8 layers and an integrated nylon mesh filter for enhanced plasma separation. A USB interface is employed to enable electrochemical lysis on-chip and facilitate chip portability.

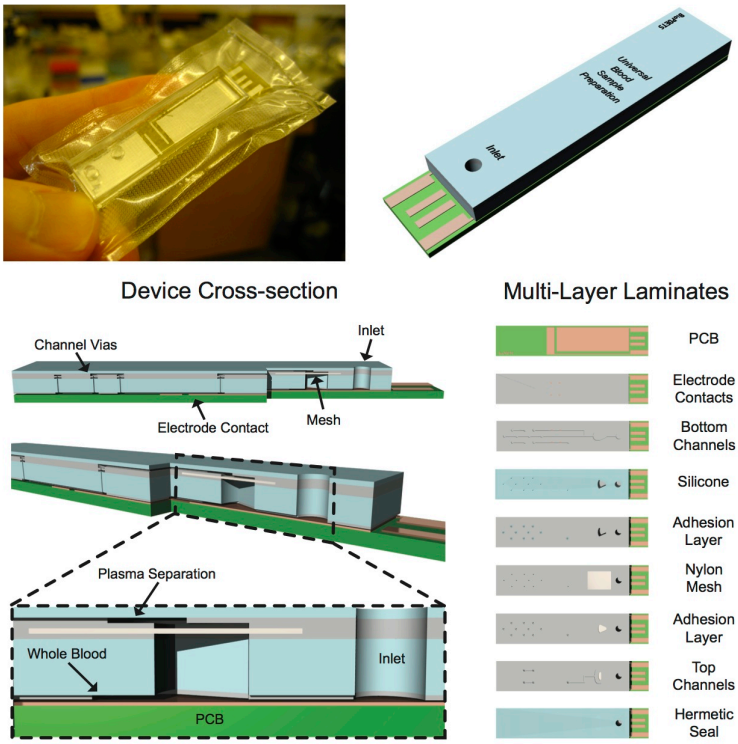

Figure 3.3: USB-interface version of the universal blood sample device. Layer-by layer assembly enables rapid production of the devices in less than three hours, a much faster process than devices created by soft-lithography.

One benefit of layer-by-layer fabrication is the speed of device production in comparison to traditional microfluidic device processing *via* soft-lithography and casting of elastomeric PDMS (polydimethylsiloxane) over a mold. Using the VersaLaser, new designs can be produced within 3 hours in comparison to traditional soft-lithography techniques, which can require more than one day to produce a mold by photolithography,

cast and cure devices, and bond devices onto a substrate. Others have previously expressed concern with the current methods and materials (PDMS) used to fabricate microfluidic devices.[59] I share these concerns and believe that in order for a microfluidic device to become a viable commercial product, devices will have to be produced with rapid fabrication techniques such as hot embossing and injection molding. Layer-by-layer/roll-to-roll assembly may be another viable technique permitting added multi-layer complexity in comparison to the design constraints of monolithic devices created by embossing and molding.

Fig. 3.4 depicts time-lapsed images of whole blood separation in our device with the traditional trench geometry. We have optimized the design such that a wider plateau region exists at the top of the rectangular trench, allowing flow expansion to decelerate fluid flow and enhance sedimentation. The plateau region also prevented trench malfunction by inhibiting capillary action at the top of the trench as blood can wick across the ceiling, bypassing the sedimentation trench. This particular device enables plasma skimming within 10 minutes of device loading. The device was vacuum packed at 300 mTorr and blood entered the device by degas-driven flow.

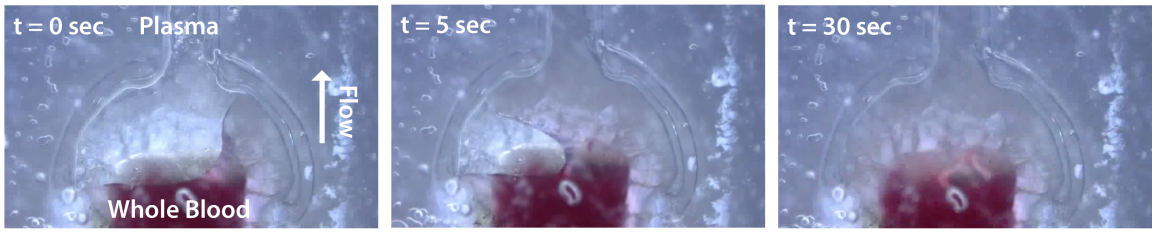

Figure 3.4: Time-lapse image of whole blood plasma separation in device. Plasma was separated from human whole blood in less than 10 minutes.

Trench geometries other than the traditional SIMBAS profile[1] were analyzed in an effort to increase plasma separation efficiency and decrease the sedimentation time necessary within the trench. COMSOL simulations of blood filtration where conducted with two trench geometries. (Fig. 3.5) The traditional cross-section was compared to a low-to-high design, where blood fills from the bottom of the trench. For the simulation of both designs, the blood enters the trench cross-section at the left side and flows rightward toward the outlet at the top right corner. The volume fraction of the dispersed phase (red blood cells, RBC) was simulated with the parameters: ρ_{RBC} = 1139 kg/m^3, ρ_{plasma} = 1025 kg/m^3, [RBC] = 5x10^9 cells/mL, and η_{plasma} = 1.5x10^{-3} Pa·sec. In the low-to-high geometry, cell accumulation at the lower right corner slowly alters the flow path lines of the blood, resulting in a significant change to the fluid streamlines within the trench. In the traditional trench, the blood cells were found to sediment mainly at the corners of the trench. Comparison of the two designs yields that the traditional trap separates ~6-10% more blood cells than the low-to-high trap, thus we continued to employ the traditional geometry in our designs.

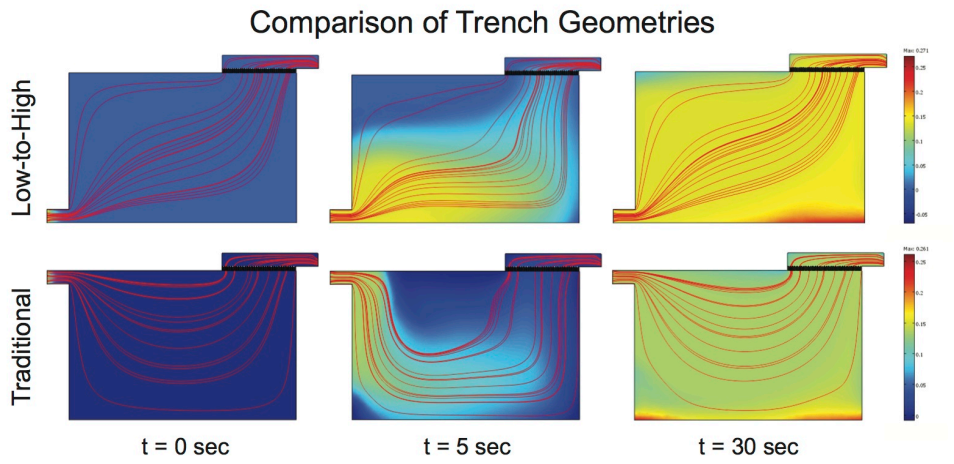

Figure 3.5: COMSOL simulations of plasma skimming with traditional and low-to-high trench designs. The figures depict the volume fraction of the dispersed phase (red blood cells) and the dispersed phase velocity field is depicted by the streamlines. Traditional (SIMBAS) trench geometries are more efficient at plasma separation.

Alternative methods intended to compliment and enhance sedimentation-based plasma separation were investigated. The integration of a 5 μm nylon mesh, typically used for filtration of cell suspensions, was simulated in COMSOL. Two and three outlet geometries were modeled with the traditional and low-to-high trench profiles. (Fig. 3.6) The filter membrane was placed directly below the plasma extraction channel with the intention of providing cell filtration in addition to sedimentation. The three outlet geometry was designed to provide transverse cross flow that would allow the clearing of any potential cell aggregates to the membrane filter. However, the simulated transverse flow velocity across the filter membrane is not sustained at a significant rate due to the filter membrane resistance for 5 μm pores. Larger pore sizes would decrease filter resistance and increase flow in the vicinity of the filter membrane, however red blood cells (3 μm to 8 μm) would likely penetrate the nylon mesh.

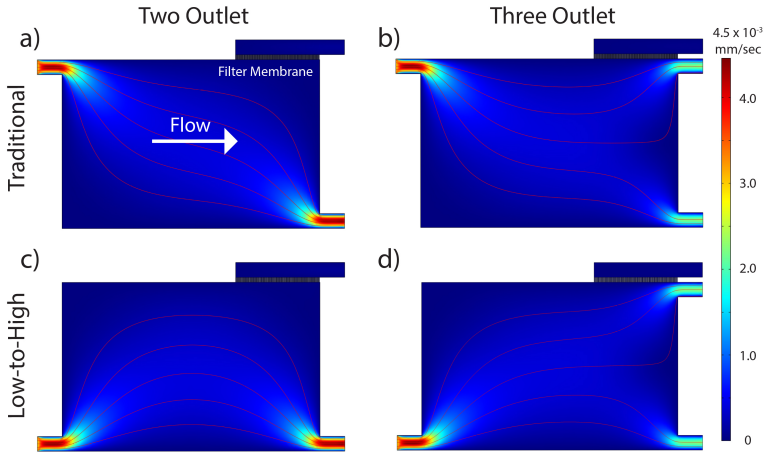

Figure 3.6: COMSOL simulations of an integrated nylon mesh for cell filtration to enhance plasma separation. Three outlet geometries were designed with transverse cross flow across the membrane filter to clear cell aggregates.

Devices with integrated nylon mesh layers were fabricated with the three outlet geometry depicted in Fig. 3.6b. (Fig. 3.7) The top fluidic layer was designed to extract plasma, while the middle and bottom layers would extract the blood with concentrated red blood cells from the trench, preventing the trench from filling with cells and prolonging plasma separation. (Fig. 3.7e) Nylon meshes with pore sizes of 1, 5, 10, and 20 μm were integrated into the devices and whole human blood was loaded into the device by degas-driven fluid flow. Unfortunately, it was determined that red bloods cells were not being filtered by the nylon mesh, regardless of pore size. (Fig. 3.7c) The flexible blood cells could penetrate through the mesh pores and plasma separation could not be accelerated past the 10 min time necessary for cell sedimentation.

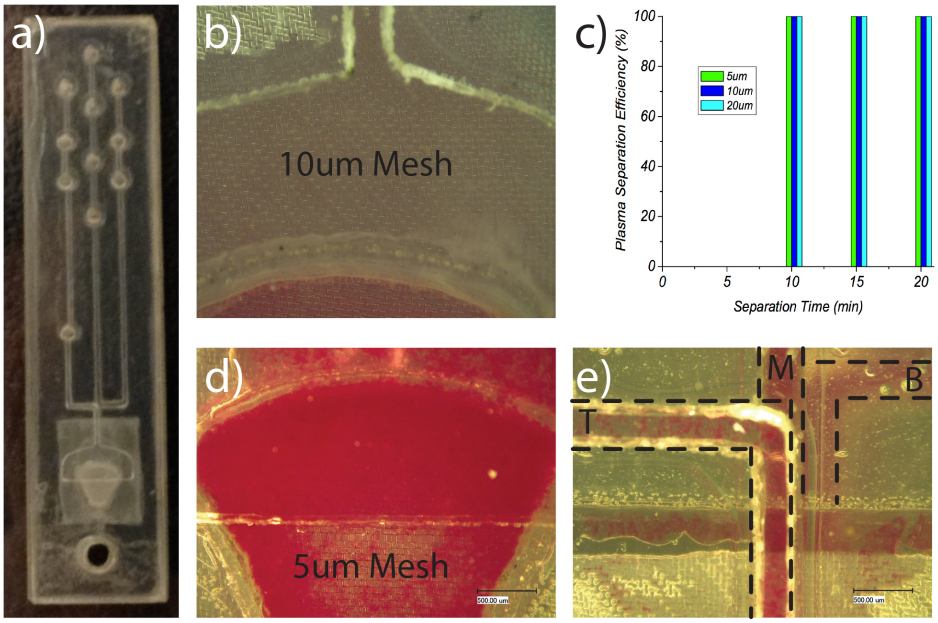

Figure 3.7: Nylon mesh cell filters were integrated into devices with the intention of enhancing sedimentation-based plasma separation times. However, red blood cells penetrated the small pores of the filter and separation was not improved.

Although the integrated nylon mesh filtration method did not enhance plasma separation, chips designed with the additional bottom channel for collection of concentrated blood cells could be used for the detection of enriched malarial biomarkers within the red blood cell population. Depending on the hematocrit level of the blood sample, which is typically between 35-70%, cell concentrations up to 2x have been obtained. However, systems that concentrate greater than 2x can be attained by alternative methods such as DNA/RNA purification or magnetic bead-based purification of target antigens. These enrichment methods could also be applied for the HIV and TB biomarkers. However, these types of strategies for biomarker concentration will require more advanced fluidic handling operations and will be challenging to implement on-chip.

Another alternative method to enhance cell sedimentation is blood dilution, either incorporated on-chip or before device loading. By simple analysis of the forces that govern a cell in free-fall, the terminal velocity can be determined:

$$F_D + F_B = Fg \tag{3.1}$$

where F_D is the drag force, F_B is the buoyancy force, and F_g is the force due to gravity. The stokes drag force is:

$$F_D = 6\pi\eta Ur \tag{3.2}$$

where η is the viscosity of plasma ($1.5\text{x}10^{-3}$ Pa·sec), U is the velocity (terminal), and r is the radius of the cell (assuming spherical curvature). The cell buoyancy force is:

$$F_B = \frac{4}{3}\pi r^3\left(\rho_{cell} - \rho_{plasma}\right)g \tag{3.3}$$

where ρ_{plasma} is 1025 kg/m^3. The terminal velocity can be determined by equating equation 3.1 to zero.

$$U = \frac{2}{9}\frac{r^2\rho_{plasma}}{\eta} \tag{3.4}$$

From this equation, the sedimentation velocity can be increased by increasing the density of the plasma (suspension fluid) or by reducing the viscosity, hence reducing the viscous drag on the cell. From this analysis, the dilution of whole blood in a buffer, such as PBS ($\eta_{PBS} = 1.0\text{x}10^{-3}$ Pa·sec and $\rho_{\text{PBS}} = 1000$ kg/m^3), may effectively increase sedimentation velocity by 46%.

Furthermore, biochemical methods can be employed to aggregate red blood cells to induce faster sedimentation rates and possibly enable filter-based separation as previously mentioned. Three techniques for cell aggregation are listed in table 3.1 and include coagulation, agglutination, and Rouleaux formation.[60] Of the three techniques, agglutination with four antigen-binding antibodies (αA, αB, αD, αc+ or αe+) could cover 99.9% of the population, enabling universal compatibility in our device. However, the cost is inhibitory as four antibodies would have to be used at an average of ~$300/each and would greatly inflate the cost per device. A cheaper alternative, Rouleaux formation, was attempted by drying dextran inside the device and allowing the blood to rehydrate the sugar. The mechanism of Rouleaux formation is complex and two theories have emerged: the formation of polymer bridge molecules that effectively neutralize the electrostatic repulsive charges between red blood cells (bridging mechanism) and the attraction of cells by osmotic gradients from the depletion of macromolecules in the intercellular space (depletion model).[61] However, aggregation is completely reversible and disaggregation occurs at low shear rates (50 sec^{-1}).[31] No enhancement of sedimentation was observed in our device using this method due to disaggregation.

Table 3.1: Potential Techniques to Enhance Sedimentation Rates

Method	Agent	Adverse Effects	Rating	Cost
Coagulation	Fibrin, Thrombin, Tissue Factors	Plasma and Platelets Coagulate	3rd	Reasonable
Agglutination	αA, αB, αD, αc+ or αe+	Minimal viscosity change	1st	Expensive
Rouleaux Formation	Dextran 50 to 500 kDa	Viscosity Increases	2nd	Cheap

3.4 ELECTROCHEMICAL LYSIS OF PATHOGENIC CELLS/VIRONS IN BLOOD

Cell and viron lysis is necessary for the extraction of HIV RNA and malarial DNA from red blood cells. These two biomarkers can be detected with nucleic acid amplification schemes downstream and we have initiated isothermal amplification methods on-chip using LAMP. The mechanism of electrochemical lysis utilizes the generation of hydroxide ions, a lysis agent, at the cathode to create localized regions for cell lysis where hydroxide concentration is in excess of 20 mM.[52] One of the main benefits of this technique is that the hydroxide ions are recombined at the anode and electrochemical lysis is non-fouling, unlike chemical lysis methods that can disrupt downstream assays. The half-cell reactions for hydroxide generation and the reduction of water are:

$$\text{Cathode:} \qquad 4H_2O + 4e^- \leftrightarrow 4OH^- + 2H_2 \tag{3.5}$$

$$\text{Anode:} \qquad 2H_2O \leftrightarrow 4H^+ + 4e^- + O_2 \tag{3.6}$$

The electrochemical lysis unit was developed in parallel with the sedimentation trench since changes in geometry/volume influence the blood flow rate within the device during degas-driven flow. Variations in flow consequently affect the efficiency of the electrochemical lysis module. Larger trench volumes have greater dead volume and require an increased amount of time to initiate fluid flow with the degassing method. Since the degassing potential decays with time, larger trench volumes will have slower flow rates by the time plasma and whole blood reach the electrodes for lysis. Fig. 3.8 depicts the lysis of whole blood on a PDMS chip with platinum electrodes deposited on glass. The false-color time lapse images illustrate how rapidly lysis can occur in stagnant flow. Using an electrochemical workstation to vary voltage in real-time, the optimal voltage for whole blood lysis was determined to be approximately 1.91V, with a maximum percent lysis of 81.3% of cells in stagnant flow. We have achieved lysis rates close to 100% on chips with continuous flow.

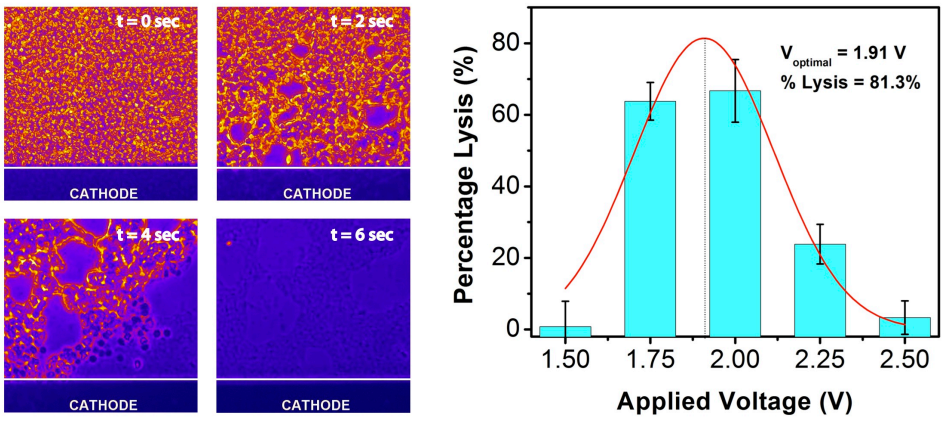

Figure 3.8: False-color, time-lapse image of electrochemical lysis of whole blood and on-chip voltage optimization of lysis in stagnant flow.

For our purposes however, we wish to perform lysis in continuous flow using the copper electrodes common to PCBs. We have found that the continuous flow operation

of our device enables efficiencies close to 100% lysis because the hydroxide ions necessary for lysis flux convectively to the cell membrane in comparison to the slower diffusive fluxes characteristic of stagnant flow. To demonstrate tether-free, on-chip lysis of whole blood, a small breadboard system was built that draws current from a 9V battery. The platform has a BASIC Stamp microcontroller, programed to control a digital potentiometer and modulate the output voltage, a seven-segment LED, which scrolls the selected output voltage, and a USB interface to enable electrical connectivity. Electrochemical lysis of 10x diluted human whole blood in our five layer laminated chip is demonstrated in Fig. 3.9 with the BASIC Stamp system. Additionally, we have tested this system with normal and concentrated whole blood (as described previously) and have achieved successfully cell lysis.

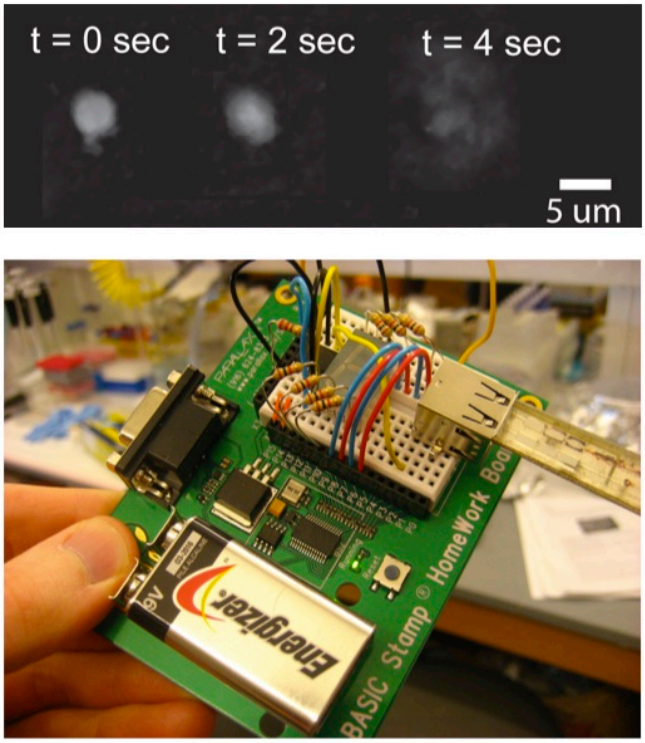

Figure 3.9: Top: On-chip lysis of a cell in 10x diluted whole blood with continuous flow with the copper PCB electrodes on-chip. Bottom: BASIC Stamp microcontroller for portable sample preparation.

A sample preparation module has been developed that achieves both plasma skimming and electrochemical cell lysis in plasma and blood with a concentrated cell suspension. The next step for this sample preparation device will be to utilize a sample panel provided by the Gates Foundation to test the sample preparation module in a disease relevant system with downstream detection assays.

3.5 Integration and Mass Manufacturability of Devices

All components of the sample preparation module must be considered during the development of this device as every additional microfluidic component has an impact on

the flow rate, thus impacting each downstream component. Several technologies have been optimized to enable the interface of these modules, some of which are illustrated in Fig. 3.10. The expansion plateau, previously mentioned, is one development that enables reliable trench loading and enhanced cell sedimentation. The lack of this plateau often results in capillary action drawing the blood across the top of the trench. Additionally, electrode contact ports have been added to control the exposed surface area of the electrical contact with the fluid and provide an additional adhesion layer to prevent device leakage. Furthermore, channel *vias* are not only used to connect channels in different layers, but are integral to device loading. These small holes pass through the silicone layer and the large surface area to volume ratio provides better degassing than the degassing chambers that have been used previously. (Fig. B1) An example of the device evolution is also shown in Fig. B1, illustrating some of the different fluidic circuit geometries that have been investigated.

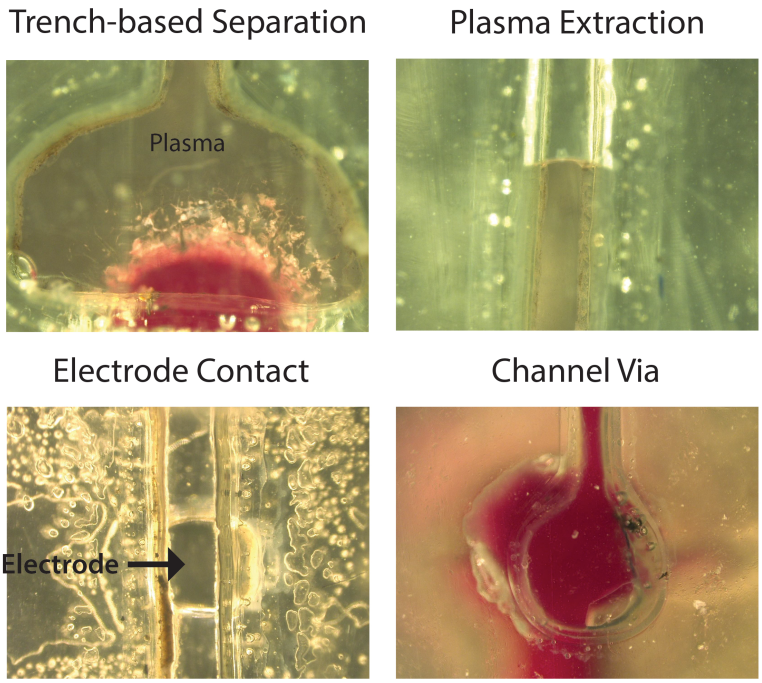

Figure 3.10: The chip components that have been used for component integration within the module include the plasma separation trench, plasma extractions channels, electrode contacts, and multi-layer channel *vias*.

Appendix B briefly outlines the protocol for multi-laminate device fabrication. Since devices are currently fabricated by hand, outside commercial partners have been contacted to pursue the viability of high-yield manufacturing. Partners that could facilitate in the fabrication of these devices include A-Laser, Inc. for laser machining purposes and A-Line, Inc. for device prototyping and rapid assembly. Additionally, minimum resolution constraints, layer alignment limitations, and material costs are considered during the design process to ease transition from academic lab prototyping to industrial scale production.

3.6 BIOMARKER DETECTION

A key importance for the sample preparation module is that the biomarkers for HIV, TB, and Malaria extracted from blood are detectable downstream. Table 3.2 depicts the biomarkers for the diseases that we intend to detect and the clinically relevant concentrations for the pathogens.

Table 3.2: Biomarker Panel for HIV, TB, and Malaria

Target Disease	Biofluid Sample	Biomarker Type	Biomarker Analyzed	Concentration	Necessary Sample Preparation
HIV	**Plasma, Whole Blood**	Protein	P24, anti-HIV-1 Ref: 62	0.06 fg/virus (p24), End-point Titer > 50 (anti-HIV-1)	Plasma separation, virus lysis
		Nucleic Acid	HIV-1 GAG, HIV-1 env Ref: 63	100-10^5 copies/mL	Whole blood lysis, plasma separation, virus lysis
TB	**Plasma**	Protein	Anti-cardiolipin IgM Ref: 64	5-35 MPL	Plasma separation
		MicroRNA	miR-155, miR-29a Ref: 65-67	-	Plasma separation
Malaria	**Whole Blood**	Protein	HRP2, pLDH Ref: 68-71	48 ng/mL (HRP2), 272 U/L (pLDH)	Whole blood lysis, plasma separation
		Nucleic Acid	18s rDNA Ref: 72	10^4 copies/parasite	Whole blood lysis

In effort an effort to integrate the two most commonly used diagnostic methods for pathogen detection, ELISA (Enzyme-linked Immunosorbent Assay) and nucleic acid amplification, the sample preparation device was redesigned with integrated detection components. (Fig.3.11) The new version of the sample preparation device has six characteristic features: 1) an SD (Secure Digital) interface, 2) the traditional SIMBAS cell sedimentation trench, 3) electrode ports for electrochemical lysis of plasma and whole blood, 4) on-chip reagent storage and sequential flow for ELISA, 5) on-chip LAMP reaction wells where the reagents can be lyophilized and rehydrated by plasma/blood, and 6) channel *vias* to enhance the reliability of degas-driven flow.

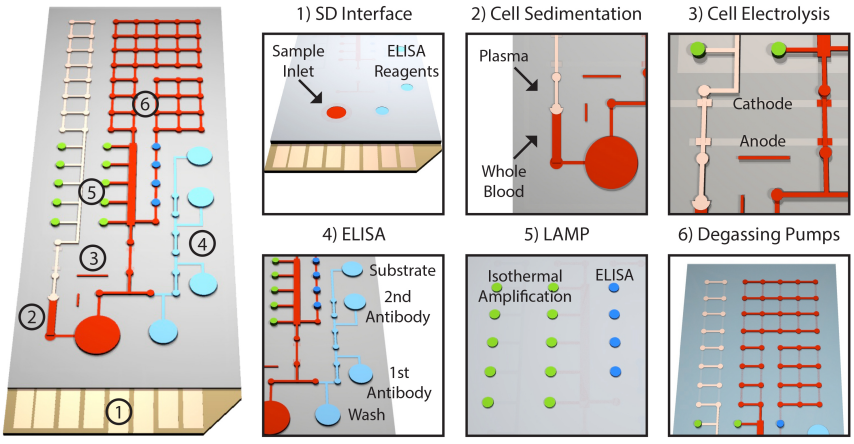

Figure 3.11: SD-interface version of the sample preparation device with downstream ELISA and LAMP components for antigen and nucleic acid detection.

The fabrication of the new version of the sample preparation device is similar to the previous device, only this version has six layers instead of eight. (Fig. B2) Additionally, the device is much thinner as the silicone layer is now only 800 μm thick, instead of the previous 1.6 mm. (Fig. 3.12a) More channel *vias* (degassing pumps) downstream enable a thinner silicone layer to provide the negative pressure necessary for the device to fill completely. The bottom substrate layer is a flexible kapton (polyimide) film with copper electrodes.

To demonstrate that the LAMP method can be achieved on-chip, LAMP reagents were mixed with TB template DNA and loaded into the sample preparation device. The device was incubated at 65°C and end-point fluorescent images were taken of the wells with a Nikon Eclipse TE2000-E microscope. (Fig. 3.12b) Although no fluorescent difference in intensity is observable by eye, image analysis (ImageJ) reveals that the reaction amplified with statistically significant difference ($p<0.001$) between the negative and positive controls. (Fig. 3.12c) A DNA gel was performed to verify the amplification of DNA, evident by the heterogeneous streak in the positive column. Inherent to the nature of the LAMP reaction scheme, amplicons are heterogeneous in length.[56] A major drawback of LAMP is that bubble formation can occur at 65°C, especially in the multi-laminated devices, and fluid in the wells can be displaced during the reaction leading to fluctuations in fluorescent intensity. One possible solution to this problem is to use amplification methods that operate at lower temperatures such as RPA (37°C).

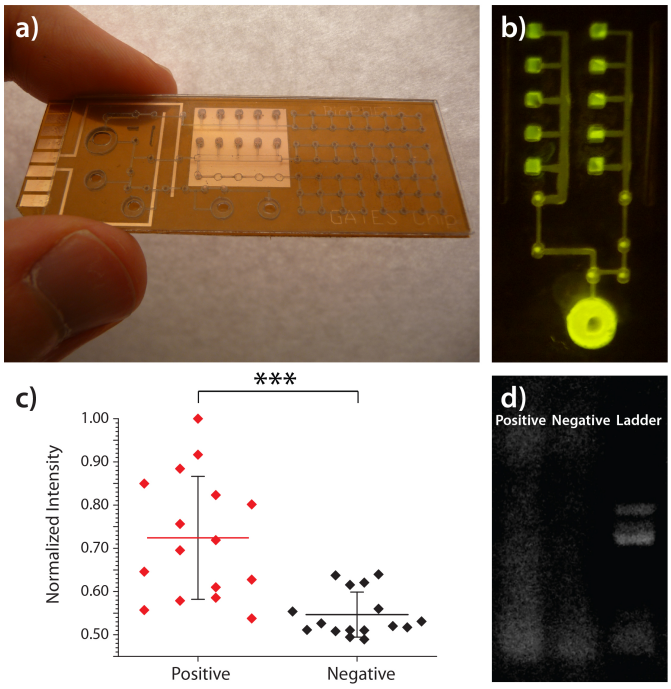

Figure 3.12: a) New version of sample preparation device with SD-interface and integrated ELISA and LAMP detection components. b) LAMP was performed on-chip with premixed reagents and fluorescent images were acquired. c) A statistically significant difference was observed between positive and negative controls. d) Amplification was verified by the amplicon smear observed in the positive column of the gel.

The inter-person variability of detection with LAMP is relatively unknown as inhibitors that are variable to each person, such as hemoglobin, chelators, proteases, and immunoglobulins, disrupt proper amplification. One solution is to dilute the samples to decrease the concentration of the inhibitors. To test the amount of dilution necessary, a TB target was spiked into plasma samples at different dilutions and LAMP was performed off-chip using a Bio-Rad CFX96 Real-time Detection System at 65°C. The plasma was separated from blood at either 3 or 7 days post-collection to investigate dependence upon the age of the blood. (Fig. 3.13) A comparison of the C_t (cycle threshold) times between plasma taken from a 34 and 64 years old, shows that there is inter-person variability at 2% dilution, however a 5% dilution does not amplify. (Fig. 3.13a and 3.13b) Plasma separated from 7 day old blood will amplify at 10% dilution, likely due to degradation in the inhibitors. (Fig. 3.13c and 3.13d) No amplification was observed in any dilution of whole blood. This analysis demonstrates that pathogen detection in plasma from fresh blood is more difficult than with stored blood, a problem that will need to be addressed for molecular diagnostics at the point-of-care. Sample dilution is one solution, however this reduces the sensitivity of the assay especially if dilutions close to 1% are needed. Another potential solution is to utilize protease, chelator, and immunoglobulin inhibitors. These reagents could be stored on-chip and rehydrated with the sample.

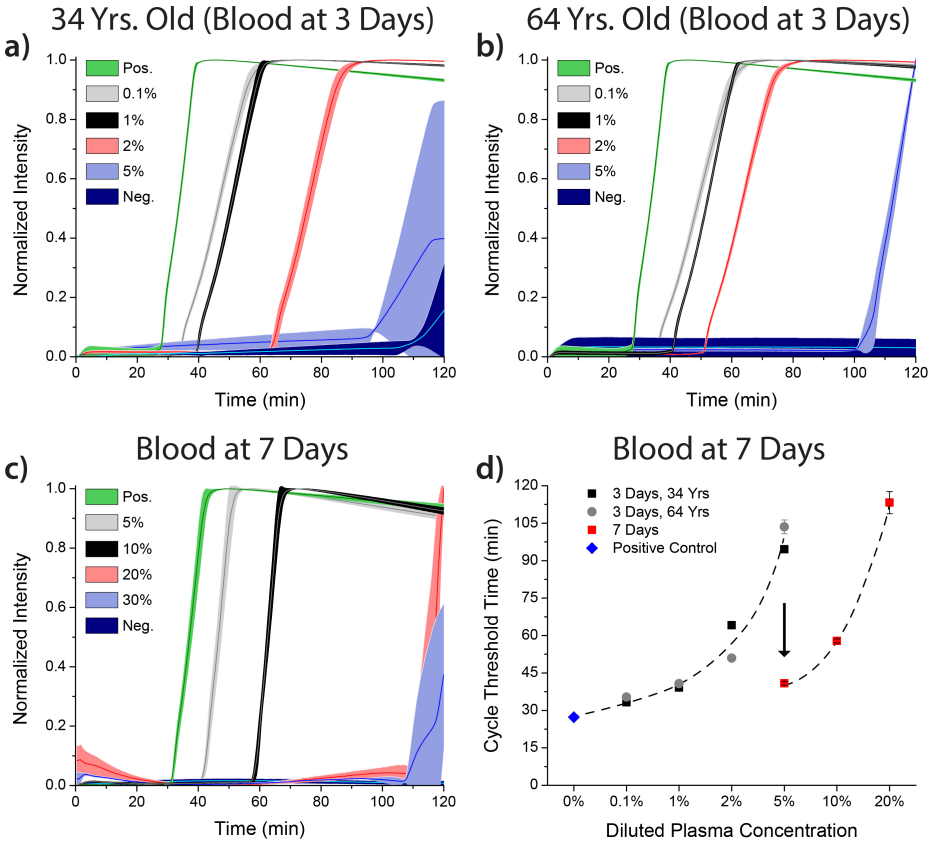

Figure 3.13: Analysis of inter-person variability and plasma dilution necessary for pathogen detection with LAMP. Less dilution was necessary for plasma separated from older blood due to degradation in inhibitors.

The second component of integrating detection on-chip is an ELISA component for antigen detection. Realization of an autonomous ELISA diagnostic system has been one of the longstanding "holy grails" of the microfluidic community. Significant progress has been achieved towards this realization, however very few sample-to-answer systems have been developed.[26,73,74] The current methods require user-mediated fluidic control (thus introducing variability),[75,76] external pumps that limit portability,[43,77] or device disassembly followed by a wash with a fluorescent antibody/label.[25] A beneficial characteristic of degas-driven flow is that the device geometry can be designed such that sequential flow of different reagents over an on-chip detection region can be accomplished autonomously. (Fig. 3.14) Traditional ELISA assays have five main fluid components: sample, wash, primary antibody, secondary antibody (conjugated to an enzyme), and colorimetric substrate. Development of an autonomous device component that can sequentially inject fluids may enable disposable microfluidic ELISA systems at the point-of-care.

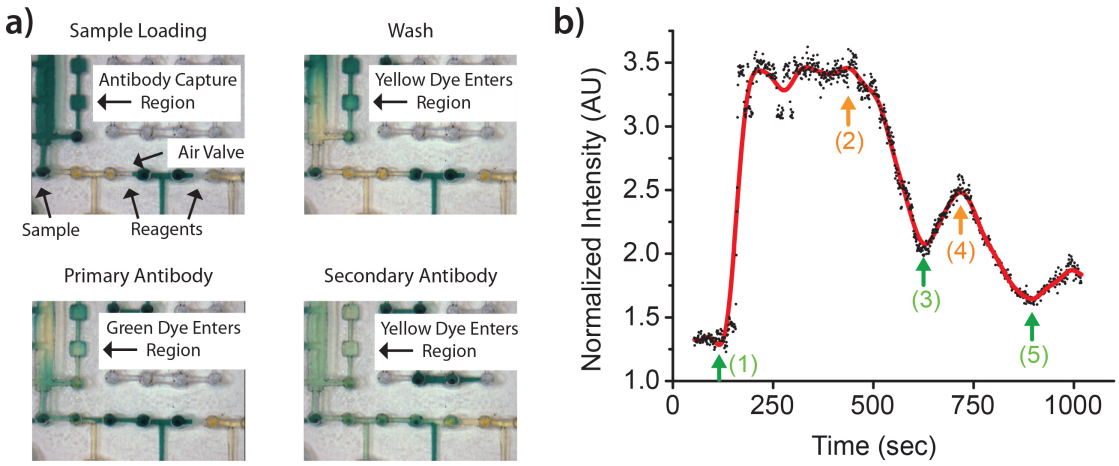

Figure 3.14: a) Demonstration of the sequential injection of five fluids: green, yellow, green, yellow, and green food coloring diluted 100x in water. b) Green intensity measurements were recorded from a square detection well representing where capture antibody would be conjugated. All five fluids were detectable.

A characteristic of degas-driven fluid flow is that when two fluids travel toward a junction, the fluid that reaches the intersection first will dominate and an air gap will prevent the second flow from continuing. These air gaps can be used as "timing valves" that slowly dissolve into the porous silicone layer allowing timed sequential flows. (Fig. B3) Once the second flow touches the first fluid, the second flow dominates. This is analogous to an electrical circuit shorting as the second fluid has a large pressure gradient across it (dP/dx) in comparison to the first fluid, which covers a larger channel distance, dx. The second fluid will effectively dominate until the pressure gradient for both fluids equilibrates and stabilizes. The intentional placement of "T-junctions" can create air valves that slowly dissolve into the porous silicone layer. (Fig. 3.14a) By changing the length of the distance between the "T-junctions," reagents can sequentially be injected into the device. Figure 3.14 demonstrates the sequential injection of alternating green, yellow, green, and yellow food coloring diluted 100x in water. Green color intensity is

mapped in Fig. 314b and reveals each of five flows through a square observation well where the measurements were recorded. The ability to inject five fluids suggests that on-chip ELISA might be a possibility. An added benefit of this system is that the flow does not start until the sample (blood) is added to the inlet since degas-driven flow will not initiate inside the device until all the ports are sealed. This feature allows autonomous flow to only occur upon placement of the sample at the inlet and may simplify further device development.

3.7 Conclusion and Future Directions

This chapter has described the development of a microfluidic sample preparation module to separate plasma from whole blood while simultaneously extracting pathogenic biomarkers by electrochemical lysis. Fluidic actuation is provided by degas-driven fluid flow and a USB/SD interface delivers electrical power for cell lysis. Although the device is designed to detect the three most burdensome diseases in the world: HIV, TB, and Malaria, the sample preparation module is in fact a universal device that has applicability for the detection of other diseases where nucleic acid and protein-based biomarkers reside in the blood. Downstream detection methods such as ELISA and nucleic acid amplification (LAMP) have been investigated and are employed in the second device. This project is part of a multi-year endeavor and is continually being optimized.

One issue that will ultimately need to be addressed is the interface match between our device and how the blood sample is obtained, transferred to the device, and initiation of device operation. Integration of a fingerstick unit or interface with a universal blood collection tube (if phlebotomy is required) may be necessary to ensure proper device loading and consideration of downstream components to prevent device malfunction. Current methods of manual device loading by pipette intrinsically introduce operator error. One function to be investigated are operations that rupture the device seal, possibly coupled with the fingerstick unit, such that device degassing and sample loading begin consistently at the time-of-assay without user dependence or variability.

Methods other than LAMP and ELISA for downstream detection are being considered such as RPA and gold/silver nanoparticle enabled immunoassays. Integrating detection capabilities on-chip eliminates external equipment and may decrease costs for performing the assay. Ideally, the detection components of the device would be colorimetric technologies that could be operated without peripheral accessories (e.g. fluorometric readers, Peltier heaters). Furthermore, device manufacturability was repeatedly considered during device design as elastomeric casting and hot embossing fabrication techniques have limited feasibility and throughput. The layer-by-layer assembly is the most versatile method for prototyping, allowing rapid redesign of the chip and potentially leading to fabrication by roll-to-roll assembly methods.

3.8 Acknowledgements

Portions of this work were performed with Debkishore Mitra (electrochemical lysis and LAMP) and Jixiao (Sean) Liu (LAMP fluorescent imaging). The laminated

device fabrication would not have been possible without advice from Erh-Chia (Charlie) Yeh and Ivan K. Dimov. Charlie Yeh was particularly instrumental in acquiring the materials necessary for fabrication. Financial support was provided by a grant from the Bill & Melinda Gates Foundation (Global Health Grant: OPP1028785).

3.9 REFERENCES

1. Dimov, I. K. *et al.* Stand-alone self-powered integrated microfluidic blood analysis system (SIMBAS). *Lab Chip* **11**, 845–850 (2011).
2. Mukhopadhyay, R. Microfluidics: on the slope of enlightenment. *Anal Chem* **81**, 4169–4173 (2009).
3. Ma, C. *et al.* A clinical microchip for evaluation of single immune cells reveals high functional heterogeneity in phenotypically similar T cells. *Nat Med* **17**, 738–743 (2011).
4. Dalerba, P. *et al.* Single-cell dissection of transcriptional heterogeneity in human colon tumors. *Nat Biotechnol* **29**, 1120–1127 (2011).
5. Balagaddé, F. K., You, L., Hansen, C. L., Arnold, F. H. & Quake, S. R. Long-term monitoring of bacteria undergoing programmed population control in a microchemostat. *Science* **309**, 137–140 (2005).
6. Wang, J., Fan, H. C., Behr, B. & Quake, S. R. Genome-wide Single-Cell Analysis of Recombination Activity and De Novo Mutation Rates in Human Sperm. *Cell* **150**, 402–412 (2012).
7. Kim, S. *et al.* High-throughput single-molecule optofluidic analysis. *Nat Meth* **8**, 242–245 (2011).
8. Fan, H. C. *et al.* Non-invasive prenatal measurement of the fetal genome. *Nature* **487**, 320–324 (2012).
9. Jiang, N. *et al.* Determinism and stochasticity during maturation of the zebrafish antibody repertoire. *P Natl Acad Sci Usa* **108**, 5348–5353 (2011).
10. White, A. K. *et al.* High-throughput microfluidic single-cell RT-qPCR. *P Natl Acad Sci Usa* **108**, 13999–14004 (2011).
11. Agresti, J. J. *et al.* Ultrahigh-throughput screening in drop-based microfluidics for directed evolution. *P Natl Acad Sci Usa* **107**, 4004–4009 (2010).
12. Yuen, P. K. *et al.* Microchip module for blood sample preparation and nucleic acid amplification reactions. *Genome Res.* **11**, 405–412 (2001).
13. Urdea, M. *et al.* Requirements for high impact diagnostics in the developing world. *Nature* **444**, 73–79 (2006).
14. Yang, S., Undar, A. & Zahn, J. D. A microfluidic device for continuous, real time blood plasma separation. *Lab Chip* **6**, 871–880 (2006).
15. Chen, X., Cui, D. & Chen, J. Design, fabrication and characterization of nano-filters in silicon microfluidic channels based on MEMS technology. *Electrophoresis* **30**, 3168–3173 (2009).
16. Thorslund, S., Klett, O., Nikolajeff, F., Markides, K. & Bergquist, J. A hybrid poly(dimethylsiloxane) microsystem for on-chip whole blood filtration optimized for steroid screening. *Biomed Microdevices* **8**, 73–79 (2006).
17. Kim, Y. C., Kim, S.-H., Kim, D., Park, S.-J. & Park, J.-K. Plasma extraction in a capillary-driven microfluidic device using surfactant-added

poly(dimethylsiloxane). *Sensor Actuat B-Chem* **145**, 861–868 (2010).
18. Focke, M. *et al.* Microstructuring of polymer films for sensitive genotyping by real-time PCR on a centrifugal microfluidic platform. *Lab Chip* **10**, 2519–2526 (2010).
19. Wilson, I. G. Inhibition and facilitation of nucleic acid amplification. *Appl Environ Microb* **63**, 3741–3751 (1997).
20. Svanes, K. & Zweifach, B. W. Variations in Small Blood Vessel Hematocrits Produced in Hypothermic Rats by Micro-Occlusion. *Microvascular research* **1**, 210–220 (1963).
21. Fung, Y. C. & Zweifach, B. W. Microcirculation: Mechanics of Blood Flow in Capillaries. *Annu. Rev. Fluid Mech.* **3**, 189–210 (1971).
22. Fung, Y.-C. Stochastic Flow in Capillary Blood-Vessels. *Microvascular research* **5**, 34–48 (1973).
23. Yen, R. T. & Fung, Y. C. Effect of velocity of distribution on red cell distribution in capillary blood vessels. *Am. J. Physiol.* **235**, H251–7 (1978).
24. Yang, S., Undar, A. & Zahn, J. D. Blood plasma separation in microfluidic channels using flow rate control. *ASAIO J* **51**, 585–590 (2005).
25. Fan, R. *et al.* Integrated barcode chips for rapid, multiplexed analysis of proteins in microliter quantities of blood. *Nat Biotechnol* (2008).doi:10.1038/nbt.1507
26. Qin, L., Vermesh, O., Shi, Q. & Heath, J. R. Self-powered microfluidic chips for multiplexed protein assays from whole blood. *Lab Chip* **9**, 2016–2020 (2009).
27. Huang, C.-T., Li, P.-N., Pai, C.-Y., Leu, T.-S. & Jen, C.-P. Design and Simulation of a Microfluidic Blood-Plasma Separation Chip Using Microchannel Structures. *Separation Science and Technology* **45**, 42–49 (2009).
28. Kersaudy-Kerhoas, M., Kavanagh, D. M., Dhariwal, R. S., Campbell, C. J. & Desmulliez, M. P. Y. Validation of a blood plasma separation system by biomarker detection. *Lab Chip* **10**, 1587–1595 (2010).
29. Jain, A. & Munn, L. L. Biomimetic postcapillary expansions for enhancing rare blood cell separation on a microfluidic chip. *Lab Chip* **11**, 2941–2947 (2011).
30. Chakraborty, S. Dynamics of capillary flow of blood into a microfluidic channel. *Lab Chip* **5**, 421–430 (2005).
31. Crowley, T. A. & Pizziconi, V. Isolation of plasma from whole blood using planar microfilters for lab-on-a-chip applications. *Lab Chip* **5**, 922 (2005).
32. VanDelinder, V. & Groisman, A. Separation of plasma from whole human blood in a continuous cross-flow in a molded microfluidic device. *Anal Chem* **78**, 3765–3771 (2006).
33. Chung, K. H. *et al.* Magnetically-actuated blood filter unit attachable to pre-made biochips. *Lab Chip* (2012).doi:10.1039/c2lc40529f
34. Shim, J. S., Browne, A. W. & Ahn, C. H. An on-chip whole blood/plasma separator with bead-packed microchannel on COC polymer. *Biomed Microdevices* **12**, 949–957 (2010).
35. Shim, J. S. & Ahn, C. H. An on-chip whole blood/plasma separator using hetero-packed beads at the inlet of a microchannel. *Lab Chip* (2012).doi:10.1039/c2lc21009f
36. Li, C., Liu, C., Xu, Z. & Li, J. A power-free deposited microbead plug-based microfluidic chip for whole-blood immunoassay. *Microfluid Nanofluid* **12**, 829–

834 (2012).
37. Maheswaran, S. *et al.* Detection of mutations in EGFR in circulating lung-cancer cells. *N Engl J Med* **359**, 366–377 (2008).
38. Zhang, X.-B. *et al.* Gravitational sedimentation induced blood delamination for continuous plasma separation on a microfluidics chip. *Anal Chem* **84**, 3780–3786 (2012).
39. Wetteland, P., Røger, M., Solberg, H. E. & Iversen, O. H. Population-based erythrocyte sedimentation rates in 3910 subjectively healthy Norwegian adults. A statistical study based on men and women from the Oslo area. *J. Intern. Med.* **240**, 125–131 (1996).
40. Haeberle, S., Brenner, T., Zengerle, R. & Ducrée, J. Centrifugal extraction of plasma from whole blood on a rotating disk. *Lab Chip* **6**, 776–781 (2006).
41. Steigert, J. *et al.* Integrated siphon-based metering and sedimentation of whole blood on a hydrophilic lab-on-a-disk. *Biomed Microdevices* **9**, 675–679 (2007).
42. Cho, Y.-K. *et al.* One-step pathogen specific DNA extraction from whole blood on a centrifugal microfluidic device. *Lab Chip* **7**, 565 (2007).
43. Lee, B. S. *et al.* Fully integrated lab-on-a-disc for simultaneous analysis of biochemistry and immunoassay from whole blood. *Lab Chip* **11**, 70–78 (2011).
44. Lutz, S. *et al.* Microfluidic lab-on-a-foil for nucleic acid analysis based on isothermal recombinase polymerase amplification (RPA). *Lab Chip* **10**, 887 (2010).
45. Focke, M., Stumpf, F., Roth, G., Zengerle, R. & Stetten, von, F. Centrifugal microfluidic system for primary amplification and secondary real-time PCR. *Lab Chip* **10**, 3210–3212 (2010).
46. Madou, M. J., Lee, L. J., Daunert, S., Lai, S. & Shih, C.-H. Design and Fabrication of CD-Like Microfluidic Platforms for Diagnostics: Microfluidic Functions. *Biomed Microdevices* **3**, 245–254 (2001).
47. Lee, L. J. *et al.* Design and Fabrication of CD-Like Microfluidic Platforms for Diagnostics: Polymer-Based Microfabrication. *Biomed Microdevices* **3**, 339–351 (2001).
48. Mahalanabis, M., Al-Muayad, H., Kulinski, M. D., Altman, D. & Klapperich, C. M. Cell lysis and DNA extraction of gram-positive and gram-negative bacteria from whole blood in a disposable microfluidic chip. *Lab Chip* **9**, 2811–2817 (2009).
49. Carlo, D. D., Jeong, K.-H. & Lee, L. P. Reagentless mechanical cell lysis by nanoscale barbs in microchannels for sample preparation. *Lab Chip* **3**, 287 (2003).
50. Siegrist, J. *et al.* Validation of a centrifugal microfluidic sample lysis and homogenization platform for nucleic acid extraction with clinical samples. *Lab Chip* **10**, 363–371 (2010).
51. Kim, J. *et al.* Cell lysis on a microfluidic CD (compact disc). *Lab Chip* **4**, 516–522 (2004).
52. Di Carlo, D., Ionescu-Zanetti, C., Zhang, Y., Hung, P. & Lee, L. P. On-chip cell lysis by local hydroxide generation. *Lab Chip* **5**, 171–178 (2005).
53. Lee, D. W. & Cho, Y.-H. A continuous electrical cell lysis device using a low dc voltage for a cell transport and rupture. *Sensor Actuat B-Chem* **124**, 84–89 (2007).
54. Lee, J.-G. *et al.* Microchip-based one step DNA extraction and real-time PCR in

one chamber for rapid pathogen identification. *Lab Chip* **6**, 886–895 (2006).
55. Liu, R. H., Yang, J., Lenigk, R., Bonanno, J. & Grodzinski, P. Self-Contained, Fully Integrated Biochip for Sample Preparation, Polymerase Chain Reaction Amplification, and DNA Microarray Detection. *Anal Chem* **76**, 1824–1831 (2004).
56. Tomita, N., Mori, Y., Kanda, H. & Notomi, T. Loop-mediated isothermal amplification (LAMP) of gene sequences and simple visual detection of products. *Nat Protoc* **3**, 877–882 (2008).
57. Piepenburg, O., Williams, C. H., Stemple, D. L. & Armes, N. A. DNA Detection Using Recombination Proteins. *PLoS Biol* **4**, e204 (2006).
58. Wang, C.-H., Lien, K.-Y., Wu, J.-J. & Lee, G.-B. A magnetic bead-based assay for the rapid detection of methicillin-resistant Staphylococcus aureus by using a microfluidic system with integrated loop-mediated isothermal amplification. *Lab Chip* **11**, 1521–1531 (2011).
59. Mukhopadhyay, R. When PDMS isn't the best. What are its weaknesses, and which other polymers can researchers add to their toolboxes? *Anal Chem* **79**, 3248–3253 (2007).
60. Baumler, H., Neu, B., Donath, E. & Kiesewetter, H. Basic phenomena of red blood cell rouleaux formation. *Biorheology* **36**, 439–442 (1999).
61. Barshtein, G., Tamir, I. & Yedgar, S. Red blood cell rouleaux formation in dextran solution: dependence on polymer conformation. *Eur. Biophys. J.* **27**, 177–181 (1998).
62. Barletta, J. M., Edelman, D. C. & Constantine, N. T. Lowering the detection limits of HIV-1 viral load using real-time immuno-PCR for HIV-1 p24 antigen. *Am. J. Clin. Pathol.* **122**, 20–27 (2004).
63. Etschel, J. K. *et al.* HIV-1 mRNA electroporation of PBMC: A simple and efficient method to monitor T-cell responses against autologous HIV-1 in HIV-1-infected patients. *Journal of Immunological Methods* **380**, 40–55 (2012).
64. Goodridge, A. *et al.* Anti-phospholipid antibody levels as biomarker for monitoring tuberculosis treatment response. *Tuberculosis* **92**, 243–247 (2012).
65. Wu, J. *et al.* Analysis of microRNA expression profiling identifies miR-155 and miR-155* as potential diagnostic markers for active tuberculosis: a preliminary study. *Human Immunology* **73**, 31–37 (2012).
66. Ma, F. *et al.* The microRNA miR-29 controls innate and adaptive immune responses to intracellular bacterial infection by targeting interferon-γ. *Nat Immunol* **12**, 861–869 (2011).
67. Fu, Y., Yi, Z., Wu, X., Li, J. & Xu, F. Circulating MicroRNAs in Patients with Active Pulmonary Tuberculosis. *J Clin Microbiol* **49**, 4246–4251 (2011).
68. Luchavez, J. *et al.* Laboratory demonstration of a prozone-like effect in HRP2-detecting malaria rapid diagnostic tests: implications for clinical management. *Malaria J* **10**, 286 (2011).
69. Makler, M. T. *et al.* Parasite Lactate-Dehydrogenase as an Assay for Plasmodium-Falciparum Drug-Sensitivity. *Am J Trop Med Hyg* **48**, 739–741 (1993).
70. Martin, S. K., Rajasekariah, G.-H., Awinda, G., Waitumbi, J. & Kifude, C. Unified Parasite Lactate Dehydrogenase and Histidine-Rich Protein ELISA for Quantification of Plasmodium falciparum. *Am J Trop Med Hyg* **80**, 516–522 (2009).

71. Piper, R. C., Buchanan, I., Choi, Y. H. & Makler, M. T. Opportunities for improving pLDH-based malaria diagnostic tests. *Malaria J* **10**, 213 (2011).
72. Murphy, S. C. *et al.* Real-Time Quantitative Reverse Transcription PCR for Monitoring of Blood-Stage Plasmodium falciparum Infections in Malaria Human Challenge Trials. *Am J Trop Med Hyg* **86**, 383–394 (2012).
73. Wang, J. *et al.* A self-powered, one-step chip for rapid, quantitative and multiplexed detection of proteins from pinpricks of whole blood. *Lab Chip* **10**, 3157–3162 (2010).
74. Kai, J. *et al.* A novel microfluidic microplate as the next generation assay platform for enzyme linked immunoassays (ELISA). *Lab Chip* (2012).doi:10.1039/c2lc40585g
75. Chin, C. D. *et al.* Microfluidics-based diagnostics of infectious diseases in the developing world. *Nat Med* **17**, 1015–1019 (2011).
76. Park, S. W., Lee, J. H., Kim, K.-I., Yoon, H. C. & Yang, S. S. An electrochemical immunosensing lab-on-a-chip integrated with latch mechanism for hand operation. *J. Micromech. Microeng.* **19**, 025024 (2009).
77. Stevens, D. Y. *et al.* Enabling a microfluidic immunoassay for the developing world by integration of on-card dry reagent storage. *Lab Chip* **8**, 2038–2045 (2008).

CHAPTER 4

BLOOD COAGULATION CHIP FOR INR VALUE AND HEMATOCRIT DETERMINATION

4.1 ABSTRACT

Previously, the method of degas-driven fluid flow was demonstrated as a method to actuate fluids for the autonomous preparation of blood for biomolecular-based assays, enabling fluid logic and sample mixing with up to five reagents. Unlike the blood sample preparation device, which requires external components to quantify LAMP fluorescence and ELISA absorbance, the autonomous blood coagulation chip presented in this chapter is a stand-alone device. Here, a simple technique is presented to visually quantify coagulation and hematocrit, essential phenotypic properties of blood. Close to 1% of the American population is routinely administered anticoagulant prophylaxes to prevent thromboembolism. However, the self-management of anticoagulant therapy has largely gone unadopted even though consensus agrees that implementation would be beneficial, improve quality of life, and decrease mortality. The simultaneous measurement of hematocrit in addition to the INR value enables the recognition of asymptomatic hemorrhage, a fatal side effect of anticoagulant therapy. To date, none of the commercial coagulation monitors have applied this measurement for screening. Unlike current electronic devices for self-monitoring, the coagulation chip in this chapter presents a power-free device model more closely related to the lateral flow assay, potentially enabling better adoption of self-monitoring.

4.2 INTRODUCTION

The administration of anticoagulants has become a routine healthcare tool to prevent and combat a number of patient health problems. The prescription of oral anticoagulants (e.g. coumarins, direct thrombin inhibitors, etc.) is typically used as a long-term prophylaxis to prevent thrombosis in a number of "chronic" situations. For example, this includes patients with long-term health concerns such as atrial fibrillation, past episodes of embolism or stroke, inherited/acquired thrombophilic disorders, and the mitigation of post-operative health risks for surgeries such as prosthetic heart valve replacement, coronary artery stent implantation, or orthopedic surgery (e.g. knee or hip replacements). As a result of the widespread use of anticoagulants, 2.5 million Americans now rely on blood thinners annually. However, the most commonly used oral anticoagulants, coumarins, have a number of adverse side effects that require continual blood monitoring and regular alteration of the drug dosage administered to the patient. The activity of coumarins, which are vitamin K antagonists, responds to a number of factors such as diet (foods high in vitamin K, cranberries, green vegetables), liver, kidney, and thyroid dysfunction, alcohol, several herbs and spices, and many common

use drugs such as aspirin and certain antibiotics.[1,2] Consequently, beginning in 2005 the International Self-Monitoring Association for Oral Anticoagulation reviewed and advocated for the increased practice of patient self-testing as a means to counter the variability in initial dose selection and stabilization, as well as mitigating long-term difficulties in maintaining anticoagulant stability.[3] The following are five of the major identified benefits of self-monitoring reported by the International Self-Monitoring Association for Oral Anticoagulation:

1) Decreased risk of death from hemorrhage and thromboembolism
2) Faster means to counter coagulation variability
3) Improved quality of life
4) Greater cost-effectiveness and reduced clinical burden
5) Patient education

The consensus of systematic comparisons in literature agree that patient self-monitoring and self-management leads to equal, if not reduced incidence of thromboembolism, major hemorrhage, and mortality in comparison to traditional clinical management.[4-9] However, even with the known evidence of these benefits, patient uptake of self-management has been difficult to implement. One study found a reduced uptake of self-monitoring by patients over 85 years of age, possibly due to a reluctance to participate in self-monitoring and an already established reliance on routine healthcare practices.[4] An economic study in the United Kingdom recently found patient self-management to be more expensive than routine care by $150,937 per quality-adjusted life-year (QALY), requiring a cost-effectiveness threshold of $37,000 per QALY gained with self-monitoring.[7] However, because the population of patients on coagulation therapy is largely elderly and retired, the estimated probability that self-management is cost effective based on QALY gained is only 44%. (A 50% probability would indicate no gain or loss.) Thus, the economic impact is marginal to a slight loss, however the benefits are largely attained through improvements in quality of life and gained independence.

The most common form and best example of patient self-management is the widespread adoption of glucose monitors to manage diabetes. In comparison to glucose monitors, a number of self-monitors for coagulation are available such as the Roche CoaguChek®, ITC ProTime®, and HemoSense INRatio®. However, these devices cost $500 to $2,000, almost 100x more than glucose monitors. In contrast, glucose monitors can generally be purchased for less than $20. A number of factors cause this price differential. One aspect is that some coagulation monitors rely on more expensive technology like the CoaguChek®, which detects the proteolytic cleavage of a fluorescent peptide, and the ProTime®, which actuates blood back and forth in a capillary until clot formation occurs. However, other monitors such as the INRatio, which electrochemically measures a change in impedance due to clot formation, are much cheaper and use similar technologies to a glucose monitor, but still cost in excess of $500. Such evidence indicates that slow user adoption has not created a sustainable market that can survive upon small profit margins, thus leading to the inflated price of blood monitors. To compound this issue, patient self-testing occurs on a monthly to weekly basis. This is a stark contrast to diabetics who test on a daily basis, perhaps as many as 3-10 times per day, thus using more consumables. One factor that might advance the adoption of

coagulation self-monitoring is a cheap and simplified product that emulates a pregnancy lateral flow assay. Even though pregnancy tests are used infrequently, their simplicity and robustness enable widespread accessibility in pharmacies. To this end, this chapter describes an attempt to develop a blood coagulation chip with attributes more similar to a disposable lateral flow assay than to a glucose monitor.

The self-powered, disposable blood coagulation chip proposed in this chapter can simultaneously monitor coagulation time and hematocrit. Prothrombin time (PT) measures the clotting tendency of blood by way of the extrinsic coagulation pathway and is the most common technique used to determine the International Normalized Ratio (INR). The INR value is defined:

$$INR = \left(\frac{PT_{Test}}{PT_{Normal}} \right)^{ISI} \tag{4.1}$$

where the patient's prothrombin time (measured in seconds) is normalized to a control sample, typically the Pooled Normal Plasma (PNP) of 50 or more individuals. The tissue factor used to initiate coagulation in the assay is standardized with an International Sensitivity Index (ISI) to account for variations between different manufacturers. The dosage level of anticoagulant that is administered to a patient is determined from the INR, with lower values indicating a risk of unwanted clotting. Typical INR values are between 0.8-1.2 for healthy individuals and greater than 2.0 for patients on anticoagulant therapy.

To design a tool to to monitor coagulation, the coagulation cascade first needs to be understood. The coagulation cascade is a series of reactions that mostly consist of serine protease precursors that become activated by enzymatic cleavage and then catalyze the next reaction in the pathway. (Fig. 4.1) Two initial pathways, the intrinsic and extrinsic pathways, are activated by different initiators and lead to activation of the common pathway and fibrin cross-linking. The extrinsic pathway is activated by cellular trauma and thromboplastin, cellular-based mixture consisting of tissue factor (III), calcium, and phospholipids, which is often used as an initiator to mimic trauma. It is by this pathway that the INR value is determined. The intrinsic pathway is activated by phospholipid, calcium, and an activator such as silica. Coagulation times measured by the initiation of this pathway are called "activated partial thromboplastin time" (aPTT) due to the absence of the last constituent of thromboplastin, tissue factor III. Blood clotting disorders can be identified by the direct addition of downstream tissue factors to probe abnormalities in the coagulation cascade. A recombinant form of tissue factor VIIa, known as NovoSeven®, is often used in hospital trauma units to initiate clotting in patients with episodes of hemophilia and uncontrollable bleeding. Figure 4.1 shows the methods of inhibition for two commonly used anticoagulants: heparin (blue) and warfarin (red). Heparin inhibits coagulation by binding antithrombin III, causing allosteric changes that enhance the inhibitory properties of antithrombin III and leading to increased inactivation kinetics up to 10,000x.[10] Warfarin inhibits vitamin K epoxide reductase, resulting in decreased concentrations of vitamin K and vitamin K epoxide. This action inhibits the ability of glutamyl carboxylase to carboxylate the glutamic acid residues of the coagulation factors II (prothrombin), VII, IX, and X. Carboxylation is

necessary for the factors to bind the phospholipid surfaces inside the vascular endothelium.[11]

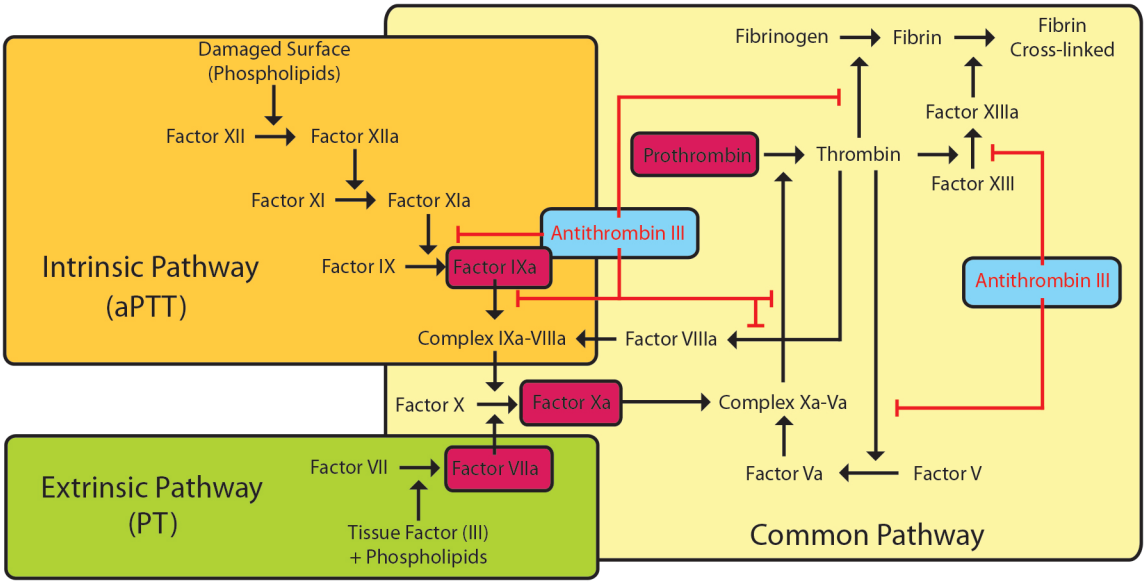

Figure 6.1: The coagulation cascade is initiated by the intrinsic (orange) and extrinisic (green) pathways leading to activation of the common pathway (yellow). The mechanisms by which heparin (blue) and warfarin (red) inhibit coagulation are depicted with red lines.

The most common side effect of anticoagulant administration is hemorrhage. As many as 7.3% of patients taking anticoagulants report annual incidents of major hemorrhage and mortality rates as high as 4.1% have been reported.[9] Hematocrit, the volume percentage of red blood cells in blood, is an important indicator of homeostasis in blood. An abnormally low hematocrit level may indicate internal bleeding due to the loss of circulating blood cells. Hematocrit measurement has not been incorporated into commercial self-monitors and its addition would be a vital tool in identifying asymptomatic internal bleeding.

4.3 The Blood Coagulation Chip

The self-powered blood chip proposed in this chapter utilizes degas-driven fluid flow to drive blood within the microchannels of the chip. A droplet of blood, placed at the inlet of the chip, is propelled by atmospheric pressure into the microchannels. For the purposes of rapid prototyping, we use the polymer polydimethylsiloxane (PDMS), which is commonly used to fabricate microfluidic devices. Other polymers could be employed that are better suited for mass fabrication such as polystyrene or cyclic Olefin Copolymer (COC), however a silicone component would need to be integrated into the chip to enable degassing. Chapter 2 analyzed alternative materials for the mass-fabrication of monolithic devices powered by degas-driven fluid flow. The chip is vacuum packaged to enable storage and prolong shelf life for fluidic actuation. Blood coagulation chips have retained vacuum for more than 15 minutes upon opening of the packaging. This time is longer than with the sample preparation devices as the entire blood coagulation chip is

produced from PDMS. A drop of blood is placed on the orifice of the device and blood is propelled into the dead end channels inside the chip. (Fig. 4.2) The current version of the chip contains three channels: one channel to measure hematocrit, a second to monitor INR value, and a third to act as a control for the second INR value channel. An on-board lancet could eventually be incorporated into the device, although a separate lancet must be used with the current prototype.

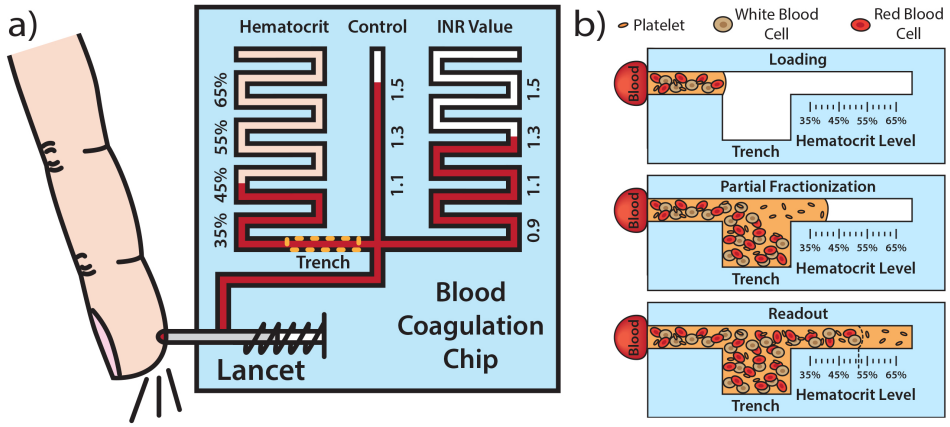

Figure 4.2: a) Schematic of the self-loading polymeric blood coagulation chip that simultaneously measures hematocrit and INR value. b) Hematocrit is determined by partially removing a known volume of cells from blood and allowing the channel to fully load. The interface between transparent plasma and blood, as measured from the end of the channel, yields determination of the hematocrit value.

The device determines INR value by initiating coagulation in the INR value channel and measuring the distance blood flows before coagulation occurs. Blood with a lower INR value travels a shorter distance before coagulation occurs. Due to the transient decay in degassing power, a control channel is necessary to ensure blood flow stops due to coagulation and not to a loss of degassing power. Clotting is initiated *via* the extrinsic pathway with thromboplastin (Tissue Factor (III), calcium, phosphatidylcholine, and phosphatidylserine). For prototyping purposes, a solution of thromboplastin (1 mg/mL) is manually loaded by hand into the device with a syringe *via* sacrificial inlet ports and physio-adsorption occurs onto the sidewalls of the INR value channel. The control channel is loaded with a solution of heparin (100 mg/mL). The device is lyophilized to enable preservation of the reagents and then permanently sealed after preparation to enable long-term storage. The thromboplastin and heparin are reconstituted upon blood flow into the channel and coagulation is either initiated or inhibited. The control channel is used as an end point reference since the idle time the user waits before addition of blood to the inlet port will impact the distance the blood will travel (as the degassing power decays). The lyophilized heparin in the control channel will prevent coagulation and flow in this channel will stop only when degas-driven flow is exhausted. This allows blood to be used in the control channel instead of a second liquid. The two-endpoint distances of blood travel in the INR value and control channels will have a non-linear correlation with the actual INR value. A table provided with the chip will enable determination of the INR value based upon the distance traveled in the INR value and control channels.

The third channel of the chip will measure hematocrit to determine if the patient has excessive bleeding. Hematocrit is measured with a trench geometry that utilizes gravity-based sedimentation to skim plasma from the blood flowing in the chip. (Fig. 4.2b) The trench, which is fabricated to a predetermined volume, is designed to overflow with blood cells, thus creating an observable interface between blood and the transparent plasma. Since the microchannels operate within the laminar flow regime, a stark interface is apparent between the opaque blood cells and plasma. The trench volume is added to the volume of the dead-end channel, as measured from the end of the channel to the edge of the trench. Therefore, the distance the blood/plasma interface travels downstream corresponds to the hematocrit level. Markers imprinted on the chip facilitate user-based visual readout.

4.4 PROTOTYPE DESIGN AND FABRICATION

A preliminary prototype design to demonstrate the concepts of the proposed system is present in Figure 4.3a. Two separate inlets are located at the bottom of the chip (green shading) to test the hematocrit and INR functionalities of the device. The finalized version of the device is envisioned to have one inlet integrated with either a lancet or hollow microneedle array to allow a one-step user protocol. The chip contains five innovative features:

1) Two large vacuum reservoirs to provide excess vacuum within the chip for prolonged degassing power (blue shading)
2) A distribution network to homogeneously provide vacuum throughout the perimeter and internal regions of chip (blue shading)
3) The simultaneous use of these internal channels as rulers to enable a visual and quantitative readout for hematocrit and INR value determination (blue shading)
4) Four sacrificial ports to enable loading of the INR value and control channels with thromboplastin and heparin (red shading)
5) A trench (yellow shading) to skim a predetermined volume of packed cell volume from the plasma with an equal volume end trench allowing hematocrit determination.

The length markings as indicated on the rulers are arbitrary length values to be used for INR value determination. A prototype device is depicted in Figure 4.3b.

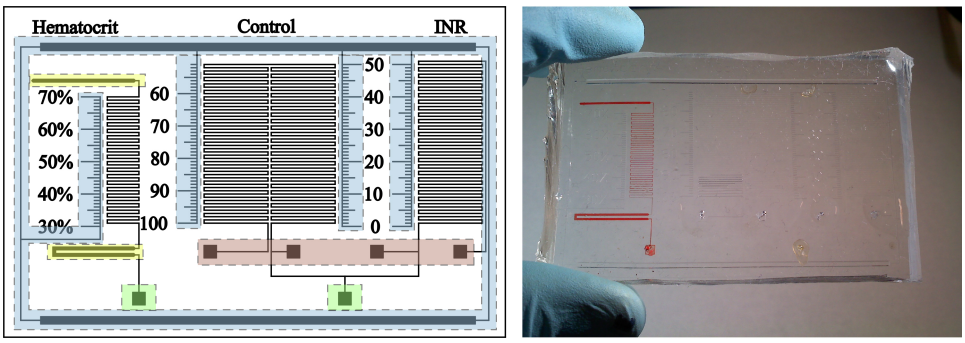

Figure 4.3: (Left) Device design with five innovative features: 1) two vacuum reservoirs with 2) distributing channels to homogenize degassing across the entire chip, which simultaneously act as 3) rulers to quantitate hematocrit and INR determination (blue shading). 4) Sacrificial inlet ports allow control and INR

channels to be primed with coagulant and anticoagulants (red shading). 5) Trench for skimming a known volume of packed cell volume from plasma and equal volume end trench for hematocrit determination (yellow shading). Two inlet ports are shown with green shading. (Right) Prototype version of the chip is made in PDMS and loaded with sheep blood and human plasma.

Prototyping was performed with standard soft lithography and the fabrication steps are outlined in Figure 4.4. The chip was designed in AutoCAD and shadow masks were created for photolithography. (The Photoplot Store) A two-layer silicon wafer mold was created using SU-8 photoresist. (MicroChem Corp.) The first layer was 20 μm and the second trap layer was 200 μm in height. The mold was fluorosilanized to enhance PDMS removal and PDMS was cured on the mold at 65°C. A thin membrane of PDMS was spin coated onto a separate fluorosilanize wafer and the molded PDMS device was bonded to the thin PDMS membrane with O_2 plasma (100W, 300 mTorr). The device was thickened with PDMS to increase the robustness of the device during handling and enhance degassing ability. Ports were punched half-way into the PDMS device and the sacrificial channels were separately primed with 10 μL of thromboplastin (1 mg/mL) and heparin (100 mg/mL). A vacuum hose was utilized to help load the sacrificial channels and the reagents were dried at 37°C overnight, enabling physio-adsorption to the microchannels. The sacrificial channels were closed by curing PDMS on the ports. Finished devices were then degassed in a vacuum of 300 mTorr for 1 hour and vacuum packaged.

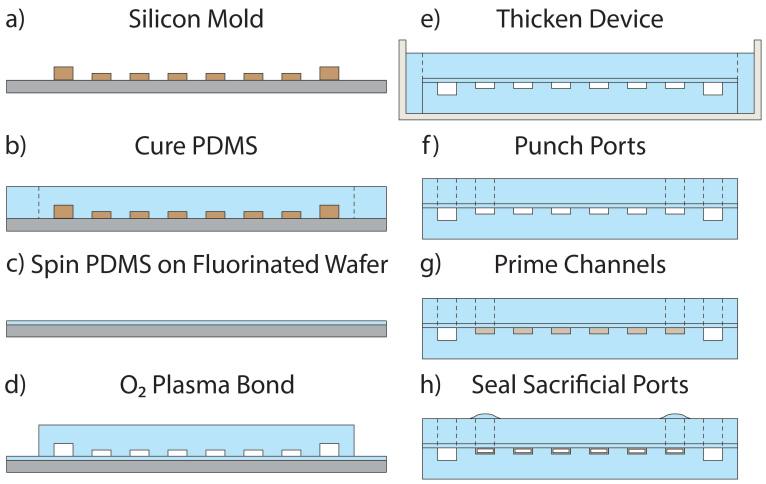

Figure 4.4: Fabrication process flow for blood coagulation chip prototyping.

4.5 Results and Discussion

Preliminary testing was performed with citrated human blood (Zen-Bio, Inc.) with a known hematocrit and Pooled Normal Plasma from 40 donors (George King Bio-Medical, Inc.). The coagulation ability of both reagents was reinitiated with 1M $CaCl_2$, which counters the chelating properties of the sodium citrate. Chips were tested and we observed a longer travel distance for the control channel (heparin) than the INR value channel (thromboplastin), indicating that physio-adsorption of the reagents onto the microchannel is having the intended effects of inducing (thromboplastin) and inhibiting

(heparin) coagulation. Blood was loaded completely into the hemoatocrit channel, indicating that sufficient vacuum was sustained for the duration of loading, which took an average of seven minutes. However, blood flow rate is too fast for sedimentation of the blood cells, even with a 10x height difference between the channel layer and trap height. Only when degas-driven flow began to slow did sedimentation occur. When the device was degassed in vacuum for shorter periods of time, sedimentation of the blood occurred, but the hematocrit channel did not fully load.

The first version of the design had flaws and three more versions were implemented and tested. Some of the problems with the chip included that the length of the INR value channel was too short and pooled normal plasma would flow past the 50 marking on the device. Also, degas-driven fluid flow operated at too high of a flow rate for cell sedimentation to occur in the hematocrit channel. (Fig. 4.5a) We are confident that the concept works as we have demonstrated plasma skimming with a 1 mm deep trench,[12] however device fabrication with this trench height is difficult. We are currently exploring techniques to decrease degassing power as this would solve both problems. Besides decreasing the time the device is degassed in vacuum during preparation, a better approach is to use TPX (polymethylpentene) to create monolithic devices. This polymer is a thermoplastic that can be hot embossed and is less permeable than PDMS, thus facilitating slower degas-driven flow rates. A version of the design with control and INR value channels that are twice the length of the original and with a trench 200 μm deep is currently being evaluated in both PDMS and TPX.

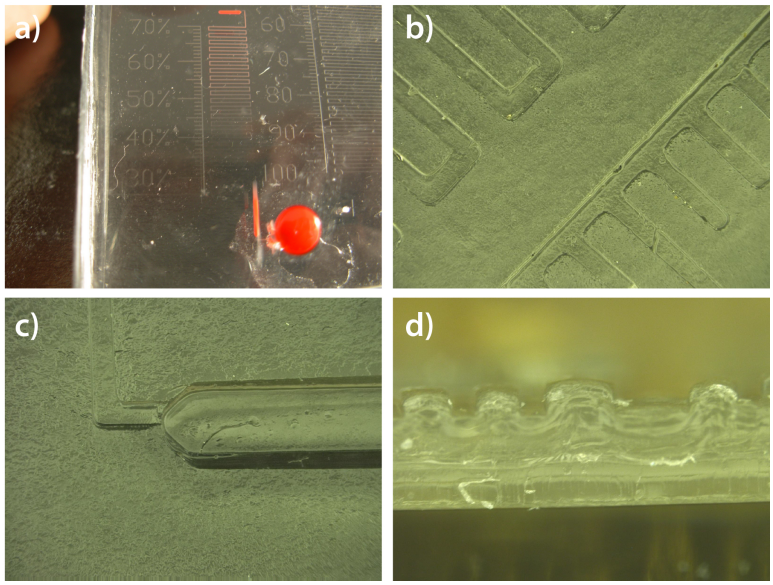

Figure 4.5: a) Degas-driven fluid flow is too fast for cell sedimentation to occur in the hematocrit channel with PDMS devices. Device components from chips fabricated with hot embossed TPX are being investigated. Sidewall geometries show good molding in b) channels and c) trench. d) Cross-section of embossed TPX device.

To hot emboss TPX, a silicon wafer mold is patterned with SU-8. TPX is placed on the mold between two 1/8" stainless steel plates, which act as supports so the silicon

wafer does not fracture. The assembly is positioned on a benchtop shop press (Grizzly Industrial, Inc.), the heating pads are set above the melting temperature of TPX to 200°C, and 1 U.S. Ton of pressure is applied for 30 seconds. Then, the mold, discs, and TPX are cooled with an air gun and the TPX is slowly removed from the SU-8 wafer mold. Figure 4.5 depicts channels, trench, and a cross-section of a device embossed from TPX. Devices are then solvent bonded to a thin TPX membrane with Xylene or a pressure sensitive adhesion layer is applied to the chip to seal the microchannels. Investigations are still continuing with TPX to determine the best method of fabrication and practicality of implementing the blood coagulation chip with this material.

4.6 CONCLUSION

The blood coagulation chip presented in this chapter is an alternative tool for patient self-management that may facilitate the implementation of self-management for individuals who chronically rely on orally administered anticoagulants. In comparison to conventional clinic-based management, self-management has been proven to maintain accurate control of INR values with a decreased occurrence of minor and major hemorrhage. However, user-adoption has been slow. The blood coagulation chip presented in this chapter seeks to augment self-testing through the development of a diagnostic device that simultaneously measures INR value, as well as hematocrit, an indicator for bleeding episodes. The blood coagulation chip is cheap and disposable, drawing a parallel more closely to the lateral flow assay than traditional coagulation monitors. The predicted cost of fabricating 10 million chips is calculated to be $1.02/chip. (Appendix C) This cost is significantly less than current coagulation monitors and may prove to be a highly useful tool for doctors in resource limited settings and developing regions of the world. The chip can ideally be packaged to hold a vacuum for multiple years. All reagents are lyophilized, reconstituted by the blood introduced into the device, and vacuum packaging will further maximize shelf life. We aim to decrease hospital visitation and laboratory diagnostic costs, increase patient education through self-monitoring, and aid in the adoption and practice of self-management for oral anticoagulants.

4.7 ACKNOWLEDGEMENTS

I acknowledge support from a National Science Foundation Graduate Research Fellowship and an award from the Center for Integration of Medicine and Innovative Technology (CIMIT).

4.8 REFERENCES

1. Couris, R. R. *et al.* Development of a self-assessment instrument to determine daily intake and variability of dietary vitamin K. *J Am Coll Nutr* **19**, 801–807 (2000).
2. Kim, K. H. *et al.* Relationship between dietary vitamin K intake and the stability of anticoagulation effect in patients taking long-term warfarin. *Thromb. Haemost.* **104**, 755–759 (2010).

3. Ansell, J. *et al.* Guidelines for implementation of patient self-testing and patient self-management of oral anticoagulation. International consensus guidelines prepared by International Self-Monitoring Association for Oral Anticoagulation. *Int. J. Cardiol.* **99**, 37–45 (2005).
4. Heneghan, C. *et al.* Self-monitoring of oral anticoagulation: systematic review and meta-analysis of individual patient data. *Lancet* **379**, 322–334 (2012).
5. Heneghan, C. *et al.* Self-monitoring of oral anticoagulation: a systematic review and meta-analysis. *Lancet* **367**, 404–411 (2006).
6. Christensen, T. D., Johnsen, S. P., Hjortdal, V. E. & Hasenkam, J. M. Self-management of oral anticoagulant therapy: A systematic review and meta-analysis. *Int. J. Cardiol.* **118**, 54–61 (2007).
7. Connock, M. *et al.* Clinical effectiveness and cost-effectiveness of different models of managing long-term oral anticoagulation therapy: a systematic review and economic modelling. *Health Technol Assess* **11**, iii–iv– ix–66 (2007).
8. Dolan, G., Smith, L. A., Collins, S. & Plumb, J. M. Effect of setting, monitoring intensity and patient experience on anticoagulation control: a systematic review and meta-analysis of the literature. *Curr Med Res Opin* **24**, 1459–1472 (2008).
9. Menéndez-Jándula, B. *et al.* Comparing self-management of oral anticoagulant therapy with clinic management: a randomized trial. *Ann. Intern. Med.* **142**, 1–10 (2005).
10. Johnson, D. J. D., Li, W., Adams, T. E. & Huntington, J. A. Antithrombin–S195A factor Xa-heparin structure reveals the allosteric mechanism of antithrombin activation. *EMBO J* **25**, 2029–2037 (2006).
11. Hirsh, J. *et al.* Oral anticoagulants: mechanism of action, clinical effectiveness, and optimal therapeutic range. *Chest* **119**, 8S–21S (2001).
12. Dimov, I. K. *et al.* Stand-alone self-powered integrated microfluidic blood analysis system (SIMBAS). *Lab Chip* **11**, 845–850 (2011).

CHAPTER 5

HYBRID LATERAL FLOW ASSAY TO MONITOR TUBERCULOSIS PATIENT RESPONSE

5.1 ABSTRACT

Lateral flow assays (LFA) are the current diagnostic gold standard for infectious disease monitoring. However, current LFA techniques that screen for biomarkers in blood require multi-step pipetting of running buffers and use plasma separation membranes that are prone to hemolysis, thus disrupting the sensitivity of the assay. Here, we demonstrate a hybrid LFA system where plasma separation occurs upstream of the assay by cell sedimentation in a microfluidic point-of-care device powered by degas-driven fluid flow. Sedimentation-based separation of cells ensures 100% capture of blood cells without the release of hemoglobin and other biomolecular components that impede immunoassay performance. In this hybrid device, a traditional LFA is coupled to a polymeric microfluidic device and hermetically sealed. Degas-driven fluid flow powers initial device loading with whole blood and subsequent sedimentation-based plasma separation. The microfluidic channel containing the extracted plasma connects with the sample pad of the LFA and capillary action consequently becomes the driving mechanism for fluid actuation. To demonstrate the hybrid LFA platform, an immunoassay was developed to screen for elevated levels of anti-cardiolipin IgM antibodies. The upregulation of anti-phospholipid antibodies in blood is currently used as a biomarker to test for diseases such as Syphilis and Systemic Lupus Erythematosus. The development of the hybrid LFA in this chapter was part of an endeavor to evaluate a hypothesis that anti-cardiolipin antibodies can be employed to monitor Tuberculosis (TB) patient response to drug therapy in resource-limited settings.

5.2 INTRODUCTION

Three diseases alone kill more than 5 million people each year: HIV, Malaria, and TB.[1] The effects of these diseases is most severe in developing regions of the world as resource-limited settings hinder accurate diagnosis leading to poor therapeutic administration. With diagnostic inaccessibility, clinical response often entails the broad dissemination of available drugs on-hand leading to drug overprescription and the emergence of drug-resistant strains.[2,3] It is widely accepted that better diagnostic technology would significantly reduce mortality and morbidity rates for these diseases as well as prevent more than one billion unnecessary treatments each year.[4,5] However, a significant lack of available rapid tests for TB has led to a striking disparity between the current diagnostic capabilities for TB in comparison to HIV and malaria.[6] While cheap LFAs exist for HIV and Malaria suitable for first line screening, there are practically no rapid tests for TB. The diagnostic gold standard remains sputum smear microscopy in

resource-limited regions of the world and interferon-gamma release assays in clinics of the developed world. The fundamental lack of a rapid test compounds with other non-technical barriers such as ineffective advocacy, undertrained end users, and socio-economic cultural difficulties that are common to regions of the world where affliction is greatest. The deficiency of a cheap rapid test for the developing world has contributed to the spread of drug-resistant TB and its prominence as the seventh leading cause of death worldwide and second most fatal infectious disease.[7]

5.3 THE HYBRID LATERAL FLOW ASSAY

The LFA is the current standard platform technology for point-of-care diagnostic testing. These assays are robust, versatile, and simple to use. For more than three decades this technology has been applied to provide an inexpensive and adaptable means of immunoassay-based target identification in biological samples.[8] Recently, there has been an effort to apply the LFA platform to more complex biofluids such as blood. Several commercial entities have responded with the development of new blood filtration membranes compatible with the lateral flow platform such as the Whatman™ Fusion 5 and Pall Corporation Vivid™ membranes.[9-11] Recently developed blood-based LFAs have been employed to assay biomarkers for cardiovascular disease,[12] acute myocardial infarction (troponin),[13] and syphilis.[14] However, commercially approved LFAs employing membrane-based separation require the manual pipetting of a running buffer after the blood sample to ensure complete device loading and wetting of the antigen detection region. Here, we attempt to improve this diagnostic platform by integrating sedimentation-based plasma separation to monitor TB patient response to drug administration. Plasma separation by cell sedimentation can achieve 100% filtration efficiencies[15] and eliminate erythrocytic hemolysis, which is detrimental to immunoassay sensitivity. A microfluidic sedimentation trench component is coupled upstream of the LFA. (Fig. 5.1) The LFA is integrated into the polymeric microfluidic device with pressure sensitive adhesive (PSA) and degas-driven fluid flow actuates blood movement through the microchannels until flow reaches the LFA. The extracted plasma channel interfaces with the sample/conjugate pad of the LFA enabling activation of capillary action characteristic of normal LFA operation. This hybrid LFA design improves upon the existing platform by eliminating the addition of a running buffer and the possibility of membrane-induced erythrocyte rupture.

Our collaborators have recently proposed the use of anti-phospholipid IgM antibody level as a mechanism to monitor TB patient response in smear positive, non-cavitary individuals.[16] This novel *ex vivo* approach to examining treatment response is a promising alternative that would greatly advance current monitoring techniques in the developing world. Treatment of TB infections typically requires long courses of multiple antibiotic therapies lasting upwards of six to nine months in duration. Drug response is observed by repeated screening of patient sputum by acid-fast bacilli smear microscopy or culture for mycobacterium tuberculosis after two months of treatment.[16] In most TB endemic regions of the world, particularly those with limited health resources, sputum culture is rarely performed. Additionally, smear microscopy requires technical expertise and is not highly sensitive as some patients can routinely test negative. Thus, a rapid test

that does not rely upon the detection of tubercle bacilli would be a great advancement for TB diagnostics. Goodridge et al. suggest that sensitivities as great as 93.3% can be achieved when monitoring anti-cardiolipin and anti-phosphatidyl choline IgM antibody decline during the course of drug treatment. The hybrid LFA enables rapid field screening of IgM serum levels against cardiolipin, providing results much faster than Goodridge et al. performed with ELISA. This blood-based diagnostic platform was developed with the endeavor to further study the radical hypothesis that anti-cardiolipin and anti-phosphatidyl choline IgM may enable the real-time evaluation of TB patient response.

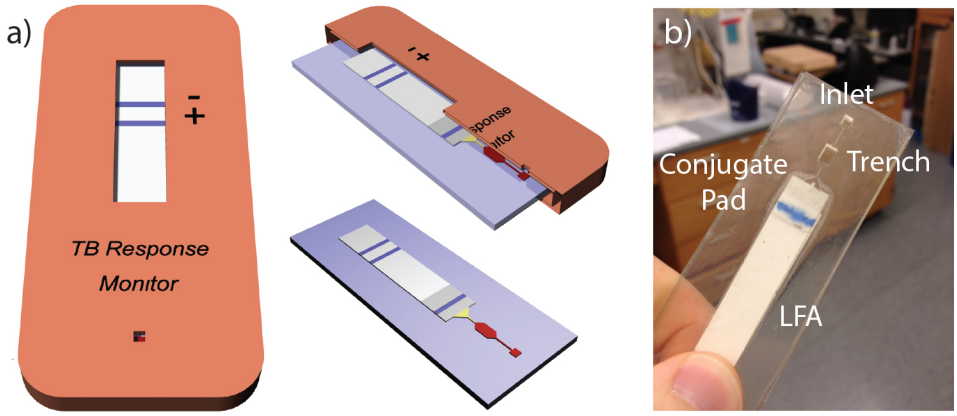

Figure 5.1: a) Schematic depicting the hybrid lateral flow assay (LFA) enclosed within a disposable housing. b) Hybrid LFA for monitoring of TB patient response to drug therapy. The LFA is encased between impermeable pressure sensitive adhesive (PSA) layers and a porous silicone layer. Degas-driven fluid flow enables fluid actuation for cell sedimentation-based plasma extraction before capillary action dominates within the LFA.

The hybrid LFA prototype was developed by sandwiching a traditional LFA within a four-layer microfluidic device. (Fig. 5.2a) The device consists of two outer air impermeable PSA layers (ARseal 90880, Research Adhesives) and a 1.8 mm middle silicone layer (Stockwell Elastomerics, Inc.) that enables degas-driven fluid flow. The PSA layer is made from a silicon-based epoxy, which enables irreversible adhesion to the middle silicone layer. A laser micromachining system (VL200 VersaLaser) was used to ablate geometries into a third 150 μm PSA layer to create microchannels within the device for fluid movement and a recessed opening for even incorporation of the LFA without bulging. (Fig. 5.2b) Holes were laser machined into the silicone layer to form the inlet well and cell sedimentation trench. The device is assembled by hand and hermetically sealed in vacuum packaging to facilitate long-term storage of the antibodies and phospholipids in the LFA. Most commercial LFA systems are enclosed in a plastic housing to protect the assay and ease user operation. The hybrid LFA was designed with the same intention of integrating the assay within a plastic housing to minimalize biologic waste exposure and aid the user with readout of the assay. (Fig. 5.1a)

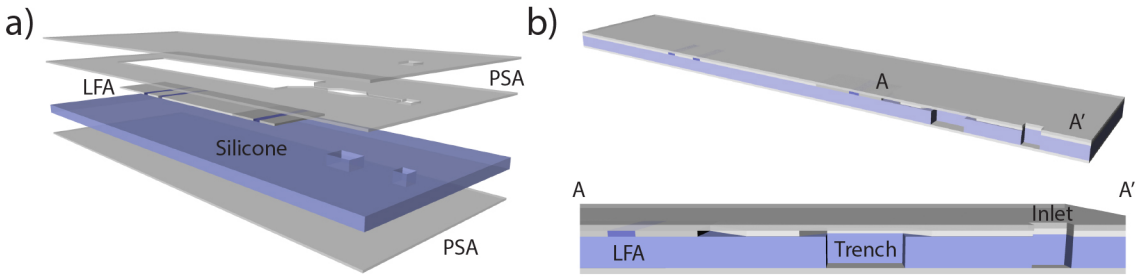

Figure 5.2: a) Incorporation of a traditional LFA within a four layer microfluidic device for upstream sedimentation-based plasma separation. The device is powered by degas-driven fluid flow. b) Cross-sectional views of the device depicting the inlet, trench, microchannel, and LFA.

The LFA incorporated in the hybrid device was fabricated following traditional LFA development protocols.[8,17-20] The nitrocellulose membranes (Hi-Flow Plus HF240, Millipore) and glass fiber conjugate pads (Millipore) were soaked in BSA (Bovine Serum Albumin) blocking buffer before application of the capture cardiolipin antigen and anti-human IgM detection particles. (See Appendix D for protocol) Blocking with BSA improved particle release and overall migration post-adsorption to the nitrocellulose membrane, regardless whether anti-human IgM 300 μm latex bead or 40 nm gold nanoparticles (Diagnostic Consulting Network) were employed. Blue latex beads were easier to visualize than gold nanoparticles (AuNPs) and were used for LFA fabrication. The BSA blocked conjugate pad was manually spotted with 3-5 μL of detection particles at stock concentration. The BSA blocked nitrocellulose membrane was spotted with 0.1 to 50 mg/mL of cardiolipin (Avanti Polar Lipids, Inc.) dissolved in ethanol or chloroform and positive control human IgM (Abcam) at stock concentration using a pipette. A negative control could also be included with a non-complementary antibody. (Fig. 5.3)

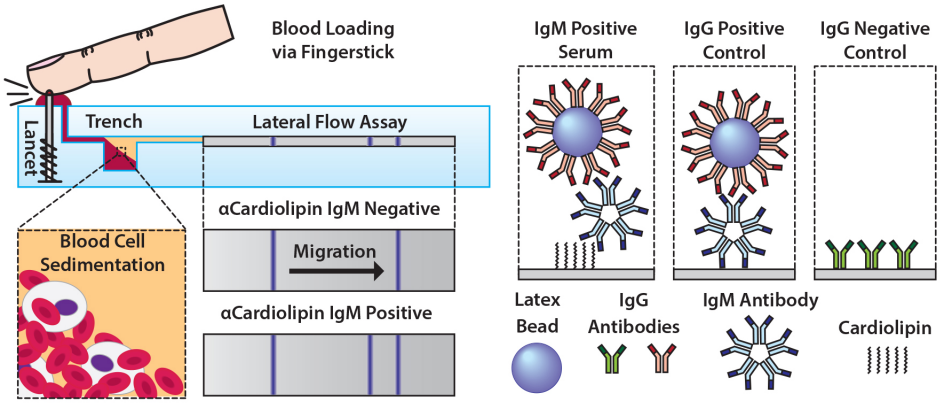

Figure 5.3: Schematic depicting device loading via fingerstick and gravity-enabled cell sedimentation. Visual readout is enabled by latex bead immunoassay of anti-cardiolipin IgM in patient serum and test validation is ensured by the subsequent control lines.

Lipid-based immunoassays are rare and one of the main questions that arose during the development of the hybrid LFA was how to immobilize the cardiolipin antigen. Cardiolipin necessitates dissolution in ethanol, a solvent with which nitrocellulose is incompatible, thus direct application of the lipid resulted in the swelling

and distortion of the nitrocellulose membrane. One solution that was attempted was to spot the cardiolipin on a polyvinylidene fluoride (PVDF) membrane, a material compatible with ethanol that is commonly used in western blots for the transfer and immobilization of proteins. Since PVDF is hydrophobic, thus preventing physioadsorption of the aqueously suspended detection particles, a BSA blocked nitrocellulose membrane was spotted with latex beads and the two membranes were sandwiched together with Scotch tape. (Fig. 5.4) The nitrocellulose membrane overlapped the PVDF membrane by at least 1 cm to ensure the complete wetting of the nitrocellulose and release of the detection particles. (Fig. 5.4d) When the AuNPs/bead side of the LFA is immersed in fluid, capillary action propels the sample between the layers, pulling the detection particles to the cardiolipin antigen region. If anti-cardiolipin IgM antibody were present, the detection particles would theoretically bind and appear on the PVDF. LFAs were developed with different concentrations of detection particles and cardiolipin antigen, and subsequently tested with anti-cardiolipin IgM (SLR Research Corporation) and pooled normal plasma (George King Bio-Medical, Inc.). Post-assay analysis entailed opening the dual membrane strip and visually observing the transfer of detection particles onto the PVDF at the cardiolipin antigen region. (Fig. 5.4e) However, the assay performed poorly as the signal depended upon the cardiolipin concentration and device-to-device variation led to false positives.

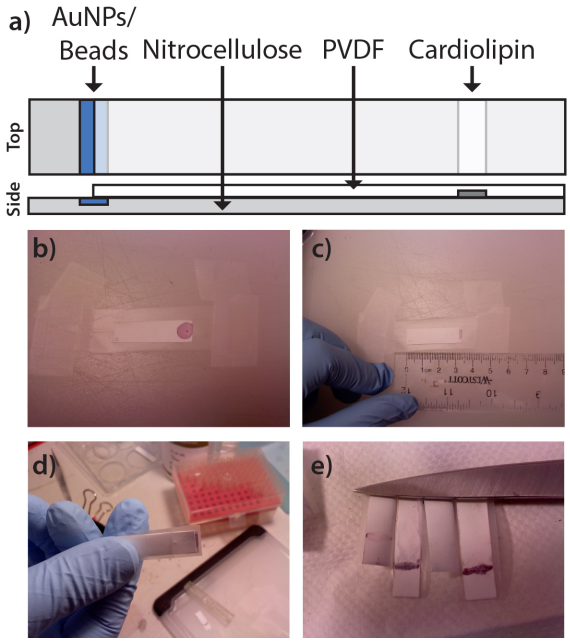

Figure 5.4: Schematic and depiction of the fabrication of a dual membrane nitrocellulose-PVDF LFA. Detection particles were spotted on the BSA blocked nitrocellulose and cardiolipin dissolved in ethanol was spotted on the PVDF. Fluid traverses between the membranes by capillary action.

Upon realizing that nitrocellulose is compatible with chloroform, another solvent for cardiolipin, single strip LFAs were developed without the PVDF membrane. This simpler LFA appeared to yield accurate detection at low cardiolipin concentrations (5 mg/mL), however the faint signal was not a reliable means for visual readout. When the cardiolipin concentration was increased (25 mg/mL), a thin false positive detection band

frequently occurred at the antigen capture region. We hypothesize that the cardiolipin concentration at the necessary concentration for particle capture creates a hydrophilic spot on the LFA. As the detection particles traverse across this region, some are pinned at the front of the hydrophobic capture region leading to a false positive signal. Decreasing the concentration of lipid below 25 mg/mL eliminated the false positive particle band, but yielded signals too faint to be reliably detected.

Ultimately, the hydrophobic nature of cardiolipin was impeding development of the LFA since the lipid could not be bound directly to nitrocellulose, a polar surface. The final attempt to develop an LFA with a lipid-based capture region involved the chemical modification of cardiolipin and conjugation to BSA to negate the hydrophobic effects of the lipid.[21] The double bonds in the unsaturated fatty acid side chains of cardiolipin were oxidized with sodium m-periodate ($NaIO_4$) and potassium permanganate ($KMnO_4$), as described by Castro et al.[21] (Fig. 5.5a) The oxidized cardiolipin was verified by thin layer chromatography (TLC) using molybdenum blue, which reacts with the phosphate head group in cardiolipin. The lack of a reaction, evident by the white smear in Fig. 5.5b, indicates that small hexanoic and malonic acids were cleaved from the lipid. The carboxyl groups in the oxidized cardiolipin were converted to amine-reactive NHS esters using a combination of EDC (1-ethyl-3-(3-dimethylaminopropyl) carbodiimide) and NHS (N-hydroxysuccinimide) chemistry, facilitating protein conjugation. (Fig. 5.5c) The conjugated BSA was then dialyzed in 10mM PBS buffer. Unfortunately, results using the prepared BSA-cardiolipin conjugation are pending as excessive crosslinking occurs upon the addition of BSA. A white, paper-like precipitate forms with the addition of BSA and synthesis of the conjugated protein should be performed with greater concentrations of BSA.

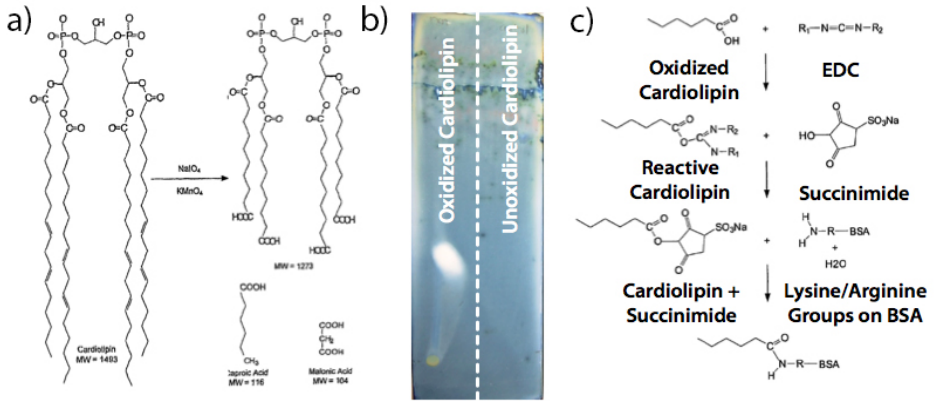

Figure 5.5: To eliminate the false positive signal that is observed when cardiolipin is spotted directly onto the LFA, cardiolipin was oxidized and conjugated to BSA (Bovine Serum Albumin). This chemistry should negate the hydrophobic effects of the cardiolipin detection band, preventing aggregation of the detection particles that cause the false positive readout.

5.4 Analysis of Anti-phospholipid Antibodies in Patient Samples

In addition to LFA development, anti-phospholipid IgM levels in patient samples were simultaneously evaluated to determine the limit of detection necessary for the assay

to achieve. ELISA (Abnova) was performed on plasma samples to determine the concentration of anti-cardiolipin antibodies present in the blood serum of patients with TB and Lupus. In comparison with normal blood plasma, results indicate a 5-10x and 30-50x fold increase for TB and Lupus patients, respectively. Therefore anti-cardiolipin IgM (SLR Research Corporation) from Lupus patients was used for preliminary LFA device testing. In addition to TB and Lupus, syphilis is another disease that is directly applicable to the development of the hybrid LFA and the screening of elevated anti-phopholipid antibody levels.[14] Preliminary ELISA results performed in Brazil also suggest that anti-cardiolipin IgM levels correlate with the number of cavities patients have when suffering from cavitary pulmonary tuberculosis. (Fig. D1) In addition to monitoring patient drug response, this assay may be able to effectively diagnose disease severity of in individual of multi-cavitary tuberculosis in regions without access to x-ray imaging equipment.

Table 5.1: ELISA Analysis of Anti-cardiolipin Antibodies Present in Blood Serum

Diagnosis	IgM (μg/mL)	TB Patient ID	IgM (μg/mL)	Lupus Patient ID	IgM (μg/mL)
Negative	**<1500**	302	286	7311	3181
Borderline Positive	**1500-2000**	007	363	7316	3362
		322	656	7320	1318
Low/Medium Positive	**2000-8000**	938	64	7321	2118
		304	63	7322	2102
High Positive	**>8000**	309	231	7323	3657
		Average	**277**	7324	3570
Pooled Normal Plasma	**66**			7325	3174
				Average	**2810**

5.5 CONCLUSION

The development of a hybrid LFA device coupling autonomous plasma separation from whole blood with the traditional particle-based immunodetection of an LFA is described. Degas-driven fluid flow powers initial upstream loading of blood into the cell-sedimentation trench and a microchannel directs extracted plasma to an LFA where capillary action enables fluid flow. The LFA was designed to monitor anti-phospholipid IgM levels, a biomarker potentially capable of monitoring patient response during the course of TB drug regiments. In addition, elevated levels of these antibodies are present in Lupus and syphilis, expanding the array of applicable diseases. Several methods of lipid immobilization to the LFA are described and assay development is ongoing. This device could potentially revolutionize the TB drug management in resource-limited settings by providing real-time patient monitoring.

5.6 ACKNOWLEDGEMENTS

This work was performed in collaboration with Debkishore Mitra, Jessie Tung, Robert Snyder, Seung-min Park, Amador Goodridge, and Prof. Lee Riley of the UC Berkeley School of Public Health. Debkishore Mitra was an equal partner throughout the project and invaluable at brainstorming solutions to the numerous problems that were incurred through LFA development. Financial support was provided by the Henry

Wheeler Center for Emerging and Neglected Diseases (SMP), the Cal NERDS Summer Undergraduate Research Program (JT), and the National Science Foundation Graduate Research Fellowship Program (JRW).

5.7 REFERENCES

1. Lopez, A. D., Mathers, C. D., Ezzati, M., Jamison, D. T. & Murray, C. J. L. Global Burden of Disease and Risk Factors. *Oxford University Press, Inc.* (2006).
2. Udwadia, Z. F., Amale, R. A., Ajbani, K. K. & Rodrigues, C. Totally Drug-Resistant Tuberculosis in India. *Clinical Infectious Diseases* **54**, 579–581 (2012).
3. Gandhi, N. R. *et al.* Extensively drug-resistant tuberculosis as a cause of death in patients co-infected with tuberculosis and HIV in a rural area of South Africa. *Lancet* **368**, 1575–1580 (2006).
4. Urdea, M. *et al.* Requirements for high impact diagnostics in the developing world. *Nature* **444**, 73–79 (2006).
5. Keeler, E. *et al.* Reducing the global burden of tuberculosis: the contribution of improved diagnostics. *Nature* **444**, 49–57 (2006).
6. Forum, G. H. D. The right tools can save lives. *Nature* **444**, 681–681 (2006).
7. Dye, C. & Williams, B. G. The Population Dynamics and Control of Tuberculosis. *Science* **328**, 856–861 (2010).
8. O'Farrell, B. *Lateral Flow Immunoassay*. 1–33 (Humana Press: Totowa, NJ, 2008).doi:10.1007/978-1-59745-240-3_1
9. Songjaroen, T., Dungchai, W., Chailapakul, O., Henry, C. S. & Laiwattanapaisal, W. Blood separation on microfluidic paper-based analytical devices. *Lab Chip* **12**, 3392–3398 (2012).
10. Govindarajan, A. V., Ramachandran, S., Vigil, G. D., Yager, P. & Böhringer, K. F. A low cost point-of-care viscous sample preparation device for molecular diagnosis in the developing world; an example of microfluidic origami. *Lab Chip* (2012).doi:10.1039/c1lc20622b
11. Nabatiyan, A., Parpia, Z. A., Elghanian, R. & Kelso, D. M. Membrane-based plasma collection device for point-of-care diagnosis of HIV. *J Virol Methods* **173**, 37–42 (2011).
12. Chin, C. D., Linder, V. & Sia, S. K. Commercialization of microfluidic point-of-care diagnostic devices. *Lab Chip* **12**, 2118–2134 (2012).
13. Choi, D. H. *et al.* A dual gold nanoparticle conjugate-based lateral flow assay (LFA) method for the analysis of troponin I. *Biosensors and Bioelectronics* **25**, 1999–2002 (2010).
14. Castro, A. R. *et al.* Novel point-of-care test for simultaneous detection of nontreponemal and treponemal antibodies in patients with syphilis. *J Clin Microbiol* **48**, 4615–4619 (2010).
15. Dimov, I. K. *et al.* Stand-alone self-powered integrated microfluidic blood analysis system (SIMBAS). *Lab Chip* **11**, 845–850 (2011).
16. Goodridge, A. *et al.* Anti-phospholipid antibody levels as biomarker for monitoring tuberculosis treatment response. *Tuberculosis* **92**, 243–247 (2012).
17. Mansfield, M. A. Chapter 4. *Drugs of abuse* (2005).
18. Christopher, P., Robinson, N. & Shaw, M. K. Chapter 5. *Drugs of abuse* (2005).

19. Carlberg, D. Chapter 6. *Drugs of abuse* (2005).
20. Wang, X. *et al.* Development of an immunochromatographic lateral-flow test strip for rapid detection of sulfonamides in eggs and chicken muscles. *J Agric Food Chem* **55**, 2072–2078 (2007).
21. Castro, A. R. & Wang, H. Modified Cardiolipin And Uses Therefor. (2011).

CHAPTER 6

A CORE-SATELLITE NANOASSEMBLED SUBSTRATE FOR COLORIMETRIC BIOMOLECULAR DETECTION

6.1 ABSTRACT

While gold nanoparticles are commonly used in lateral flow assays for visual readout, a development within the past 15 years has been colloidal-based nanoparticle assemblies for visual detection. These liquid-based systems have enabled the demonstration of nucleic acid and aptamer-based recognition yielding greater detection sensitivities. However, such detection schemes are not implementable in microfluidic diagnostic devices. In this chapter, the disassembly of a core-satellite nanostructured substrate is presented as a colorimetric biosensor observable under dark field illumination and can be executed in microfluidic devices for visual readout. The fabrication method described herein utilizes thiol-mediated adsorption and streptavidin-biotin binding to self-assemble core-satellite nanostructures with a sacrificial linking peptide. Biosensing functionality is demonstrated with the protease trypsin and the optical properties of the nanoassemblies are characterized. A figure of merit is presented to determine the optimal core and satellite size for visual detection. Nanoassemblies with 50 nm cores and 30 nm or 50 nm satellites are superior as these structures achieve an orange to green color shift greater than 70 nm that is easily discernible by naked eye. This colorimetric substrate may prove to be a favorable alternative to liquid-based colloidal sensors and a useful visual readout mechanism for microfluidic diagnostic assays.

6.2 INTRODUCTION

The simultaneous realization of self-assembled colloidal gold nanocrystals by Mirkin and Alivisatos established a platform technology for 'bottom up' fabrication that utilized fundamental principles from biology. This technology has shown the greatest promise for diagnostic biomolecular detection. Although lateral flow assays have used gold nanoparticle-based detection for decades, the new paradigm of colloidal-based nanosensors has greatly enhanced sensitivity and facilitated other mechanisms of biorecognition such as nucleic acid and aptamer-based sensing. The advent of this discovery has yielded a multitude of geometric nanoassembly variations such as lattice networks,[1,2] dimer and trimer configurations,[3-5] and core-satellite constructs.[5-11] Gold nanoparticle assemblies have localized surface plasmon resonances in the visible spectrum that are easily observable by eye. (Fig. 6.1a) Assemblies with greater numbers of nanoparticles cause a nearly linear redshift in the scattering spectrum. (Fig. 6.1b and 6.1c) These noble metal nanoassemblies have enabled optical investigations of plasmon resonance coupling[10,11] and the colorimetric detection of biological and chemical analytes such as single nucleotide polymorphisms (SNPs),[12] cocaine,[13] adenosine,[13] lead,[14]

caspase,[15] and rabbit IgG.[16] Such technologies may bolster the groundwork for a new generation of point-of-care diagnostic devices (POCDx) capable of identifying diverse analyte species, an improvement upon the commercially available immunoassay-based lateral flow test.[17]

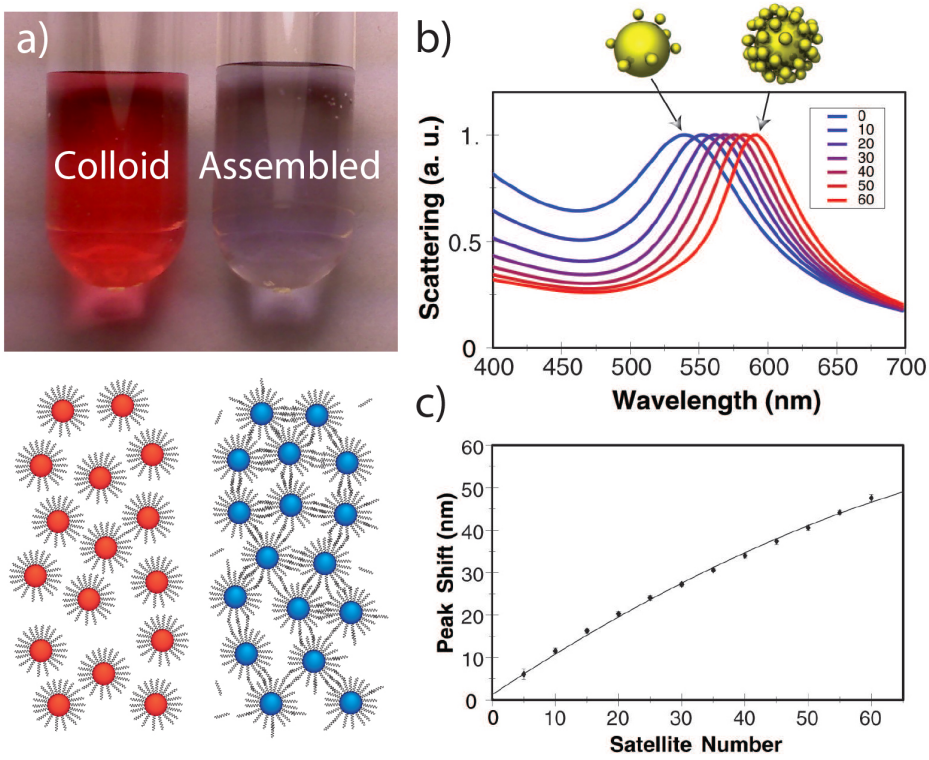

Figure 6.1: a) The local surface plasmon of colloidal-based nanosensors is in the visible spectrum, allowing visual detection of assembly. The picture depicts complementary nucleic acid detection and nanoassembly. b) The scattering spectrum of nanoassemblies redshifts as more particles aggregate and local plasmonic coupling between particles occurs. c) The redshift is nearly linear. Methods for the simulation are discussed in section 6.7 and the diameters of the nanoparticles are: d_{core}=100 nm and $d_{satellite}$=20 nm.

We propose an advancement upon the current suspension-based modality of colloidal biomolecular sensors that is better suited for on-chip diagnostic system integration while preserving the capability for diverse species detection. We present the fabrication of nanoassembles constructed on a two-dimensional glass substrate, demonstrate the colorimetric functionality of biomolecular sensing *via* disassembly, and systematically analyze the optical detection properties of the substrate. Nanoconstructs with 50 nm cores and 30 nm or 50 nm satellites maximized the signal-to-noise ratio during biosensing and enabled visible colorimetric shifts from orange (>630 nm) to green (~560 nm) *via* the observation of scattered light with dark field (DF) illumination.

The construction of colloidal gold biosensors using DNA, peptide, or aptamer linkers has enabled the detection of an assortment of species outside the typical antigen/antibody binding interactions observed in traditional immunoassays.[12-17] This

method is advantageous as plasmonic nanoparticles are ~500,000 times more luminous than a fluorophore, have an unlimited photon budget, and do not bleach, blink, or require expensive spectroscopic equipment.[18] However, the technology to date has relied upon nanoconstructs suspended in solution. This assembly paradigm has five deficiencies that may be overcome by the use of disassembling nanostructures immobilized on a substrate:

1) The sample analyte is diluted by at least three orders of magnitude when added to the suspension of nanostructures, diminishing detection limits.
2) Impurities in the analyte, such as salts and pH fluctuations, might cause flocculation and subsequently, a false positive readout.
3) The storage life is limited because suspended nanoparticles tend to aggregate and settle with time.
4) Liquid-based assays are prone to containment issues such as spillage and require liquid handling units.
5) The most significant flaw is that liquid-based sensors rely upon changes in optical absorbance, a serious impracticality for microfluidics.

Since the Beer-Lambert Law ($A=\varepsilon lc$, where A is the absorbance, ε is the extinction coefficient of the suspension, l is the path length, and c is the nanoparticle concentration) states that absorbance has a linear dependence on path length, colloidal liquid-based sensors are not feasible in microfluidic diagnostic systems. The colorimetric substrate presented here bypasses these shortcomings. Previous reports of disassembling colorimetric nanomaterials on a substrate have included the resuspension of nanoparticles released from nanolattices dried on hydrophobic paper or constructed on a fluid lipid bilayer membrane.[19,20] However, unlike previous biosensors, we present the first self-assembled substrate that yields a structural color change directly at the site of disassembly when imaged in DF. The small optical path length of the biosensing substrate (~nm) is better suited for the length scales of on-chip diagnostic systems (~μm) in comparison to suspended nanoassembled networks that require longer path lengths (~cm) for colorimetric changes to be observable. The utility of this localized disassembly mechanism may enable functionality for spatiotemporal monitoring of cellular secretions and POC capability using innovative handheld DF viewing techniques.

Protease diagnostics are greatly underutilized in clinical settings and detectable levels of proteases present in peripheral fluids taken *ex vivo* have been shown to act as diagnostic markers that are presymptomatically indicative of disease.[21-24] For example, specific tissue factors of the coagulation cascade could be monitored in people treated with anticoagulant therapies or diagnosed with blood disorders. This would permit assessment of specific proteolytic tissue factors instead of monitoring blood coagulation as a whole. A substrate able to detect protease activity was designed as a proof-of-concept to demonstrate the structurally induced spectral scattering shift of the biosensor. This article presents the use of scattered light from coupled gold nanoparticle assemblies and their subsequent disassembly *via* proteolysis as a colorimetric assay to detect protease activity. Cleavage of the nanoassemblies disengages the plasmon coupling between nanoparticles and shifts the observed DF scattered light from orange to green (Figure 6.2a). This model system is not only limited to protease activity monitoring, but

is applicable to the detection of numerous biomolecules. By altering the core-satellite tether, detection platforms for other biomolecular species can be created.

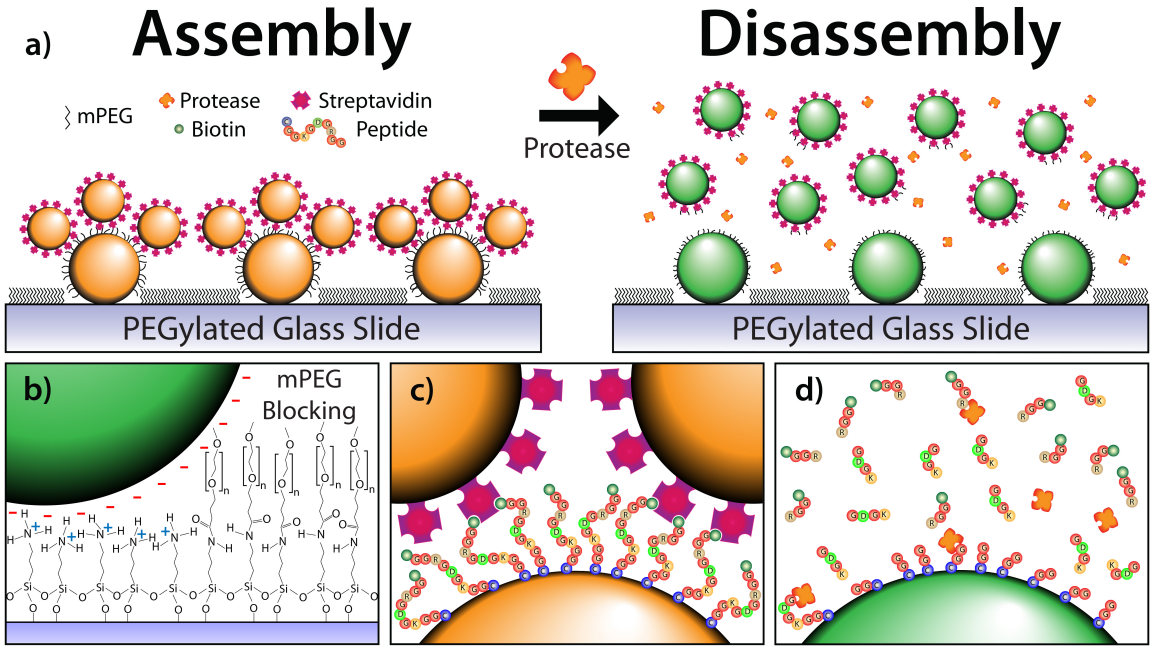

Figure 6.2: a) Core-satellite Au nanoassemblies before and after proteolytic cleavage. b) Immobilization of the negatively charged AuNP cores is enabled by Coulombic electrostatic attraction to an APTES monolayer on glass. The glass slide is subsequently passivated with an mPEG chain to block nonspecific satellite adsorption. c) Satellite attachment is enabled by a directional cysteine/biotin-streptavidin peptide tether. d) The addition of trypsin cleaves the peptide, releasing the satellites into solution and enabling colorimetric detection of the protease.

6.3 Substrate Assembly

Gold nanoparticles (AuNPs) were first deposited onto APTES (3-aminopropyltriethoxysilane) functionalized glass microscope slides. The sodium citrate reduction (Turkevich) method[25] produces negatively charged AuNPs and the AuNPs, which served as the core of the nanoconstruct, were electrostatically immobilized onto the positively charged surface of the APTES glass slide through Coulombic attraction (Figure 1b, left). Next, a biotinylated ten amino acid long peptide substrate, cleavable by the serine protease trypsin, was incubated on the substrate. The C-terminus of the peptide is a cysteine residue, enabling the thiol-mediated adsorption of the peptide onto the surface of the core nanoparticle. The peptide sequence is biotin-GGRGDGKGGC-OH. Streptavidin conjugated satellite nanoparticles bind to the biotinylated N-terminus of the peptide for controlled, directional self-assembly (Figure 6.2c). The incubation of methoxy polyethylene glycol succinimidyl valerate (mPEG-SVA, M_W = 2 kDa) on the substrate before satellite deposition blocks the microscope slide such that the satellites only attach to the core nanoparticles. This essential step prevents the satellites from nonspecifically adsorbing onto the substrate and facilitates a reversible color shift. The APTES-functionalized slide enables passivation as the mPEG-SVA reacts with the exposed primary amine, releasing 1-Hydroxy-2,5-pyrrolidinedione and immobilizing the

PEG chain onto the slide (Figure 6.2b, right). It should be noted that the linking peptide chain could be replaced by a variety of other biomolecules such as an oligonucleotide or aptazyme for diverse analyte identification. All substrates were stored in deionized (DI) water to prevent capillary remodeling caused by evaporation. The substrates remained functional for more than 28 days when stored in DI water at 4°C. The complete protocol for nanoassembly fabrication is described in Appendix E.

6.4 SCATTERING PROPERTIES OF GOLD NANOPARTICLES

Pairs of slides were created for each geometrical combination of core (30, 50, 80, and 100 nm) and satellite size (10, 30, and 50 nm) and analyzed under DF. A spectrophotometer measured the far-field scattering spectra from the substrate and data taken from five random positions on each substrate were averaged to determine peak position and full width at half maximum (FWHM). AuNPs cores were deposited at high densities, ~33.1 cores μm^{-2} for 50 nm AuNP cores, enabling easy visualization of the scattered color yet substrates were not overly dense, which would cause unfavorable plasmonic coupling between core particles. Four variations of core diameter were investigated. 30 nm and 50 nm cores scattered green in comparison to 80 nm and 100 nm cores, which appeared chartreuse (Table 6.1 and Fig. E1). Additionally, the two larger core sizes have broader peakwidths (FWHM). Radiation damping has been shown to be responsible for the redshift and bandwidth broadening observed in both the near- and far-field scattering as nanoparticles increase in size.[26] Core sizes with green scattering, which is the most sensitive color to the human eye, are optimal as their plasmon peak will be redshifted upon satellite attachment and plasmon coupling. The redshift for assemblies with a large core size (>50 nm) cannot be visually discerned as the far-field scattering spectra shifts into the near IR, however such shifts are detectable with spectroscopy. Another important property for core size is the scattering cross-section (σ_s). When a particle radius (r) is much smaller than the wavelength of light ($r \ll \lambda$), Rayleigh theory states:

$$\sigma_s = \frac{128}{3}\frac{\pi^5 n_b^4 r^6}{\lambda^4}\left|\frac{n_{rel}^2 - 1}{n_{rel}^2 + 2}\right| \tag{6.1}$$

when $n_{rel}=n_s/n_b$. Thus $\sigma_s \propto r^6/\lambda^4$ and core sizes of 30 nm and smaller have a small scattering cross-section, resulting in dimly scattered green light which is difficult to visualize in DF. (Table 6.1) The optimal core size, as determined by its spectral peak position and scattering cross-section, is 50 nm.

Table 6.1: Scattering Properties of Various Sized Core AuNPs

Core AuNP Size (nm)	Peak Position (nm) [a]	FWHM (nm) [a]	Scattering Cross-section, σ_s (nm^2) [b]	Scattering Efficiency, Q_s [b]
30	561.0	97.5	0.94	0.0013
50	556.0	84.6	18.31	0.0093
80	568.3	115.3	249.90	0.0497
100	569.3	110.1	806.05	0.1026

[a] Experimental measurements; [b] Calculated using Mie theory

The effects of Rayleigh scattering can be observed in the color of colloidal suspensions ranging 50 to 150 nm in diameter (Fig. E2a). Smaller gold nanoparticles (50 nm) have larger scattering cross-sections at smaller wavelengths, such as blue light. Thus, these particles appear redder in suspension. As the radius of the gold nanoparticle increases, both short and longer wavelengths of light are scattered and the particles appear translucent. The calculated scattering cross-sections (σ_s) and scattering efficiencies (Q_s) in Table 6.1 were determined using Mie theory.[27] Mie theory is an exact solution of scattering and can determine the electromagnetic radiation scattered by larger spheres, whereas Rayleigh scattering is only valid when the particle radius is much smaller than the wavelength of light ($r \leq 0.1\lambda$). The scattering efficiency is a proportionality parameter that relates the effective scattering cross-section to the actual geometric cross-section $\sigma_s = \pi r^2 Q_s$. The optical properties of gold were taken from literature for the calculations in Table 6.1.[28-30]

6.5 Results and Discussion

The serine protease trypsin, known to cleave the carboxyl end of lysine and arginine, was used to initiate substrate disassembly (Figure 6.2d). Trypsin (100 μM) was spotted directly onto the substrate at room temperature (25°C) and produced a complete color change in less than 40 minutes as seen in the images captured by a true-color charge-coupled device (CCD) camera (Figure 6.3). Figures 6.3a, 6.3b, and 6.3c are time-lapse images of a substrate at 0 min, 30 min, and 60 min after trypsin exposure. The white spots observable in Figure 6.3c are believed to be scattering from mPEG-SVA aggregates that accumulated during surface passivation. A representative DF spectrum depicts a colorimetric shift greater than 70 nm for a substrate with 50 nm cores and 50 nm satellites (Figure 6.3d). Modified Gaussian curves have been fit to the data. An SEM image of a 100 nm core with 10 nm satellites is shown in Figure 6.3e. Core sizes larger than 100 nm scatter light greater than 600 nm and satellite disassembly is visually indiscernible. Thus, larger sized core particles were eliminated from the study. A nanoassembled substrate with 50 nm cores and 50 nm satellites, before and after trypsin-mediated disassembly, is shown under bright field illumination in Figure 6.3f. The short path length of the monolayer of core-satellites does not scatter enough of the incident light for a colorimetric change to be noticeably observable by eye. A technique similar to resonance-enhanced adsorption may be able to amplify this faint color shift under bright field illumination and facilitate detection without the constraint of DF illumination.[31] Polydimethylsiloxane (PDMS) droplet immobilizers, visible in Figure 6.3f, were used to contain the droplet and prevent capillary-induced remodeling of the nanostructures due to evaporation. All of the images presented in Figure 6.3 are unaltered.

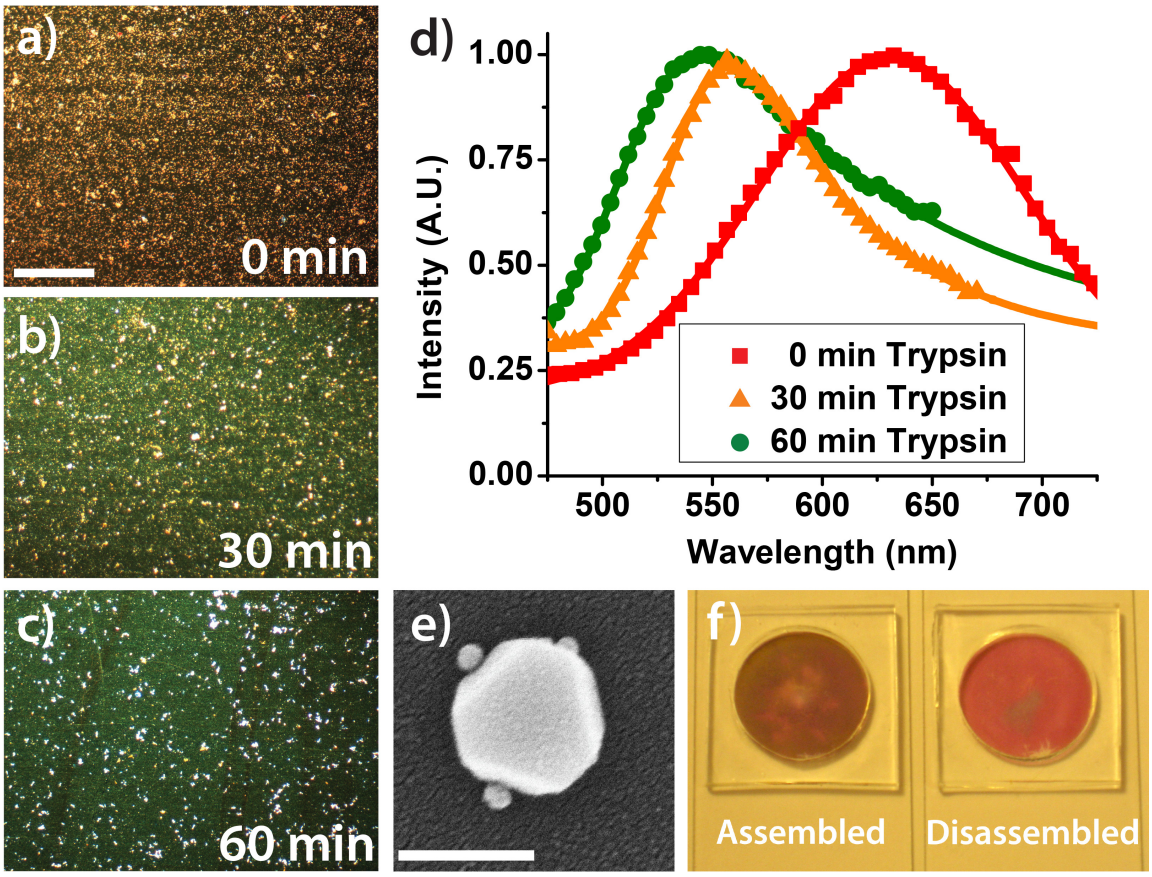

Figure 6.3: Dark field microscopy images representative of the observable colorimetric shift upon disassembly by proteolytic cleavage with 100 µM trypsin at a) 0 minutes, b) 30 minutes, and c) 60 minutes. The substrate is composed of 50 nm core AuNPs and 50 nm satellite AuNPs. (scale bar: 100 µm) d) The corresponding normalized spectra taken simultaneously with the images. e) SEM image of an individual core-satellite nanoassembly with a 100 nm core and 10 nm satellites. (scale bar: 100 nm) f) A 50 nm core and 50 nm satellite nanoassembled substrate before and after trypsin cleavage *via* bright field illumination. The short path length of the core-satellite nanoassembled substrate does not scatter enough of the incident light for a colorimetric change to be noticeably observable by eye.

A large-scale study was performed for an array of nanostructures to characterize assembly and disassembly (Figure 6.4). Core sizes ranged from 30 nm to 100 nm and satellite sizes ranged from 10 nm to 50 nm. Satellites larger than 50 nm are difficult to conjugate with streptavidin as the surface-to-volume ratio is large and the colloid becomes unstable during physio-adsorption of the streptavidin onto the AuNP surface. Maintaining the electrostatic repulsion between the negatively charged nanoparticles is essential and prevents the suspension from crashing out of solution. Substrates were prepared in duplicate and optical measurements were acquired at random locations in quintuplicate for each slide (n=10). The acquisitions were collected over a large field of view such that substrate inconsistencies and variations were averaged over the acquired spectrum. Disassembly was achieved by exposing the substrates to trypsin for 60 minutes at room temperature. The ten spectral measurements were averaged and are graphed in Figure 6.4. The peaks observed at ~670 nm and ~740 nm in Figure 6.4 are

attributed to source normalization artifacts due to a poor signal-to-noise ratio at the spectral extremities of our spectrophotometer. See Figure E3 for the emitted spectrum from the Xenon light source used in this study. A MATLAB script individually calculated the peak shift and FWHM for each spectral measurement and the values were averaged to obtain peak shift and FWHM statistics. The script is located in Appendix E.

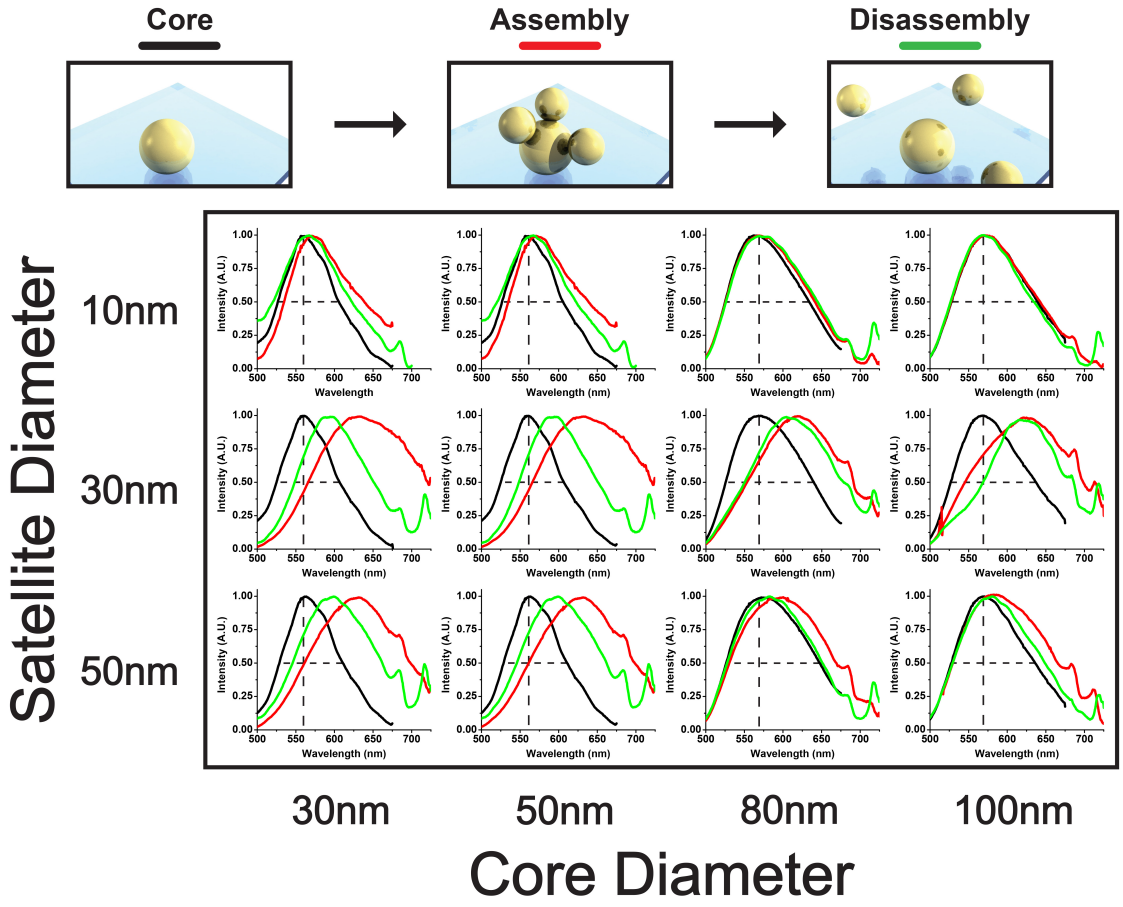

Figure 6.4: Dark field microscopy images representative of the observable colorimetric shift upon disassembly by proteolytic cleavage with 100 µM trypsin at a) 0 minutes, b) 30 minutes, and c) 60 minutes. The substrate is composed of 50 nm core AuNPs and 50 nm satellite AuNPs. (scale bar: 100 µm) d) The corresponding normalized spectra taken simultaneously with the images. e) SEM image of an individual core-satellite nanoassembly with a 100 nm core and 10 nm satellites. (scale bar: 100 nm) f) A 50 nm core and 50 nm satellite nanoassembled substrate before and after trypsin cleavage *via* bright field illumination. The short path length of the core-satellite nanoassembled substrate does not scatter enough of the incident light for a colorimetric change to be noticeably observable by eye.

6.6 Determining the Optimal Core-Satellite Geometry

Two important optical characteristics for visual detection are the peak shift and change in FWHM upon assembly and disassembly. Peak shift upon assembly is defined as: $\Delta\lambda_{peak} = \lambda_{peak,core+sat.} - \lambda_{peak,core}$ and is depicted on the x-axis of Figure 6.5a. The maximum attained assembly redshifts were approximately ~70 nm for all combinations

of 50 nm and 30 nm AuNPs. 30 nm satellites consistently produced the largest peak shift of all the satellite sizes. This behavior seems contrary to intuition as 50 nm satellites cause a larger structural change than 30 nm satellites. Limited streptavidin conjugation onto the larger 50 nm AuNPs may have resulted in fewer satellites capable of binding to the core particles. Next, the peak shift upon disassembly was analyzed and is depicted on the x-axis of Figure 6.5b. Combinations of 30 nm and 50 nm AuNPs provided the largest blue shift, with 30 nm core and 50 nm satellite assemblies causing a maximum shift of 48.3 nm. The investigation reveals that the assembly redshift is not completely reversible, which may be caused by nonspecific aggregation of the satellites to the substrate and/or irreversible core-satellite attachment. Overall, core-satellite combinations of 30 nm and 50 nm result in the largest spectral peak shifts. The findings of this analysis correlate well with previous theoretical simulations of core-satellite plasmon band redshifting due to interparticle dipole coupling and radiation damping.[10,32]

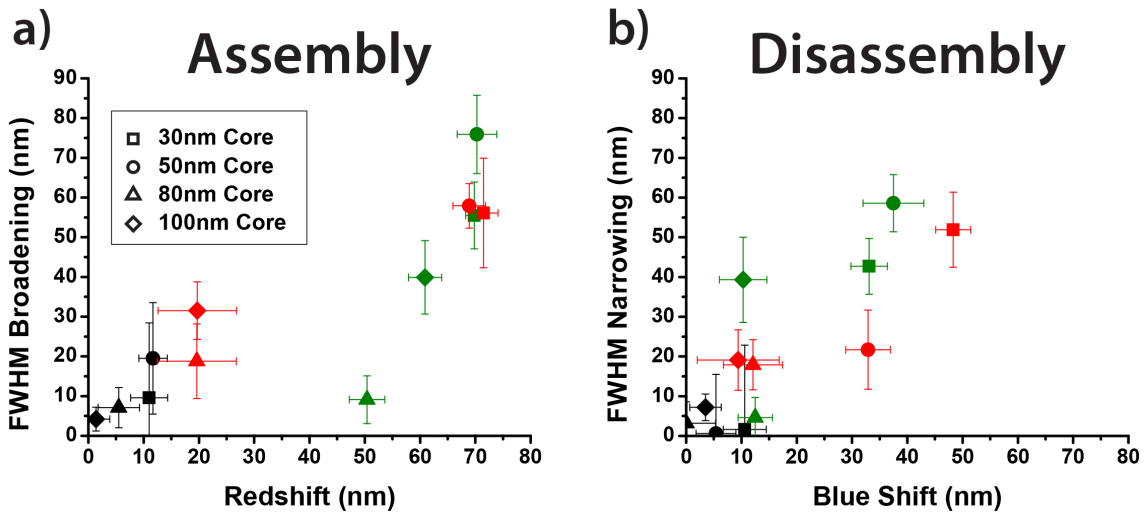

Figure 6.5: Correlation between peak shift and FWHM broadening/narrowing upon a) assembly and b) disassembly. Data points are extracted from Figure 6.4 with the shape corresponding to the core size and the color corresponding to the satellite size. 10 nm, 30 nm, and 50 nm satellites are represented by black, green, and red, respectively.

The second optical characteristic analyzed was the FWHM assembly broadening and disassembly narrowing properties of the nanoassemblies. Analysis of the FWHM is necessary to maximize the signal-to-noise ratio during biosensing as large FWHM increases may cause disassembly blue shifts to be indiscernible. The change in the bandwidth upon assembly, defined as $\Delta FWHM = FWHM_{core+sate.} - FWHM_{core}$, was a maximum, 75.9 nm, for the 50 nm core and 30 nm satellite assembly (Figure 6.5a). Other combinations of 30 nm and 50 nm AuNP produced ~56 nm in bandwidth broadening. During disassembly, 50 nm cores with 30 nm satellites obtained the maximum bandwidth narrowing (Figure 6.5b). Minimizing the bandwidth upon assembly and disassembly is essential such that only one color, a single peak, can be easily resolved by human eye for both cases. Thus optimal core-satellite combinations would lie in the lower right side of Figures 6.5a and 6.5b. However, our data reveals that shifts in peak position appear to be positively correlated to changes in bandwidth. These

results coincide with recent findings that larger satellite sizes broaden the plasmon band when assembled onto core AuNPs.[32] This characteristic is mainly due to retardation effects as the nanoassembly size becomes significant in comparison to the wavelength of light. Radiation damping has been shown to be a large factor in the redshifts observed in the far-field scattering as nanoparticles increase in size.[26] Ultimately, larger satellite sizes should lead to greater changes in FWHM upon assembly and disassembly. Similar to the nanoassemblies' characteristics with regard to peak shift, 30 nm satellites consistently produced the greatest fluctuations in bandwidth for both assembly and disassembly. Qualitative heat maps for both the peak shift and change in FWHM upon assembly and disassembly are shown in Figures E4 and E5, in addition to the sample standard deviations for the peak shift and FWHM measurements (Tables E1 and E2).

In order to quantify the overall biosensing capability of each nanoassembly variation, we have proposed the use of a figure of merit (FOM) for detecting plasmon peak shifts:[32]

$$\mathrm{FOM} = \frac{\Delta\lambda_{\mathrm{Peak}}}{\langle \mathrm{FWHM} \rangle} \tag{6.2}$$

where $\langle \mathrm{FWHM} \rangle$ is the average of the two FWHM values. The FOM takes into account both the peak shift and plasmon bandwidth, quantifying the nanoassemblies' ability to provide a resolved and observable colorimetric change. The experimentally obtained FOM values are shown in Table 6.2 for the nanoassembly variations we have studied. The substrate with 30 nm cores and 50 nm satellites has the highest FOM value, 0.37. However, the small scattering cross-section of a 30 nm core AuNP made this substrate very difficult to observe by naked eye. The second and third nanoassemblies with the next highest FOM values, 50 nm cores with 30 nm and 50 nm satellite sizes, yielded spectacular color shifts for our experimental setup (Fig. 6.3). These two combinations of nanoassembly are optimal.

Table 6.2: Figure of Merit for Various Core-Satellite Assemblies

		Core Size			
		30 nm	**50 nm**	**80 nm**	**100 nm**
Satellite Size	**10 nm**	0.10	0.05	0.01	0.07
	30 nm	0.26	**0.28**	0.10	0.08
	50 nm	0.37	**0.25**	0.09	0.03

6.7 COMPARISON WITH MIE THEORY SIMULATIONS

In an effort to optimize the core-satellite assembly and provide theoretical validation of the experimental results, colloidal gold nanoassemblies were simulated with the Generalized Multiparticle Mie solution.[33] This method provides an exact solution of electromagnetic scattering from multiple spheres at a specified distance and arrangement. Additionally, it allows us to make generalizations about nanoparticle assembly that can be applied to the nanoassembled substrate. As it was observed in Fig. 6.1b and 6.1c, more satellite nanoparticles cause a greater redshift in the scattering spectrum from localized plasmonic coupling between the core and satellites. However, controlling the

number of conjugated satellites, much less adding 60 satellites to a single core, is not possible. The most satellites reported on a 50 nm core is ~20 satellites with diameters of $d_{satellite}$=13 nm.[10] From Fig. 6.1b, this would lead to a peak shift of approximately 20 to 25 nm. This is about twice the redshift we observed with cores of d_{core}=50 nm and satellites of $d_{satellite}$=10 nm. (Fig. 6.5a) The difference is likely attributed to less surface area available on the core nanoparticle for satellite attachment, steric hindrance of the substrate, and assumptions in the simulations such as homogeneous peptide coverage.

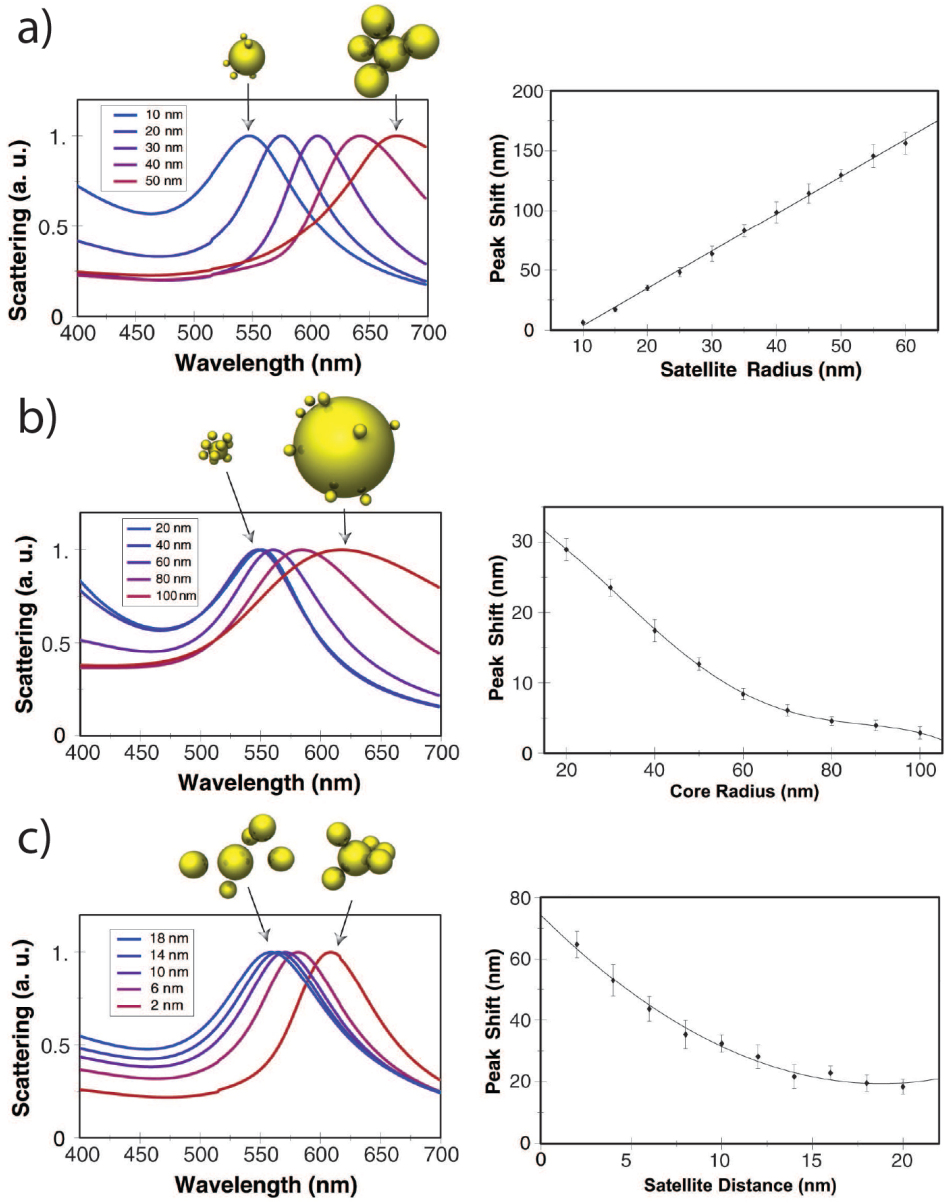

Figure 6.6: Effects of varying the a) satellite size, b) core size, and c) inter-particle distance in colloidal-based core-satellite systems. The generalizations obtained through simulations with the Generalized Multiparticle Mie theory regarding nanoparticle assembly correlate with those learned from the investigation with the nanoassembled substrate.

Two other possible strategies for maximizing the redshift upon attachment are to increase the satellite size (Fig. 6.6a) or to increase the core size. (Fig. 6.6b) As the size of the satellite nanoparticle increases, fewer satellites ($n_{satellite}$=5) are needed to yield significant redshifts in the plasmon resonance. Additionally, radiation damping causes the FWHM to broaden, mainly due to retardation effects as the nanoassembly becomes comparable to the wavelength of light.[26] For $d_{satellite}$=50 nm, the simulation predicts that a redshift of approximately 50 nm is expected to occur. We observed redshifts of 20 nm with larger core nanoparticles d_{core}=100 nm, but smaller core nanoparticles d_{core}=50 nm had average redshifts of more than 70 nm. (Fig. 6.5a) Thus using a fewer satellites and increasing the satellite size is one method of creating larger assembly redshifts. This understanding supports our earlier finding that smaller d_{core}=30 nm core nanoparticle with large $d_{satellite}$=50 nm satellites yielded the highest FOM.

The second approach is to consider the consequences that core size have on assembly redshift. Again, dampening effects occur as the core size increases, increasing the FWHM while decreasing the redshift. (Fig. 6.6b) These results suggest that minimizing the core size is appropriate strategy to increase peak shift, while maintaining narrow bandwidths. This analysis correlates with our prior results in Fig. 6.5 where small d_{core}=30 nm cores produce greater peak shifts with minimal band broadening. However, as mentioned before, the shortcoming of smaller core sizes is that the scattering cross-section is drastically reduced ($\sigma_s \propto r^6/\lambda^4$).

A final variable not investigated in the 2D nanoassembly system, but investigated with the Mie Theory simulation is the distance between the core and satellite particles. In our system, the length of the biomolecular tether can control the inter-particle distance. Decreasing the inter-particle core-satellite distance enhances the localized plasmon coupling, increasing the assembly redshift nonlinearly. This nonlinearity is particularly significant in systems where the core-satellite distance is less than 10 nm. In systems such as the nanoassembled substrate, reduced inter-particle distances will obstruct biomolecular recognition events. Thus there is a trade-off between the diffusion-limited transport of biomolecules to the space between two nanoparticles and maximizing the plasmon coupling to enhance the detectable signal of the sensor.

6.8 Determination of Proteolytic Enzyme Kinetics

As mentioned previously, the up-regulation of proteases from their homeostatic state can be indicative of a number of asymptomatic diseases such as oral cancer, rheumatoid arthritis, Sjorgen's syndrome, blood disorders, and cardiovascular disease. A theoretical analysis of the detection times for a number of prominent proteases found in various bodily fluids is given in Table 6.3. Using known enzyme kinetics, predicted detection times to cleave a core-satellite substrate specific for each protease were calculated to determine applicability of the substrate with the equation:

$$\frac{V_A}{V_B} = \frac{\left(\frac{K_{cat}}{K_m}\right)_A [E_A][S_A]}{\left(\frac{K_{cat}}{K_m}\right)_B [E_B][S_B]} = \frac{\left(\frac{K_{cat}}{K_m}\right)_A [E_A]}{\left(\frac{K_{cat}}{K_m}\right)_B [E_B]} \tag{6.3}$$

where V is the velocity of the reaction, K_{cat} is the catalytic constant, K_m is the Michaelis constant, [E] is the enzyme concentration, and [S] is the substrate concentration. The ratio is only valid when the substrate concentration is much less than the Michaelis constant, $[S] << K_m$. Table 6.3 was determined using the empirically determined time necessary for trypsin to disassemble the core-satellite substrate and resultantly, certain biomolecules were found to be better suited for detection than others. Proteases with higher K_{cat}/K_m values and at greater concentrations in the sample fluid facilitate detection in much less time than other proteases, making them better candidate biomolecules for our proposed detection system. Thrombin and clotting factor Xa/Va are proteases that could potentially be detected with the nanoassembled substrate, while clotting factors IXa/VIIIa, MMP-2, and acrosin are enzymatically slower requiring significant time for substrate disassembly.

Table 6.3: Predicted Detection Times for Physiologically Relevant Biosamples

Enzyme	Body Fluid	K_{cat}/K_m ($M^{-1}s^{-1}$)	K_{cat} (s^{-1})	K_m (M)	Physiological Concentration (M)	Predicted Detection Time (min)
Trypsin	Stomach Acid	$2.1x10^5$	39.9	$1.9x10^{-4}$	$1.04x10^{-4}$*	50**
Thrombin	Blood	$1.3x10^7$	91.0	$7.0x10^{-6}$	$2.7x10^{-6}$	~30
Factor Xa/Va	Blood	$1.1x10^9$	81.7	$7.6x10^{-8}$	$3.0x10^{-8}$ - $1.8x10^{-7}$	>5
Factor IXa/VIIIa	Blood	$3.2x10^7$	2.5	$8.0x10^{-8}$	$1.2x10^{-9}$ – $9.0x10^{-8}$	>378
MMP-2	Saliva	$5.4x10^4$	0.017	$1.7x10^{-5}$	$2.5x10^{-10}$ - $4.0x10^{-10}$	$>5.3x10^8$
Acrosin	Semen	$1.8x10^6$	77	$4.4x10^{-5}$	$1.2x10^{-6}$	>505

*Concentration used for substrate characterization; **Actual time; References: 34-41

Furthermore, the nanoassembled substrate might be a viable platform for determining enzyme kinetics of proteases, for which a single-substrate mechanism is typically applied using the Michaelis-Menten model:

$$[E]+[S]\underset{K_d}{\overset{K_a}{\leftrightarrow}}[ES]\xrightarrow{K_{cat}}[E]+[P] \tag{6.4}$$

where [P] is the product concentration, K_d is the dissociation constant, K_a is the association constant, and the Michaelis constant, k_m, is defined as:

$$K_m = \frac{K_d + K_{cat}}{K_a} \tag{6.5}$$

Current zymography and liquid-based cleavage assays detect the velocity of enzymatic activity by varying the substrate concentration to create a Michaelis-Menten plot. Typically in such assays, the substrate concentration is much greater than the enzyme concentration, [S] >> [E]. From this plot, K_m is defined as the substrate concentration at half maximum velocity, where the velocity is the increase in fluorescent intensity units per second, ΔI/sec:

$$V = \frac{V_{max}[S]}{K_m + [S]} \tag{6.6}$$

Accurate values of V_{max} and K_m are determined by linear least squares regression and can be represented on a double-reciprocal Lineweaver-Burk plot where:

$$\frac{1}{V} = \frac{K_m}{V_{max}[S]} + \frac{1}{V_{max}} \tag{6.7}$$

The proposed AuNP disassembly method has two main distinctions from common liquid-based assays. First, the peptide substrate concentration cannot be easily varied as with liquid-based assays. Second, transport of the enzyme is influenced by limited mass transport to the surface of the AuNP substrate and Michaelis-Menten kinetics do not apply. One way to address the first difference is to change the peptide substrate concentration by altering the self-assembly protocol (incubation time) to vary core AuNP density. Alternatively, core structures can be fabricated using nanofabrication techniques such as nanosphere lithography, photolithography, mold replication, stamping, or embossing. The second distinction can be accounted for by modifying the known surface receptor kinetics for optical plasmon resonance-based biosensors in instruments such as those made by Biacore. Myszka et al. have developed mass transport-influenced binding analysis for determining the reaction kinetics in Biacore flow cells using a two-compartment model.[42] The model uses ordinary differential equations to determine the mass transport of analyte from the flow channel (top compartment) to the nanoscale compartment along the biosensing surface (bottom compartment). (Fig. 6.7) This model is currently utilized in the accompanying software of the BIACORE systems. By modifying the reaction kinetics to include substrate hydrolysis, important enzyme kinetics can be determined.

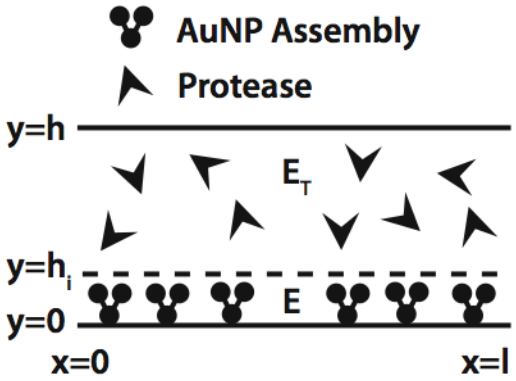

Figure 6.7: Two-compartment model used to derive equations for determination of reaction constants in a flow channel.

The enzyme concentration, E, of the bottom compartment adjacent to the AuNP surface is influenced by the initial concentration of the enzyme in the flow channel, E_T, and enzyme association, dissociation, and catalytic cleavage, constants:

$$\frac{d[E]}{dt} = -K_a[E]([S]-[ES]) + K_d[ES] + K_{cat}[ES] + K_t([E_T]-[E]) \tag{6.8}$$

where K_t is the diffusion-limited forward rate constant into the surface compartment. K_t has been proven to be defined by the enzyme diffusion constant D, the maximum flow velocity in the flow channel v_c, height h, and length l:

$$K_t = 1.282\left(\frac{v_c D^2}{hl}\right)^{\frac{1}{3}} \tag{6.9}$$

The substrate bound enzyme is defined as:

$$\frac{d[ES]}{dt} = K_a[E]([S]-[ES]) - K_d[ES] - K_{cat}[ES] \tag{6.10}$$

where the initial conditions for the flow channel at $t = 0$ are [E] = 0, [ES] = 0, and $[E_T]$ is the enzyme injection concentration.

A detection chamber 1 cm x 1 cm x 100 μm in size containing a biofluid with 100 pM of protease will have $5.9x10^{-14}$ moles of the molecule. This amount exceeds the approximated peptide substrate amount of $7.9x10^{-15}$ moles in an equal size chamber, as determined with a core density of $33.1x10^6$ cores/cm^2 and 15% of satellite surface area linked to one core AuNP. Techniques such as AFM or cleavage of fluorescently labels peptide could be used to characterize substrate concentrations. In individuals with periodontitis, the amount of protease in saliva will exceed the AuNP peptide concentration by ~7.5 times, allowing the detection of proteolytic activity. Typical hydrolysis assays have substrate concentrations in excess of 10^{-6} moles, thus this proposed assay may have shorter assay times. The velocity of the product, signaled by the release of AuNP satellites is:

$$\frac{dP}{dt} = K_{cat}[ES] \tag{6.11}$$

and the amount of product released is directly related to the intensity of green light at the 550 nm wavelength and the initial amount of peptide core-satellite linkers:

$$P = \left(\frac{I_{550nm,t} - I_{550nm,t_0}}{I_{550nm,t_\infty} - I_{550nm,t_0}}\right)\cdot 7.9x10^{-15} \tag{6.12}$$

where the baseline of the intensity is subtracted to remove potential unconjugated core AuNPs and normalized. Additionally, the amount of substrate which yields an optical response by the release of a AuNP satellite can be equally determined:

$$S_{core-satellite} = \left(\frac{I_{630nm,t} - I_{630nm,t_\infty}}{I_{630nm,t_0} - I_{630nm,t_\infty}}\right)\cdot 7.9x10^{-15} \tag{6.13}$$

where $S_{core-satellite}$ is the amount of substrate that is linking a core and satellite AuNP. It is approximated that ~3008 peptides, S, cover the upper 69% of the core AuNP, however only ~142 peptides, $S_{core-satellite}$, link the core to the satellite. These core-satellite linking peptide substrates amount to $7.9x10^{-15}$ moles in a 1 cm x 1 cm x 100 μm detection chamber and it is approximated that 16 times the core-satellite linkers equal the total peptide substrate present in the system, 16 x $S_{core-sate}$ = S.

Myszka et al. has demonstrated that a quasi-steady-state approximation can be made for the two compartment model by initially setting dE/dt = 0 since the concentration of enzyme, E, changes rapidly over a short period of time upon injection of the analyte (protease) and slowly thereafter. Since ES has been proven to change negligibly during the initial injection, ES = 0 during this rapid transient:

$$\frac{dE}{dt} = K_t[E_T] - [E](K_t + K_a[S]) \tag{6.14}$$

and the enzyme concentration is related as:

$$[E] = [E_T]\left(\frac{K_t}{K_t + K_a[S]}\right)\left(1 - e^{\frac{-t}{t_f}}\right) \tag{6.15}$$

where the fast transient time constant is related to the nanoscale height of the first compartment h_i:

$$t_f = \frac{h_i}{K_t + K_a[S]} \tag{6.16}$$

thus, enabling the combination of nonlinear least squares regression and the Levenberg-Marquardt method to solve for the kinetic parameters: K_a, K_d, K_{cat}, and K_t via numerical methods.[43] From this derivation, important reaction rate constants can be determined.

6.9 Future Directions

A portable power-free viewer and powered reader are potential conceptual tools to facilitate observation of the DF scatter from the core-satellite substrate and enable point-of-care detection. The power-free viewer would have an optical window through which the microfluidic chip will be observable and provide qualitative naked-eye detection. The viewer would be constructed with a port to insert the microfluidic chip and pinhole openings will allow the indirect illumination of light on the diagnostic chip. A glass or clear plastic lens will magnify the viewer to at least 10x and the casing, made from injection molded plastic, will be fused together to sandwich the internal lenses for cheap fabrication. A powered reader with total internal reflection (TIR) illumination and a CMOS/CCD sensor could be employed for quantitative real-time measurement of color change from the substrate. An internal LED would enable light to couple to the bottom of the microfluidic diagnostic device, enabling light scatter from the core-satellite nanoassemblies.

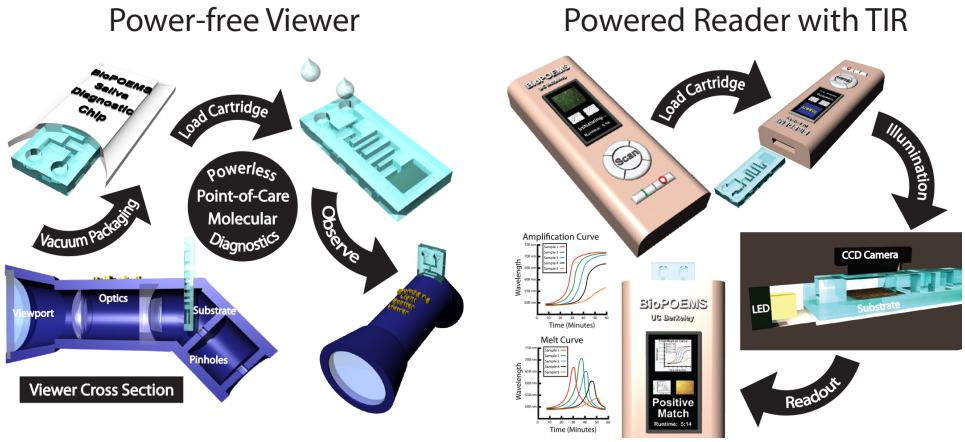

Figure 6.8: Conceptual renderings of a power-free viewer for qualitiative detection and powered reader for real-time measurement of color change from the nanoassembled substrate.

6.10 CONCLUSION

We have proposed an advancement upon the current suspension-based modality of colloidal biomolecular sensors that is better suited for on-chip diagnostic system integration while preserving the capability for diverse species detection. We present the fabrication of nanoassemblies self-assembled on a two-dimensional glass substrate, demonstrate the colorimetric functionality of biomolecular sensing *via* trypsin-mediated disassembly, and systematically analyze the optical detection properties of the substrate. A FOM was determined to quantify visual resolution the of the color change and nanoassemblies with 50 nm cores and either 30 nm or 50 nm satellites were concluded to be optimal. To the best of our knowledge, this plasmonic biosensor is the first self-assembled substrate that yields a structural color change directly at the site of disassembly. This new modality may enable a new generation of robust POC diagnostic devices with enhanced sensing capabilities.

6.11 ACKNOWLEDGEMENTS

Tim Wang and Benjamin M. Ross are co-authors of this work. Financial support was provided by grants from the National Institutes of Health (NIH) Nanomedicine Development Center for the Optical Control of Biological Function (Grant No. 3PN2 EY01824), Center for Nanostructured Materials and Technology (CNMT), National Academies Keck Futures Initiative funding (Grant No. NA-KFI Nano09), DARPA MF3 (Award No. HR0011-06-10050), and DARPA SERS S&T Fundamental Program under LLNL subcontract (Grant No. B573237). I acknowledge support from a National Science Foundation Graduate Research Fellowship and I thank N. Choudhary for her early contributions to the project. Yu-lin Xu provided the Fortran code for the Generalized Multiparticle Mie solution.

6.12 REFERENCES

1. Mirkin, C. A., Letsinger, R. L., Mucic, R. C. & Storhoff, J. J. A DNA-based method for rationally assembling nanoparticles into macroscopic materials. *Nature* **382**, 607–609 (1996).
2. Nykypanchuk, D., Maye, M. M., van der Lelie, D. & Gang, O. DNA-guided crystallization of colloidal nanoparticles. *Nature* **451**, 549–552 (2008).
3. Alivisatos, A. P. *et al.* Organization of 'nanocrystal molecules' using DNA. *Nature* **382**, 609–611 (1996).
4. Loweth, C. J., Caldwell, W. B., Peng, X., Alivisatos, A. P. & Schultz, P. G. DNA-Based Assembly of Gold Nanocrystals. *Angew Chem Int Edit* **38**, 1808–1812 (1999).
5. Yao, H., Yi, C., Tzang, C.-H., Zhu, J. & Yang, M. DNA-directed self-assembly of gold nanoparticles into binary and ternary nanostructures. *Nanotechnology* **18**, 015102 (2007).
6. Xu, X., Rosi, N. L., Wang, Y., Huo, F. & Mirkin, C. A. Asymmetric functionalization of gold nanoparticles with oligonucleotides. *J Am Chem Soc* **128**, 9286–9287 (2006).

7. Maye, M. M., Nykypanchuk, D., Cuisinier, M., van der Lelie, D. & Gang, O. Stepwise surface encoding for high-throughput assembly of nanoclusters. *Nat Mater* **8**, 388–391 (2009).
8. Sadasivan, S., Dujardin, E., Li, M., Johnson, C. J. & Mann, S. DNA-driven assembly of mesoporous silica/gold satellite nanostructures. *Small* **1**, 103–106 (2005).
9. Li, B. & Li, C. Y. Immobilizing au nanoparticles with polymer single crystals, patterning and asymmetric functionalization. *J Am Chem Soc* **129**, 12–13 (2007).
10. Sebba, D., Mock, J., Smith, D., Labean, T. & Lazarides, A. Reconfigurable Core-Satellite Nanoassemblies as Molecularly-Driven Plasmonic Switches. *Nano Lett* **8**, 1803–1808 (2008).
11. Sönnichsen, C., Reinhard, B. M., Liphardt, J. & Alivisatos, A. P. A molecular ruler based on plasmon coupling of single gold and silver nanoparticles. *Nat Biotechnol* **23**, 741–745 (2005).
12. Elghanian, R., Storhoff, J. J., Mucic, R. C., Letsinger, R. L. & Mirkin, C. A. Selective colorimetric detection of polynucleotides based on the distance-dependent optical properties of gold nanoparticles. *Science* **277**, 1078–1081 (1997).
13. Liu, J. & Lu, Y. Fast colorimetric sensing of adenosine and cocaine based on a general sensor design involving aptamers and nanoparticles. *Angew Chem Int Ed Engl* **45**, 90–94 (2006).
14. Liu, J. & Lu, Y. A colorimetric lead biosensor using DNAzyme-directed assembly of gold nanoparticles. *J Am Chem Soc* **125**, 6642–6643 (2003).
15. Jun, Y.-W. *et al.* Continuous imaging of plasmon rulers in live cells reveals early-stage caspase-3 activation at the single-molecule level. *P Natl Acad Sci Usa* **106**, 17735–17740 (2009).
16. Hirsch, L. R., Jackson, J. B., Lee, A., Halas, N. J. & West, J. L. A whole blood immunoassay using gold nanoshells. *Anal Chem* **75**, 2377–2381 (2003).
17. Myers, F. B. & Lee, L. P. Innovations in optical microfluidic technologies for point-of-care diagnostics. *Lab Chip* **8**, 2015–2031 (2008).
18. Anker, J. N. *et al.* Biosensing with plasmonic nanosensors. *Nat Mater* **7**, 442–453 (2008).
19. Zhao, W., Ali, M. M., Aguirre, S. D., Brook, M. A. & Li, Y. Paper-Based Bioassays Using Gold Nanoparticle Colorimetric Probes. *Anal Chem* **80**, 8431–8437 (2008).
20. Charrier, A., Candoni, N., Liachenko, N. & Thibaudau, F. 2D aggregation and selective desorption of nanoparticle probes: a new method to probe DNA mismatches and damages. *Biosensors and Bioelectronics* **22**, 1881–1886 (2007).
21. Ramseier, C. A. *et al.* Identification of pathogen and host-response markers correlated with periodontal disease. *J Periodontol* **80**, 436–446 (2009).
22. Tchetverikov, I. *et al.* MMP protein and activity levels in synovial fluid from patients with joint injury, inflammatory arthritis, and osteoarthritis. *Annals of the Rheumatic Diseases* **64**, 694–698 (2005).
23. Brawley, O., Ankerst, D. & Thompson, I. Screening for Prostate Cancer. *CA: A Cancer Journal for Clinicians* **59**, 264–273 (2009).
24. Herr, A. E. *et al.* Microfluidic immunoassays as rapid saliva-based clinical

diagnostics. *P Natl Acad Sci Usa* **104**, 5268–5273 (2007).
25. Turkevich, J., Stevenson, P. C. & Hillier, J. A study of the nucleation and growth processes in the synthesis of colloidal gold. *Discussions of the Faraday Society* **11**, 55–75 (1951).
26. Ross, B. M. & Lee, L. P. Comparison of near- and far-field measures for plasmon resonance of metallic nanoparticles. *Opt Lett* **34**, 896–898 (2009).
27. Wang, L. V. & Wu, H.-I. *Biomedical Optics*. (Wiley-Blackwell: 2007).
28. Schulz, L. G. The Optical Constants of Silver, Gold, Copper, and Aluminum. I. The Absorption Coefficient k. *JOSA, Vol. 44, Issue 5, pp. 357-362* **44**, 357–362 (1954).
29. Ordal, M. A. *et al.* Optical properties of the metals Al. Co, Cu, Au, Fe, Pb, Ni, Pd, Pt, Ag, Ti, and W in the infrared and far infrared. *Appl. Opt.* **22**, 1099–1120 (1983).
30. Palik, E. D. *Handbook of Optical Constants of Solids*. (Academic Press: San Diego, California, 1998).
31. Maier, I., Michael R A Morgan, S., Wolfgang Lindner & Pittner, F. Optical Resonance-Enhanced Absorption-Based Near-Field Immunochip Biosensor for Allergen Detection. *Anal Chem* **80**, 2694–2703 (2008).
32. Ross, B. M., Waldeisen, J. R., Wang, T. & Lee, L. P. Strategies for nanoplasmonic core-satellite biomolecular sensors: Theory-based Design. *Appl. Phys. Lett.* **95**, 193112 (2009).
33. Xu, Y. L. Electromagnetic scattering by an aggregate of spheres: far field. *Appl. Opt.* **36**, 9496–9508 (1997).
34. Dang, O. D., Vindigni, A. & Di Cera, E. An allosteric switch controls the procoagulant and anticoagulant activities of thrombin. *P Natl Acad Sci Usa* **92**, 5977–5981 (1995).
35. Kerschbaumer, R. J. *et al.* An antibody specific for coagulation factor IX enhances the activity of the intrinsic factor X-activating complex. *J Biol Chem* **279**, 40445–40450 (2004).
36. Nishimura, H. *et al.* Factor IX Fukuoka. Substitution of ASN92 by His in the second epidermal growth factor-like domain results in defective interaction with factors VIIa/X. *J Biol Chem* **268**, 24041–24046 (1993).
37. Butenas, S., Ribarik, N. & Mann, K. G. Synthetic substrates for human factor VIIa and factor VIIa-tissue factor. *Biochemistry* **32**, 6531–6538 (1993).
38. Nagase, H., Fields, C. G. & Fields, G. B. Design and characterization of a fluorogenic substrate selectively hydrolyzed by stromelysin 1 (matrix metalloproteinase-3). *J Biol Chem* **269**, 20952–20957 (1994).
39. Rai, B., Kharb, S., Jain, R. & Anand, S. C. Biomarkers of periodontitis in oral fluids. *J Oral Sci* **50**, 53–56 (2008).
40. Liu, D. Y. & Baker, H. W. Relationships between human sperm acrosin, acrosomes, morphology and fertilization in vitro. *Hum Reprod* **5**, 298–303 (1990).
41. Hardy, D. M., Schoots, A. F. & Hedrick, J. L. Caprine acrosin. Purification, characterization and proteolysis of the porcine zona pellucida. *Biochem J* **257**, 447–453 (1989).
42. Myszka, D. G., He, X., Dembo, M., Morton, T. A. & Goldstein, B. Extending the range of rate constants available from BIACORE: interpreting mass transport-

influenced binding data. *Biophysical Journal* **75**, 583–594 (1998).
43. Morton, T. A., Myszka, D. G. & Chaiken, I. M. Interpreting complex binding kinetics from optical biosensors: a comparison of analysis by linearization, the integrated rate equation, and numerical integration. *Analytical Biochemistry* **227**, 176–185 (1995).

CHAPTER 7

A REAL-TIME PCR ANTIBIOGRAM FOR DRUG-RESISTANT SEPSIS

7.1 ABSTRACT

Current molecular diagnostic techniques for susceptibility testing of septicemia rely on genotyping for the presence of known resistance cassettes. This technique is intrinsically vulnerable due to the inability to detect newly emergent resistance genes. Traditional phenotypic susceptibility testing has always been a superior method to assay for resistance; however, relying on the multi-day growth period to determine which antimicrobial to administer jeopardizes patient survival. These factors have resulted in the widespread and deleterious use of broad-spectrum antimicrobials. The real-time PCR antibiogram, described herein, combines universal phenotypic susceptibility testing with the rapid diagnostic capabilities of PCR. We have developed a procedure that determines susceptibility by monitoring pathogenic load with the highly conserved 16S rRNA gene in blood samples exposed to different antimicrobial drugs. The optimized protocol removes heme and human background DNA from blood, which allows standard real-time PCR detection systems to be employed with high sensitivity (<100 CFU/mL). Three strains of E. coli, two of which were antimicrobial resistant, were spiked into whole blood and exposed to three different antibiotics. After real-time PCR-based determination of pathogenic load, a $\Delta C_t < 3.0$ between untreated and treated samples was found to indicate antimicrobial resistance ($P < 0.01$). Minimum inhibitory concentration was determined for susceptible bacteria and pan-bacterial detection was demonstrated with 3 Gram-negative and 2 Gram-positive bacteria. Species identification was performed via analysis of the hypervariable amplicons. In summary, we have developed a universal diagnostic phenotyping technique that assays for the susceptibility of drug-resistant septicemia with the speed of PCR. The real-time PCR antibiogram achieves detection, susceptibility testing, minimum inhibitory concentration determination, and identification in less than 24 hours.

7.2 INTRODUCTION

Until now this thesis has focused on infectious disease detection at the point-of-care. However, point-of-care diagnostic devices are not applicable for the detection of all diseases. For example, sepsis is a disease unlikely to be detectable with the small volumes of capillary blood obtained by fingerstick. The small pathogenic loads in sepsis and severe microcirculatory dysfunction lead to reduced pathogenic load in capillary blood, precluding pathogen detection *via* fingerstick.[1-3] Sepsis is commonly defined as a bloodstream infection often caused by bacteria, although other microbes such as fungi and viruses can cause presentation of the disease. Mortality rates are reported between

35%-50%, with greater than 250,000 deaths occurring in the USA annually.[4] However, an important constituent to the mortality of sepsis is the body's own immune response. The cause of such high mortality rates is not directly caused by the microbe, but rather the massive immune response that leads to shock, multiple organ dysfunction, hypotension, lactic acidosis, diffuse intravascular coagulation, among other symptoms. The illness is often diagnosed upon the presentation of systemic inflammatory response syndrome (SIRS) and blood culture is performed upon suspected infection as a confirmatory rather than a diagnostic test. Although therapy is immediately initiated with the administration of broad-spectrum antibiotics, patient survival greatly relies upon response to immunosuppressants. Thus there is a grave inability to detect sepsis early before the patient presents SIRS. The disease progression septicemia begins with initial SIRS (low pathogenic load, <10 CFU/mL), followed by sepsis (~10-100 CFU/mL), to septic shock and organ dysfunction (high pathogenic load, >100 CFU/mL), and ultimately death. To diagnose a patient with sepsis, extremely sensitive recognition methods are needed with larger volumes (~mL) of blood obtained by venipuncture. Current molecular diagnostic technologies for septicemia have primarily focused on pathogen identification as a means to optimize antimicrobial therapy for patients. Such developments have included multiplexed PCR,[5,6] microarray platforms,[7,8] and chemiluminescent RNA probes[9] for the genetic detection of known bacterial and fungal organisms responsible for septicemia. Virulence and susceptibility are often deduced upon species identification as only a handful of known resistance genes can be screened with current commercial systems.[6] Compounding the issue of genotyping for resistance is the fact that the number of potential resistance genes scale with each pathogen, thus straining the limits of current diagnostic technology and economic feasibility. Despite this constraint, molecular diagnostic systems have demonstrated species identification in less than 24 hours, a drastic improvement in comparison to the gold standard culture-based susceptibility and Gram staining-based identification methods that yield results in 24 to 72 hours.[7,8,10,11] However, even though literature agrees that molecular diagnostic detection rapidly decreases the time to sepsis diagnosis, much debate over the accuracy of pathogen identification and hence, the appropriateness of the method for prescribing antimicrobial therapy remains.[5,6,12-16]

The anticipations of molecular diagnostic systems becoming the new gold standard for patient diagnosis have largely gone unmet and blood culture still remains as the *de facto* method to determine the course of patient treatment.[6,12-16] In light of the focus on molecular diagnostics, efforts to develop rapid techniques to directly test pathogen susceptibility are lacking.[17] In fact, we believe direct susceptibility testing of such blood-borne pathogens may be of greater importance than species identification via genotyping as the selective pressures of broad-spectrum antibiotic use have contributed to the increased incidence and virulence of antimicrobial resistant septicemia.[18-22] Universal susceptibility testing by genotyping for resistance is inferior to traditional phenotypic methods, as the microorganisms must be screened for a multitude of resistance cassettes. This approach has intrinsic vulnerabilities as more complicated and genetically diverse mechanisms of antimicrobial resistance have remained elusive.[22,23] Herein, we describe a method of direct susceptibility testing by monitoring phenotypic bacterial load via real-time PCR of spiked blood samples post-exposure to an array of antimicrobials. This

method combines rapid molecular diagnostic detection with the traditional benefits of phenotypic testing to achieve universal susceptibility analysis, minimum inhibitory concentration determination, and pathogen identification in blood in less than 24 hours.

7.3 EXPERIMENTAL OVERVIEW

The real-time PCR antibiogram utilizes antimicrobial exposure, preanalytic removal of heme and human background DNA, and colony PCR to assess pathogen susceptibility.[24,25] The optimized protocol is described below in the Materials and Methods Section of Appendix F. Briefly, 1 mL of spiked blood (~100 CFU/mL) is added to 9 mL of growth medium and incubated for 9 hours in various antibiotic environments. The sample is fractionated to separate red blood cells that contain heme, a PCR inhibitor. The supernatant, which consists of bacteria and mammalian cells, is pelleted and decanted. The pellet is then resuspended in mammalian lysis buffer and treated with DNase. This technique removes human DNA found in white blood cells from the sample, thus enhancing the sensitivity of detection. This is an essential part of this protocol as excess background human DNA can saturate the PCR amplification curves when using intercalating fluorophores. The sample is spun-down and the unseen bacterial cell pellet is washed in reticulocyte saline (RS) buffer. Preparation concludes by adding 2 μL of the sample directly to the PCR plate as template. This bacterial isolation method takes approximately 2-3 hours of manual labor, but could be automated to decrease sample preparation time and multiplexed for high-throughput testing in a clinical diagnostic laboratory setting.

A target pathogen concentration of ~100 CFU/mL was chosen to emulate levels found clinically in sepsis cases.[26-28] For bacteremia, greater than 50% of cases are low-grade (<10 CFU/mL) and ~25% of cases are high-grade bacteremia (>100 CFU/mL), thus necessitating a detection sensitivity of at least 100 CFU/mL.

7.4 THE REAL-TIME PCR ANTIBIOGRAM

Real-time colony PCR is performed using universal forward and reverse primers specific for the highly conserved region of the 16S ribosomal RNA gene sequence (Table 7.1).[29] Real-time PCR enables the comparison of bacterial load after antibiotic exposure by monitoring the amount of 16S rDNA present. The Bio-Rad iQ5 real-time PCR detection system used in this investigation was determined to have a detection limit of approximately $2x10^4$ CFU/mL, thus necessitating an incubation time of at least 8 hours. Figure 7.1 depicts the serial dilutions and incubation time curves used to determine the colony PCR detection limit to optimize the procedure for sample preparation.

Table 7.1: Universal Primers for the 16S rRNA Gene

Primer	Sequence (5' → 3')
Forward	AGAGTTTGATCMTGGCTCAG
Reverse	CTGCTGCSYCCCGTAG

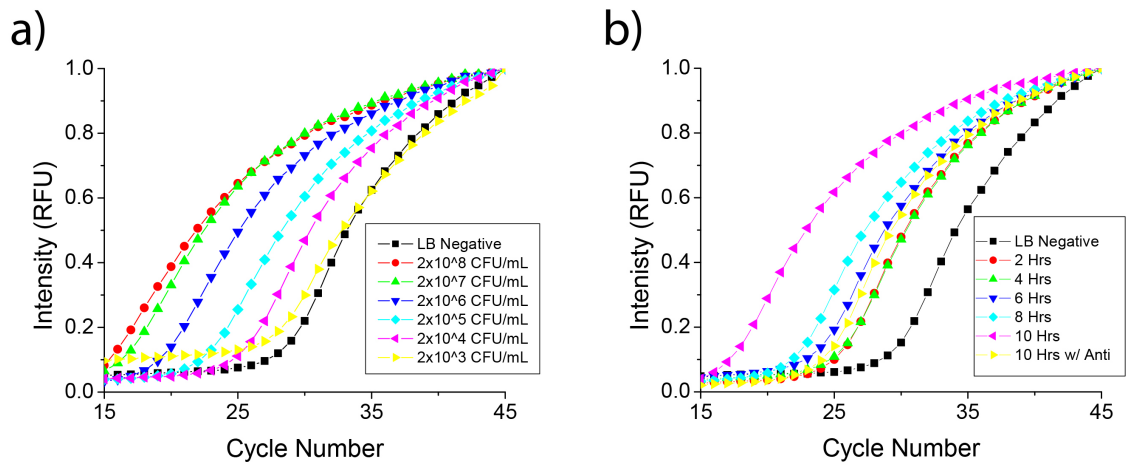

Figure 7.1: Protocol optimization for the Bio-Rad iQ5 PCR detection system. a) A limit of detection (LOD) of $2x10^4$ CFU/mL was determined for colony PCR, although lower limits have been reported. b) Optimization of our experimental protocol necessitates an incubation time of 8+ hours to differentiate bacterial growth from the initial concentrations found in septicemia.

The real-time PCR antibiogram method determines susceptibility in less than 24 hours, an improvement upon traditional phenotypic methods such as CO_2 monitoring and agar dilution methods, which require 24 to 72 hours. The decreased time to detection using the real-time PCR antibiogram method is depicted in Figure 7.2 and illustrates how phenotypic response can be combined with the diagnostic speed of PCR to yield drastically decreased detection times of antibiotic resistance. A traditional antibiogram takes 2+ days (left). The real-time PCR antibiogram (middle) is determined by measuring the change in ΔC_t values for different antibiotics against an untreated control. Variations in bacterial load post-exposure to an array of antibiotics are amplified by PCR, thus allowing pathogen detection and susceptibility to be obtained in much less time. Parameters for the simulation were optimized using experimental data and incubation times greater than 8+ hours allowed our detection system to assay cultures at ~100 CFU/mL. The three-hour horizontal dashes before amplification depict manual sample preparation time.

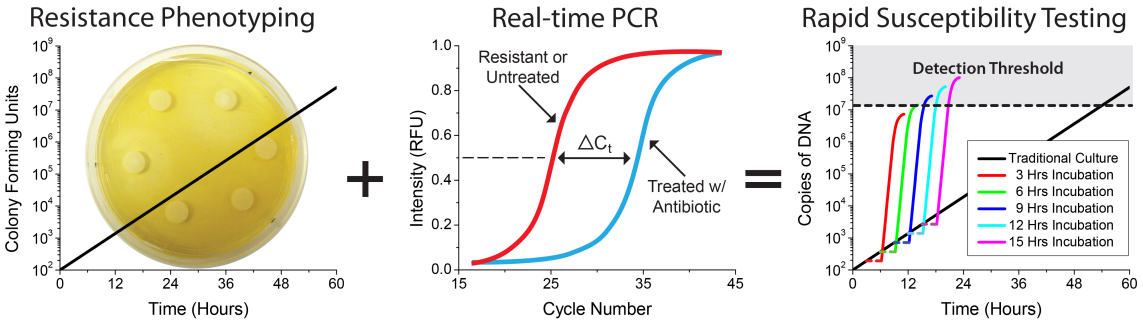

Figure 7.2: The real-time PCR antibiogram achieves rapid susceptibility testing of septicemia in less than 24 hours. Schematic that illustrates how phenotypic response can be monitored with the diagnostic speed of PCR to yield drastically decreased detection times. A traditional antibiogram takes 2+ days (left). The real-time PCR antibiogram (middle) is determined by measuring the change in ΔC_t

values for different antibiotics against a control. Parameters for the simulation (right) were optimized using experimental data and incubation times greater than 8+ hours allowed our detection system to assay cultures at ~100 CFU/mL. The three-hour horizontal dashes before amplification depict manual sample preparation time.

7.5 SUSCEPTIBILITY AND MINIMUM INHIBITORY CONCENTRATION TESTING

The developed assay was performed on three strains of E. coli, two of which are resistant, for three types of antibiotics: kanamycin, spectinomycin, and chloramphenicol. (Figure 7.3) These three small molecule antibiotics have similar molecular weight (300-500 g/mol) and similar mechanisms of action that interrupt protein synthesis. Kanamycin and spectinomycin bind to the 30S subunit of the bacterial ribosome and chloramphenicol binds to the 50S ribosomal subunit. The real-time PCR antibiogram determines resistance by monitoring the relative difference in pathogenic bacterial load between treated and untreated blood samples. The cycle threshold difference (ΔC_t) is defined as:

$$\Delta C_t = C_t\left(\text{antibiotic}\right) - C_t\left(\text{untreated}\right) \qquad (7.1)$$

All experiments were performed in triplicate, normalized, and the C_t value was defined as the cycle number in which the normalized amplification curve crossed 0.5. ΔC_t values >3.0 were assigned to indicate susceptibility, while ΔC_t values <3.0 designate resistance. We acknowledge that this cutoff value is arbitrary and is dependent upon a number of variables intrinsic to the diagnostic equipment being used. We observed no inhibition of PCR amplification from residual Heme or from any of the three antibiotics. Susceptible E. coli produced low bacterial loads when exposed to all three of the antibiotics and large ΔC_t values indicated susceptibility. (Figure 7.3a and 7.3c) Spectinomycin resistant E. coli produced low bacterial loads to all the antibiotics except when incubated in the presence of spectinomycin, thus yielding a significantly lower ΔC_t value. (Figure 7.3b and 7.3d) Similarly, kanamycin resistant E. coli produced the same result when incubation was performed with kanamycin. (Figure 7.3e and 7.3g) The real-time PCR antibiogram matrix summarizes the susceptibility results, as depicted in Table 7.2. Comparison of spectinomycin ΔC_t values between susceptible and spectinomycin resistant E. coli confirmed a significant statistical difference. (Appendix F and Figure F1) Next, minimum inhibitory concentration was determined for blood samples spiked with E. coli susceptible to spectinomycin. The samples were incubated in four different concentrations of spectinomycin and there is a significant difference in the ΔC_t value at concentrations below the minimum inhibitory concentration. (Figure 7.3f and 7.3h) Figure 7.3 illustrates how the real-time PCR antibiogram can determine the optimal patient-specific antimicrobial concentration for administration in addition to aiding antimicrobial selection.

Table 7.2: Real-time PCR Antibiogram Matrix for Susceptibility Testing

	Kanamycin	Spectinomycin	Chloramphenicol
Susceptible E. coli	+6.2	+6.0	+7.0
Kanamycin Resistant	**-1.0**	+6.3	+5.7
Spectinomycin Resistant	+11.2	**+1.0**	+11.1

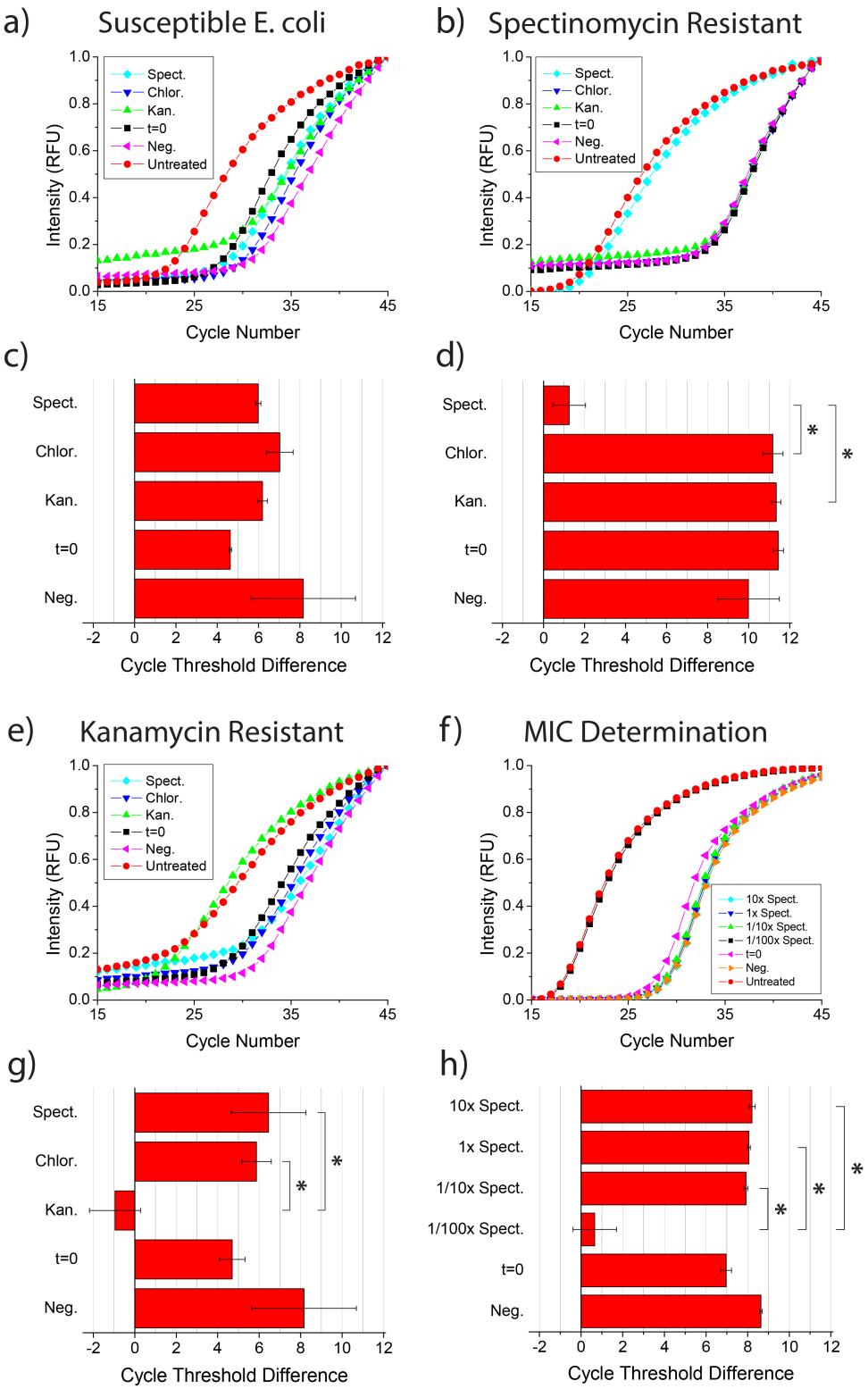

Figure 7.3: The real-time PCR antibiogram for aiding antimicrobial selection and administration. a,b,e,f) Real-time PCR amplification curves for measuring the susceptibility of susceptible, spectinomycin resistant, kanamycin resistant, and the minimum inhibitory concentration of E. coli spiked in blood. Amplification curves were performed in triplicate. c,d,g,h) The corresponding ΔC_t values for the real-

time amplification curves. ΔC_t values >3.0 were assigned to indicate susceptibility, while ΔC_t values <3.0 designate resistance. *P < 0.01 for multiple comparisons by the Holm *t* Test. t=0 signifies initial bacterial levels with no incubation and negative curves denote sample preparation with no bacteria. Susceptible E. coli was used for minimum inhibitory concentration determination and 1x designates a spectinomycin concentration of 50 μg/mL.

It is important to note that the cutoff value for ΔC_t is dependent upon factors intrinsic to the real-time PCR detection system employed, such as the cycle time, amplification efficiency of the polymerase, and dynamic range of the fluorescent detection window of the system. Thus we aim to provide a conceptualized approach to determining resistance that will need further clinical optimization. We anticipate that advanced stages of sepsis will have higher ΔC_t values needed to indicate resistance as pathogenic load generally correlates with the severity of sepsis (i.e. SIRS vs. sepsis vs. septic shock) and larger pathogenic loads will have greater deviation between patients. Cases in which there is partial antibiotic resistance, such as with efflux pump upregulation and partial resistance to glycopeptide antibiotics conferred by the thickening of the bacterial cell wall, MIC determination would ascertain the antibiotic concentration or combination of antibiotics necessary for therapy.

7.6 Pan-bacterial Detection and Identification

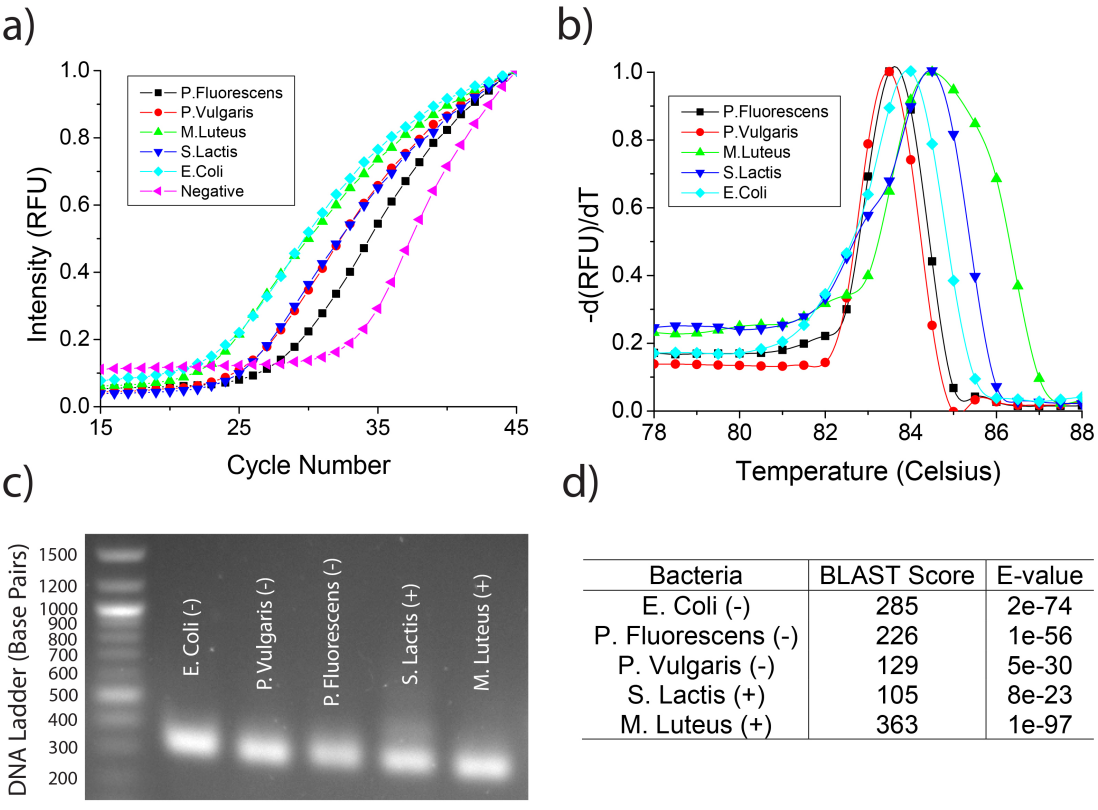

Bacteria	BLAST Score	E-value
E. Coli (-)	285	2e-74
P. Fluorescens (-)	226	1e-56
P. Vulgaris (-)	129	5e-30
S. Lactis (+)	105	8e-23
M. Luteus (+)	363	1e-97

Figure 7.4: The real-time PCR antibiogram for pan-bacterial detection and identification. a) Pan-bacterial amplification illustrates universal binding of the highly conserved 16S rDNA primers and b) melt curve analysis provides evidence that consistent, species-specific amplicons were generated. c) Amplicons on gel

electrophoresis exhibit similar lengths of 200-300 base pairs and d) sequences submitted to the BLAST are readily identifiable.

Given the large population of microbes that can cause sepsis, pan-bacterial amplification was demonstrated with 3 Gram-negative and 2 Gram-positive bacteria. (Figure 7.4a) Melt curve analysis illustrated how the primers produced consistent, species-specific amplicons. (Figure 7.4b) The amplified 16S rDNA amplicons, which are approximately 200-300 base pairs in length, contain hypervariable regions that are capable of enabling species-specific bacterial identification. (Figure 7.4C) Sequenced amplicons were submitted to the BLAST database and the original species were readily identifiable. (Figure 7.4D) Species identification could be equally obtained using multiplexed molecular probes found in current commercial diagnostic PCR systems such as the Roche LightCycler® SeptiFast system.

7.7 COMPARISON TO COMMERCIAL TECHNIQUES

The current gold standard is detection by microbial culture. Systems such as the bioMerieux BacT/Alert® provide automated detection by monitoring metabolic products. For aerobic bacteremia, microbial incubation tubes have a fluorescent compound that reacts with CO_2, allowing real-time analysis. However, long culture times are required, typically >72 hours with some incubations requiring up to 5 or 6 days before positive identification of pathogen.[8,13] Additionally, different incubation tubes need to be used for suspected bacteremia, viremia, and fungemia. Recently, the Roche LightCycler® SeptiFast system has challenged gold standard incubation-based methods and drastically reduced the time-to-detection to less than 6 hours.[6,8,13,15,30] This technology utilizes multiplexed real-time PCR to detect 25 pathogens with molecular beacons. The amplification reaction employs 25 primer sets by recording fluorescence on 5 channels. Each fluorescent channel has 5 molecular beacons, each with a different melting point, thus melt curve analysis enables pathogen identification. Although the LightCycler® SeptiFast system has higher sensitivity than the BacT/Alert® system, worse specificities are reported. (Table 7.3) This is a major barrier for the technology as specificity is more critical than sensitivity in diagnostics. The LightCycler® is approved for clinical use in Europe, but has not been approved by the FDA here in America. The Real-time PCR Antibiogram combines the benefits of both techniques: the specificity of microbial incubation with the rapid time-to-detection capability of real-time PCR.

Table 7.3: Comparison to Commercial Techniques

Technique	Time to Diagnosis	Detects Emergent Strains	Requisite Labor	Sensitivity	Specificity
Gold Standard: Blood Culture (BacT/Alert®)	24 Hrs[15] - 6 Days[8,13]	**Yes**	**Semi-Automated**	75.0%,[15] 94.7%[8]	96.8%,[15] **98.8%**[8]
Real-time PCR (LightCycler® SeptiFast)	**<6 Hrs**[31]	No	**Semi-Automated**	90.9%,[15] **98.8%**[31]	90.1%,[15] Variable[31]
Real-time PCR Antibiogram	<10-18 Hrs	**Yes**	**Manual, can be Automated**	**98.8%?**	**98.8%?**

7.8 CONCLUSION

Recent innovations in susceptibility testing have largely failed to transcend the gold standard culture-based methods that have dominated clinical diagnostic laboratory protocols for the past 50+ years. Susceptibility testing of septicemia relies on either extended multi-day phenotypic methods that jeopardize patient survival or molecular genotyping techniques that are limited by the number of resistance cassettes the system can detect and that are unable to detect newly emergent resistance genes. These issues have resulted in the pervasive administration of broad-spectrum antimicrobials and the increased incidence and virulence of antimicrobial resistant septicemia.

By combining universal phenotypic susceptibility testing with the rapid diagnostic capabilities of PCR, we have developed a superior method of direct susceptibility testing. The procedure determines susceptibility by monitoring pathogenic load with the highly conserved 16S rRNA gene in blood samples exposed to different antimicrobial drugs. The optimized protocol removes heme and human background DNA from blood, which allows standard real-time PCR detection systems to be employed with high sensitivity (<100 CFU/mL). The real-time PCR antibiogram achieves detection, susceptibility testing, minimum inhibitory concentration determination, and identification in less than 24 hours. We anticipate the uptake of this technique to continue with subsequent clinical testing and comparison to the current standards of sepsis diagnosis and treatment.

7.9 ACKNOWLEDGEMENTS

Tim Wang and Debkishore Mitra are co-authors of this work. Financial support was provided by grants from the Korean Institute for Advancement of Technology and the Center for Nanostructured Materials and Technology (CNMT). I acknowledge support from a National Science Foundation Graduate Research Fellowship. I thank Terry Johnson and Megan Dueck for access to the Bio-Rad iQ5 real-time PCR detection system, Jin Huh and the J. Christopher Anderson Lab for donating the E. coli used in this investigation, and the PLoS ONE reviewer for helpful feedback.

7.10 REFERENCES

1. Diaz, N. L. Histochemical and ultrastructural study of skeletal muscle in patients with sepsis and multiple organ failure syndrome (MOFS). *Histology and Histopathology* **13**, 121–128 (1998).
2. De Backer, D., Creteur, J., Preiser, J.-C., Dubois, M.-J. & Vincent, J.-L. Microvascular Blood Flow Is Altered in Patients with Sepsis. *American Journal of Respiratory and Critical Care Medicine* **166**, 98–104 (2002).
3. Lehr, H. A., Bittinger, F. & Kirkpatrick, C. J. Microcirculatory dysfunction in sepsis: a pathogenetic basis for therapy? *J. Pathol.* **190**, 373–386 (2000).
4. Cromer, J. R., Wood, S. J., Miller, K. A., Nguyen, T. & David, S. A. Functionalized dendrimers as endotoxin sponges. *Bioorg Med Chem Lett* **15**, 1295–1298 (2005).

5. Lilienfeld-Toal, Von, M. *et al.* Utility of a commercially available multiplex real-time PCR assay to detect bacterial and fungal pathogens in febrile neutropenia. *J Clin Microbiol* **47**, 2405–2410 (2009).
6. Yanagihara, K. *et al.* Evaluation of pathogen detection from clinical samples by real-time polymerase chain reaction using a sepsis pathogen DNA detection kit. *Crit Care* **14**, R159 (2010).
7. Cleven, B. *et al.* Identification and Characterization of Bacterial Pathogens Causing Bloodstream Infections by DNA Microarray. *J Clin Microbiol* **44**, 2389 (2006).
8. Tissari, P. *et al.* Accurate and rapid identification of bacterial species from positive blood cultures with a DNA-based microarray platform: an observational study. *Lancet* **375**, 224–230 (2010).
9. Lindholm, L. & Sarkkinen, H. Direct identification of gram-positive cocci from routine blood cultures by using AccuProbe tests. *J Clin Microbiol* **42**, 5609–5613 (2004).
10. Wiegand, I., Hilpert, K. & Hancock, R. E. W. Agar and broth dilution methods to determine the minimal inhibitory concentration (MIC) of antimicrobial substances. *Nat Protoc* **3**, 163–175 (2008).
11. Zhang, S. X. *et al.* Evaluation of CLSI agar dilution method and Trek Sensititre broth microdilution panel for determining antimicrobial susceptibility of Streptococcus pneumoniae. *J Clin Microbiol* **49**, 704–706 (2011).
12. Reier-Nilsen, T., Farstad, T., Nakstad, B., Lauvrak, V. & Steinbakk, M. Comparison of broad range 16S rDNA PCR and conventional blood culture for diagnosis of sepsis in the newborn: a case control study. *BMC Pediatrics 2009 9:5* **9**, 5 (2009).
13. Wallet, F. *et al.* Preliminary clinical study using a multiplex real-time PCR test for the detection of bacterial and fungal DNA directly in blood. *Clinical Microbiology and Infection* **16**, 774–779 (2010).
14. Bauer, M. & Reinhart, K. Molecular diagnostics of sepsis-Where are we today? *International journal of medical microbiology : IJMM* (2010).doi:10.1016/j.ijmm.2010.04.006
15. Avolio, M. *et al.* Molecular identification of bloodstream pathogens in patients presenting to the emergency department with suspected sepsis. *Shock* **34**, 27–30 (2010).
16. Vince, A. *et al.* LightCycler SeptiFast assay as a tool for the rapid diagnosis of sepsis in patients during antimicrobial therapy. *Journal of Medical Microbiology* **57**, 1306 (2008).
17. Sener, S., Acuner, I. C., Bek, Y. & Durupinar, B. Colorimetric-Plate Method for Rapid Disk Diffusion Susceptibility Testing of Escherichia coli. *J Clin Microbiol* **49**, 1124–1127 (2011).
18. Figueiredo Costa, S. Impact of antimicrobial resistance on the treatment and outcome of patients with sepsis. *Shock* **30 Suppl 1**, 23–29 (2008).
19. Shopsin, B., Gomez, M., Waddington, M., Riehman, M. & Kreiswirth, B. N. Use of coagulase gene (coa) repeat region nucleotide sequences for typing of methicillin-resistant Staphylococcus aureus strains. *J Clin Microbiol* **38**, 3453–3456 (2000).

20. Boakes, E. *et al.* Distinct bacteriophages encoding Panton-Valentine leukocidin (PVL) among international methicillin-resistant Staphylococcus aureus clones harboring PVL. *J Clin Microbiol* **49**, 684–692 (2011).
21. Blanc, D. S. *et al.* High proportion of wrongly identified methicillin-resistant Staphylococcus aureus carriers by use of a rapid commercial PCR assay due to presence of staphylococcal cassette chromosome element lacking the mecA gene. *J Clin Microbiol* **49**, 722–724 (2011).
22. Stutz, K., Stephan, R. & Tasara, T. SpA, ClfA, and FnbA genetic variations lead to Staphaurex test-negative phenotypes in bovine mastitis Staphylococcus aureus isolates. *J Clin Microbiol* **49**, 638–646 (2011).
23. Procop, G. W. Molecular diagnostics for the detection and characterization of microbial pathogens. *Clin Infect Dis* **45 Suppl 2**, S99–S111 (2007).
24. Handschur, M., Karlic, H., Hertel, C., Pfeilstöcker, M. & Haslberger, A. G. Preanalytic removal of human DNA eliminates false signals in general 16S rDNA PCR monitoring of bacterial pathogens in blood. *Comp Immunol Microbiol Infect Dis* **32**, 207–219 (2009).
25. Rolain, J. M., Mallet, M. N., Fournier, P. E. & Raoult, D. Real-time PCR for universal antibiotic susceptibility testing. *Journal of Antimicrobial Chemotherapy* **54**, 538–541 (2004).
26. Phillips, S. E. & Bradley, J. S. Bacteremia detected by lysis direct plating in a neonatal intensive care unit. *J Clin Microbiol* **28**, 1–4 (1990).
27. Kellogg, J. A., Manzella, J. P. & Bankert, D. A. Frequency of low-level bacteremia in children from birth to fifteen years of age. *J Clin Microbiol* **38**, 2181–2185 (2000).
28. Walsh, A. L. *et al.* Prognostic significance of quantitative bacteremia in septicemic melioidosis. *Clin Infect Dis* **21**, 1498–1500 (1995).
29. Lane, D. J. 16S/23S rRNA sequencing. *Nucleic acid techniques in bacterial systematics* (2004).
30. Nguyen, D. T. *et al.* Real-time PCR testing for mecA reduces vancomycin usage and length of hospitalization for patients infected with methicillin-sensitive staphylococci. *J Clin Microbiol* **48**, 785–790 (2010).
31. Lehmann, L. E. *et al.* A multiplex real-time PCR assay for rapid detection and differentiation of 25 bacterial and fungal pathogens from whole blood samples. *Med. Microbiol. Immunol.* **197**, 313–324 (2008).

CHAPTER 8

FUTURE DIRECTIONS

8.1 CONCLUSION

This dissertation describes an effort to employ new microfluidic technologies to point-of-care devices for infectious disease testing and patient self-monitoring. Degas-driven fluid flow was a central theme to many of the chapters and I believe that many improvements are to come. Further exploration will undoubtedly discover ways to improve flow stability, allow flow rate control, and enable propulsion of multiple fluids within one fluidic network. This simple method of fluid actuation is the bridge between the dependable mechanism of capillary action found in lateral flow assays and state-of-the-art microfluidic component technology that has been developed in the past two decades.

The advancement of isothermal amplification techniques for nucleic acid detection, both DNA and RNA, are of great importance to the diagnostic community. Recombinase polymerase amplification is a highly attractive reaction that can amplify nucleic acids at 37°C. At such low amplification temperatures, exothermal reactions could facilitate on-chip reactions. However, this emerging technique still has its share of growing pains as primer design is complicated, detection is commonly performed with molecular beacons, and vital detection specifications are unknown (sensitivity and specificity). New signal amplification schemes for antibody recognition and protein detection will be necessary to develop a complete diagnostic assay. The nanoassembly method I proposed is an example of the enhancement factors that can be obtained with nanoplasmonics. Other schemes utilizing visual and structural color change mechanisms are powerful methods that have yet to be integrated into diagnostic devices. As science progresses, research and technology undoubtedly become more interdisciplinary. The future of point-of-care diagnostics will rely upon the microfluidic community accepting and integrating unfamiliar techniques. Much of the work I performed for DARPA and the Bill and Melinda Gates Foundation grants forced me to understand how diagnostic testing is currently performed in both the developed and undeveloped worlds. Surprisingly, disease diagnostics is still highly dependent upon evaluation of patient symptoms regardless of the location. Front-line diagnostic technology exists minimally in healthcare universally around the globe and improvements made in the developing world will certainly translate to the developed world.

Finally, there are diseases where the direct detection of pathogenic biomarkers with microfluidic diagnostic devices is impractical. A prime example is sepsis. When systemic inflammatory response syndrome develops (SIRS) before full-blown sepsis, bacterial loads are ~10 CFU/mL. The current detection limit with PCR is 3 CFU/mL, thus the detection volumes in a microfluidic device are infeasible. As demonstrated in

Chapter 7, detection and susceptibility within 24 hours is essential and possible. Additionally, with the FDA blocking approval of Roche's Septifast platform, alternative detection methods for sepsis are critical. Even though sepsis is the tenth most common disease leading to death, very little research is performed on sepsis and early detection technologies. One possible way to detect sepsis is to monitor the body's innate immune response. Activation of specific toll-like receptors could be used to deduce the pathogen present in the patient and direct therapeutic prescription. Ultimately, the microfluidic research must sometimes accept the fact that certain diagnostics must be left to the centralized clinical laboratory.

In summary, the work during my graduate career has afforded me the opportunity to immerse myself in several fields and I intend to continue forward upon the eclectic research path that I have come to know so well.

APPENDIX

APPENDIX A: SIMULATION OF DEGAS-DRIVEN FLUID FLOW

Derivation of Equation 2.5

The following is a derivation of an extension of the Navier-Stokes equation that accounts for the continuous change in pressure within the microfluidic channel. Typical pressure driven fluid flow assumes that the pressure gradient driving fluid flow is constant:

$$\frac{\partial^2 u}{\partial y^2}+\frac{\partial^2 u}{\partial z^2}=-\frac{1}{\mu}\frac{\partial P}{\partial x} \tag{A.1}$$

However, with pressure driven fluid flow where the pressure gradient is not constant and Netwon's second law can be applied. Here, the momentum change (LHS) is balanced by the surface tension force, instantaneous pressure difference, and the viscous force, respectively from left to right.

$$\frac{\partial\left(\rho HWl\frac{dl}{dt}\right)}{\partial t}=2\sigma\cos\theta\left(1+\beta\right)+\left(P_{atm}-P_{channel}\right)W-\frac{12\mu l}{W\gamma}\frac{dl}{dt} \tag{A.2}$$

where γ is the adjustment factor for fluid flow in a rectangular microchannel:

$$\gamma=1-192\alpha\sum_{i=1,3,5\ldots}^{\infty}\frac{\tanh\left(\frac{i\pi}{2\alpha}\right)}{\left(i\pi\right)^5} \tag{A.3}$$

In typical pressure driven flow, the LHS of equation 2 is equal to zero since the pressure gradient is constant and the fluid flow is fully developed. The solution is:

$$U_{ave}=\frac{\left(2\sigma\cos\theta\left(\frac{1}{w}+\frac{1}{h}\right)+\left(P_{atm}-P_{channel}\right)\right)w^2\gamma}{12\mu l} \tag{A.4}$$

However, in degas-driven flow, the fluid plug has momentum and its inertia resists subtle changes in the flow rate. To solve this partial differential equation, the following substitution is made to allow the second-order linear differential equation to be solved.

$$l\frac{dl}{dt}=\frac{1}{2}\frac{dl^2}{dt} \tag{A.5}$$

The equation governing fluid flow now has the form:

$$\frac{\rho HW}{2}\frac{d^2l^2}{dt^2}=2\sigma\cos\theta\left(1+\beta\right)+\left(P_{atm}-P_{channel}\right)W-\frac{6\mu}{W\gamma}\frac{dl^2}{dt} \tag{A.6}$$

Another substitution, *v(t)*, then allows the equation to take the form of a first-order inhomogeneous differential equation:

$$v(t)=\frac{dl^2}{dt} \tag{A.7}$$

$$\frac{dv}{dt}+\frac{12\mu}{\gamma\rho HW^2}v=\frac{4\sigma\cos\theta(1+\beta)+2(P_{atm}-P_{channel})W}{\rho HW} \tag{A.8}$$

which can be multiplied by the integrating factor, $e^{\frac{12\mu}{\gamma\rho HW^2}t}$:

$$\frac{d\left(v\cdot e^{\frac{12\mu}{\gamma\rho HW^2}t}\right)}{dt}=\frac{4\sigma\cos\theta(1+\beta)+2(P_{atm}-P_{channel})W}{\rho HW}e^{\frac{12\mu}{\gamma\rho HW^2}t} \tag{A.9}$$

and integration by parts then yields:

$$v\cdot e^{\frac{12\mu}{\gamma\rho HW^2}t}=\frac{4\sigma\cos\theta(1+\beta)W\gamma}{12\mu}e^{\frac{12\mu}{\gamma\rho HW^2}t}+\frac{(P_{atm}-P_{channel})W^2\gamma}{6\mu}e^{\frac{12\mu}{\gamma\rho HW^2}t}+\frac{W^2\gamma}{6\mu}e^{\frac{12\mu}{\gamma\rho HW^2}t}\int\left(\frac{dP_{channel}}{dt}\bigg|_t\right)dt \tag{A.10}$$

where the average flow velocity can be obtained (assuming the atmospheric pressure driving fluid flow is constant):

$$\frac{dl}{dt}=U_{ave}=\frac{\gamma w^2}{12\mu l}\left(\frac{2\sigma\cos\theta(1+\alpha)}{w}+(P_{atm}-P_{channel})+\int_{T-\varepsilon}^{T}\left(\frac{dP_{channel}}{dt}\bigg|_{t=T}\right)dt\right) \tag{A.11}$$

The equation is similar to equation A.4, however the instantaneous change in the pressure gradient is subtracted from the entire pressure gradient, thus enabling inertial effects to counter sudden pressure changes within the microchannel and thus effectively modeling a slower flow rate than was originally simulated.

Supplementary Figures

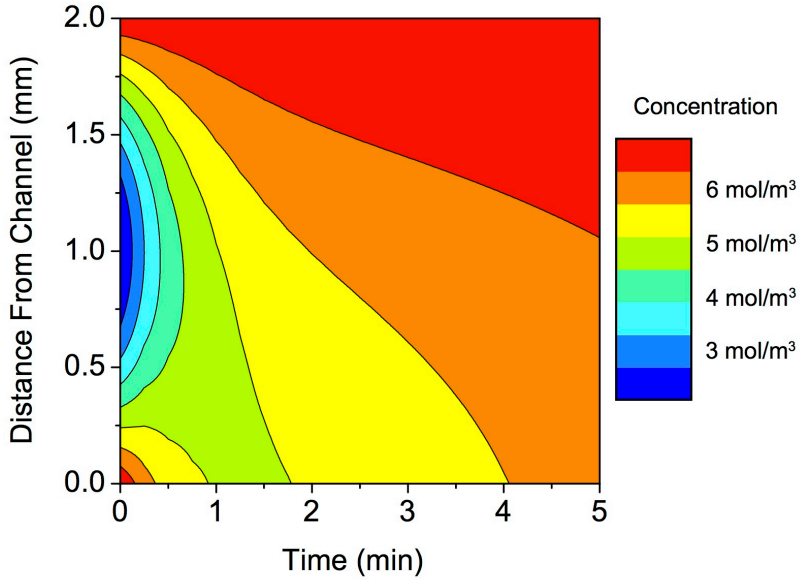

Figure A1: Time-lapse, spatial concentration profile across a 2 mm PDMS degassing layer adjacent to an empty microchannel. The figure is a visual depiction of the line graph in Fig. 2.2d.

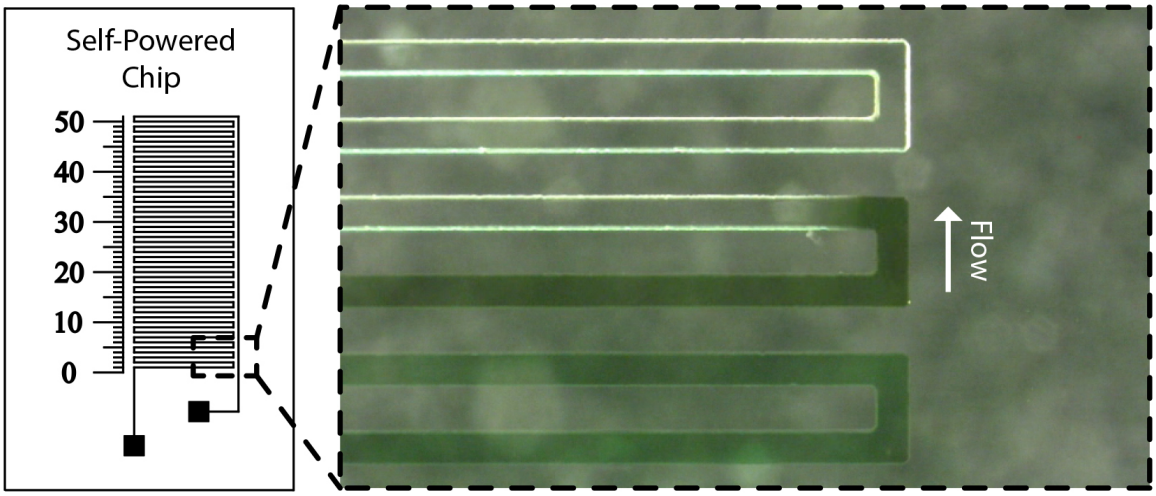

Figure A2: Schematic of the monolithic PDMS device used to validate the predictive model of degas-driven fluid flow (left). Fluid flow was visualized with green dye and observed in a Keyence VHX-500F digital microscope with a frame rate of 16 fps (right).

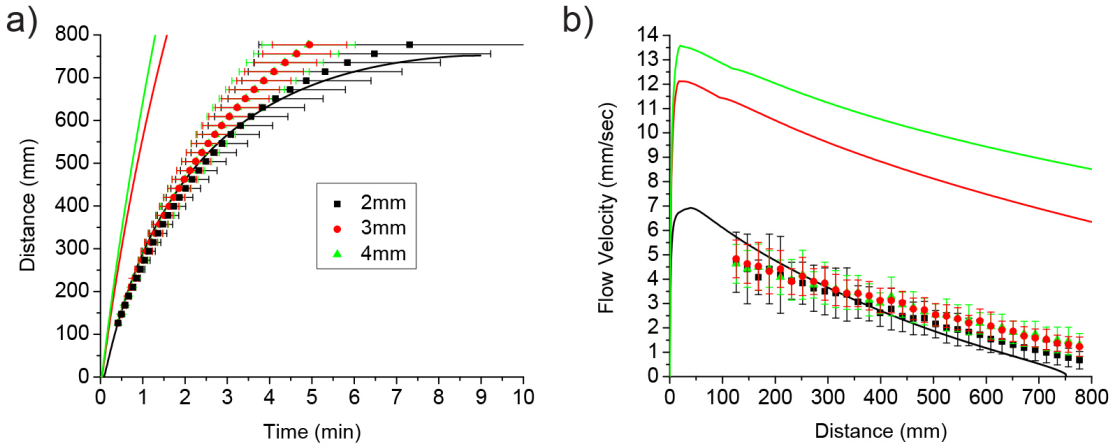

Figure A3: The 1D assumption of diffusion in a plane sheet was evaluated with devices of three different thicknesses. Monolithic PDMS devices (n=5) 2, 3, and 4 mm thick with a 4 mm boundary around the perimeter of the channels were used to determine the thickness at which diffusion in the y- and z-axes could no longer be assumed negligible. Devices were degassed at 300 mTorr and the fluid movement was monitored to compare the a) distance travelled by the fluid and b) flow velocity to the simulation. The model (solid line) predicts correctly for device thicknesses (2 mm) half of the perimeter width (4 mm). However, as the device thickness was increased to equal the perimeter width, diffusion from the side of the device was no longer negligible and the simulation deviated from experimental observation. For 3 and 4 mm thick devices, the simulation over-predicted fluid flow.

Device Fabrication

The PDMS devices employed to evaluate the simulation model were fabricated using standard soft lithography processes. A single layer mold was created using contact photolithography with SU-8 2100 (MicroChem Corp.) photoresist on a silicon wafer.

The channel dimensions were 88 μm high x 100 μm wide. Following hard bake, the mold was silanized with Trichloro(1H,1H,2H,2H-perfluorooctyl)silane (Sigma Aldrich). PDMS (Dow Corning Corp.) base and initiator were mixed in a 10:1 ratio, degassed, and poured onto the mold. The PDMS was then cured in a 65°C oven, removed from the mold, and the inlet holes were punched. The devices were bonded to a glass slide using Oxygen plasma (20W, 40 sec, 300 mTorr). The simulation parameters were adjusted accordingly to accurately represent the devices used for validation testing.

MATLAB Script of Model for Predicting Degas-driven Flow in a Microfluidic Device

```
%Model for Predicting Degas-driven flow in a Microfluidic Device
%Couples Diffusion of Gas in a Plane Sheet with Pressure-driven flow in a Rectangular Microchannel
%Non-Steady State, Internal Surface Concentrations Variable with Initial Distribution f(x)
%See Crank's Mathematics of Diffusion Text
%
%Written December 2011 by John R. Waldeisen, modified March 2012

close all;
clear all;
clc

nitrosol=0.168;
oxsol=0.168;
nitrodiff=8.514e-9;
oxdiff=8.514e-9;

solubility=oxsol*.22+nitrosol*0.78;
cchan=40.874; %the concentration in mol/m^3 of atmosphere
c1=solubility*40.874;
c2=solubility*40.874;

cvac=solubility*(0.000395*101325)/(8.3144621*298.15); %Concentration at 300mTorr (vacuum pump), PV=nRT

d=8.514e-9; %Weighted average of N2 and O2 diuffusion coefficients in PDMS
vactime=1800; %time that PDMS is in vacuum (30 min)
waittime=30; %time before fluid is loaded in seconds
endtime=300;
l=2.0e-3; %the length between the end of the channel and the surface of the PDMS in m
dl=1e-6; %micron increments across PDMS interface
x=[0:dl:l]; %creates x position
chanlen(1)=100e-2; %the length of the channel in m
side=100e-6; %channel width
chanvol=side.*side.*chanlen(1); %volume of channel in m
surfchan=chanlen(1).*side; %surface area of ceiling and floor of channel
dt=0.5; %the time step size for fluid flow
bigdt=1; %the big time step size for vacuum and wait times
a=2; %a will be used to incremement the location in the arrays
conc(1)=cchan.*chanvol;
p(1)=conc(1).*8.314462.*298.15./chanvol;
dx(1)=.006; %Width of droplet of fluid on device
u(1)=0; %Initial velocity of blood
vis=0.001; %Dynamic Viscosity in Pa-sec
aspect=1; %Aspect ratio of channel width to height (w/h)
surftension=0.0725; %Surface Tension of fluid (water) in N/m
contact=110; %Contact angle of fluid with polymer (PDMS is 110) in degrees
capillary=2*surftension*cos(contact*pi/180)*(1/side+1/side); %Capillary pressure
gamma=0.4217313774; %Gamma is correction factor for rectangular microchannel

%%%VACUUM TIME%%%  (Calculates initial conc. profile of degassed device before fluid loading)
% count=0;
% xvac=x-max(x)/2;
% lvac=l/2;
% for t=dt:bigdt:vactime;
```

```
%    term1=0;
%    count=count+1
%    for n=0:20
%       term1=term1+((-1)^n)/(2*n+1)*exp((-d*((2*n+1)^2)*(pi^2)*t)/(4*(lvac^2)))*cos(((2*n+1)*pi*xvac)/(2*lvac));
%    end
%    cpdms(count,:)=((cvac-co)*(1-(4/pi)*term1))+co;
% end
% co=ones(1,size(x,2));
% co(1,:)=cpdms(count,:);
co=cvac*ones(1,size(x,2));  %Input for completely degassed device
%%%END OF VAC TIME%%%

%%%IDLE TIME%%%  (Determines conc. profile in device after idle time)
count=0;
for t=dt:bigdt:waittime;
   term1=0;
   term2=0;
   count=count+1

   for n=1:20;
      term1=term1+((c2*cos(n*pi)-c1)/n)*sin(n*pi*x/l)*exp(-d*n^2*pi^2*(t)/(l^2));
      term2=term2+sin(n*pi*x/l)*exp ((-d*(pi^2)*(n^2)*(t))/(l^2))*trapz(x,(diag((co(a-1,:)')*sin((n*pi*x)/l))'));
   end
cwait(count,:)=c1+(c2-c1)*x/l+2/pi*term1+(2/l)*term2;
end
clear co;
co=ones(1,size(x,2));
co(1,:)=cwait(count,:);
%%%END OF WAIT TIME%%%

f(1)=-d*(co(1,2)-co(1,1))/dl;  %Flux for the first time point

%%%LOADING SECTION%%%
for t=dt:dt:endtime;
%Use Fick's 2nd Law
term1=0;
term2=0;

for n=1:20;
   term1=term1+((c2*cos(n*pi)-c1)/n)*sin(n*pi*x/l)*exp(-d*n^2*pi^2*(dt)/(l^2));
   term2=term2+sin(n*pi*x/l)*exp((-d*(pi^2)*(n^2)*(dt))/(l^2))*trapz(x,(diag((co(a-1,:)')*sin((n*pi*x)/l))'));
end

co(a,:)=c1+(c2-c1)*x/l+2/pi*term1+(2/l)*term2;

dc=co(a,2)-co(a,1);
dcdl=dc/dl; %Calculates forward derivative of concentration wrt length
f(a)=-d*dcdl;  %Determines flux out of the microchannel

%%%%%START WHILE EPS FUNCTION%%%%%  (Iterates until model converges upon a solution)
eps=1;
tempchanlen=chanlen(a-1);
dx(a)=dx(a-1);

while eps>0.0001
   conc(a)=cchan.*chanvol; %Channel concentration at PDMS boundary, in mols
   p(a)=conc(a).*8.314472.*298.15./chanvol; %Ideal gas law calculation of pressure, P=nRT/v

   if p(a)<3173
      p(a)=3173; %Channel pressure must be greater than vapor pressure of liquid (Water is 3173 kPa)
   end

   dp=p(1)-p(a);
   dpdx=dp/dx(a);
   curtime(1)=0;
   curtime(a)=t;

   instdp(1)=0;
   instdp(a)=p(a)-p(a-1);
```

```
   if (capillary+dp)<0 %Capillary pinning
   u(a)=0;
   else

u(a)=((surftension*cos(contact*pi/180)*(1+aspect)*side*gamma)/(6*vis*dx(a)))+((dp*side^2*gamma)/(12*vis*dx(a)))+((side^2*ga
mma*instdp(a))/(12*vis*dx(a))); %Equation 5
   end

   if u(a)<0
      u(a)=0;
   end

   travel=u(a)*dt;
   dx(a)=dx(a-1)+travel;
   chanlen(a)=chanlen(a-1)-(travel);
   chanvol=side.*side.*chanlen(a); %Volume of channel in m
   surfchan=1*chanlen(a).*side; %Surface area of ceiling (Multiply by 3 for monolithic PDMS device)
eps=abs((chanlen(a)-tempchanlen)./chanlen(a));
   tempchanlen=chanlen(a);
end

if chanlen(a)<0 && t>15
   endtime=t;
   disp('!!!Channel length < 0!!!')
   break
end

if u(a)==0 && t>60
   endtime=t;
   disp('!!!Fluid Flow Stopped: Degas Flow Exhausted!!!')
   break
end

disp(t), disp(p(a)), disp(dp), disp(instdp(a)), disp(chanlen(a)*100), disp(dx(a)*100) %Help debug

a=a+1;
conc(a)=conc(a-1)-(f(a-1).*surfchan.*dt);

if conc(a)<0;
   conc(a)=0;  %Pressure cannot be below zero
end

cchan=conc(a)/chanvol; %Do not need to multiply by RT as it would be divided in next line
c1=solubility*cchan; %New boundary condition which includes solubility of air in PDMS

end

%Figures Section
%
%Figure 1 will display the concentration of N2 and 02 within the PDMS during the wait time
%figure(1);
%plot(x,cpdms);
%xlabel('Distance from Channel Wall to Outer Polymer Surface (m)');
%ylabel('Concentration at Given Location (mol/m^3)');
%title('Concentration as a Function of Distance During Vacuum');
%saveas(gcf,'/Users/XXX/Desktop/Degas Flow Simulation/Results/Current/figure1.jpg');

%Figure 2 will display the concentration of N2 and 02 within the PDMS during the wait time
figure(2);
plot(x,cwait);
xlabel('Distance from Channel Wall to Outer Polymer Surface (m)');
ylabel('Concentration at Given Location (mol/m^3)');
title('Concentration as a Function of Distance During Wait');
saveas(gcf,'/Users/XXX/Desktop/Degas Flow Simulation/Results/Current/figure2.jpg');

%Figure 3 will display the concentration of N2 and O2 at the PDMS Interface and then through the PDMS
figure(3);
plot(x,co);
xlabel('Distance from Channel Wall to Outer Polymer Surface (m)');
ylabel('Concentration at Given Location (mol/m^3)');
```

```
title('Concentration as a Function of Distance During Loading');
saveas(gcf,'/Users/XXX/Desktop/Degas Flow Simulation/Results/Current/figure3.jpg');

%Figure 4 displays the flux at the PDMS channel interface as a function of time
ymin=min(f);
ymax=max(f);
time=0:dt:endtime;
figure(4);
plot(time,f);
xlabel('Time (seconds)');
ylabel('Flux at Channel Interface (mol/(s*m^2))');
title('Flux at Channel Interface as a Function of Time');
axis([0 endtime ymin ymax]);
saveas(gcf,'/Users/XXX/Desktop/Degas Flow Simulation/Results/Current/figure4.jpg');

%Figure 5 displays the pressure within the channel as a function of time
pmax=max(p);
pmin=min(p);
figure(5);
plot(time,p);
xlabel('Time (seconds)');
ylabel('Pressure within Channel (Pa)');
title('Pressure within Channel as a Function of Time');
axis([0 endtime pmin pmax]);
saveas(gcf,'/Users/XXX/Desktop/Degas Flow Simulation/Results/Current/figure5.jpg');

%Figure 6 displays the fluid velocity within the channel as a function of time
umax=max(u);
umin=min(u);
figure(6);
plot(time,u);
xlabel('Time (seconds)');
ylabel('Fluid Velocity (m/sec)');
title('Fluid Velocity as a Funtion of Time');
axis([0 endtime umin umax]);
saveas(gcf,'/Users/XXX/Desktop/Degas Flow Simulation/Results/Current/figure6.jpg');

%Figure 7 displays the fluid velocity within the channel as a function of position
dxmax=max(dx);
dxmin=min(dx);
figure(7);
plot(dx,u);
xlabel('Position (m)');
ylabel('Fluid Velocity (m/xec)');
title('Fluid Velocity as a Function of Position');
axis([0 dxmax umin umax]);
saveas(gcf,'/Users/XXX/Desktop/Degas Flow Simulation/Results/Current/figure7.jpg');

%Figure 8 displays the fluid interface position as a function of time
figure(8);
plot(time,dx);
xlabel('Time (sec)');
ylabel('Position (m)');
title('Fluid Interface Position as a Function of Time');
axis([0 endtime dxmin dxmax]);
saveas(gcf,'/Users/XXX/Desktop/Degas Flow Simulation/Results/Current/figure8.jpg');

dlmwrite('/Users/XXX/Desktop/Degas Flow Simulation/Results/Current/x.txt',x,'delimiter','\t');
%dlmwrite('/Users/XXX/Desktop/Degas Flow Simulation/Results/Current/cpdms.txt',cpdms,'delimiter','\t');
dlmwrite('/Users/XXX/Desktop/Degas Flow Simulation/Results/Current/cwait.txt',cwait,'delimiter','\t');
dlmwrite('/Users/XXX/Desktop/Degas Flow Simulation/Results/Current/co.txt',co,'delimiter','\t');
dlmwrite('/Users/XXX/Desktop/Degas Flow Simulation/Results/Current/time.txt',time,'delimiter','\t');
dlmwrite('/Users/XXX/Desktop/Degas Flow Simulation/Results/Current/f.txt',f,'delimiter','\t');
dlmwrite('/Users/XXX/Desktop/Degas Flow Simulation/Results/Current/p.txt',p,'delimiter','\t');
dlmwrite('/Users/XXX/Desktop/Degas Flow Simulation/Results/Current/u.txt',u,'delimiter','\t');
dlmwrite('/Users/XXX/Desktop/Degas Flow Simulation/Results/Current/dx.txt',dx,'delimiter','\t');
```

APPENDIX B: UNIVERSAL BLOOD SAMPLE PREPARATION DEVICE

Multi-laminate Device Fabrication

Multi-laminate devices were designed in AutoCAD 2012 with a single polyline representing a fluidic channel. Designs were converted to the color red and lines were configured to continuous line format with a width of 0.0001. The AutoCAD units were set to equal 1 mm and the file was plotted on the VersaLaser. The VersaLaser machining settings were configured to those depicted in Table B1. ARseal 90880 (150 μm) was used for the fluidic channel layer and was the most adhesive PSA from Adhesives Research.

Table B1: Laminated Device Material Machining Settings for VersaLaser

Material	Company	Thickness	Material Setting	Thickness Setting	Power Adjustment Setting
PSA	Adhesives Research	150 μm	Paper	0.6 mm	-20%
Silicone Elastomer	Stockwell Elastomerics	250 μm	Rubber Stamp	0.3 mm	0%
Silicone Elastomer	Stockwell Elastomerics	800 μm	Rubber Stamp	0.8 mm	0%

The bottom PCB substrate (Advanced Circuits) was cut with a band saw (G0621 Variable Speed Bandsaw Grizzly Industrial, Inc.) and PSA was assembled layer-by-layer by hand with tweezers. The middle silicone layer, typically 250 or 800 μm thick, was cut with the VersaLaser and cleaned with soap afterwards as the material ashes during cutting. A top hermetic seal layer, typically polyvinyl plastic, was used to prolong degassing lifetime. A KnK Blade Cutter was employed to cut this layer.

Table B2: Laminated Device Material Machining Settings for KnK Blade Cutter

Material	Company	Thickness	Force	Speed	Result
Polyvinyl Plastic	US Plastic Corp	250 μm (0.01")	125	50	Good cut
PTFE	US Plastic Corp	500 μm (0.02")	250 (Max)	50	Poor cut (could snap out small features)

Devices were typically inspected with a stereomicroscope (Olympus SZX7 Stereoscope or Keyence VHX-500F). Final devises were degassed in the Stanley Hall house vacuum or in a two-stage mechanical vacuum pump at 300 mTorr for a couple of hours and then vacuum packaged (Van der Stähl Scientific, Inc. Vaccum Packaging System or FoodSaver V2240).

Sample Preparation Device Design

To date, over 25 design versions of the sample preparation device exist and some are depicted in Fig. B1. Degassing chambers were originally designed to provide added surface area for enhanced degassing. However, channel vias were soon determined to

have a better surface area-to-volume ratio and a honeycomb arrangement can be seen in v17. Device with one, two, and three trench outlets were developed and v17 includes the nylon mesh filter that was determined to be less efficient.

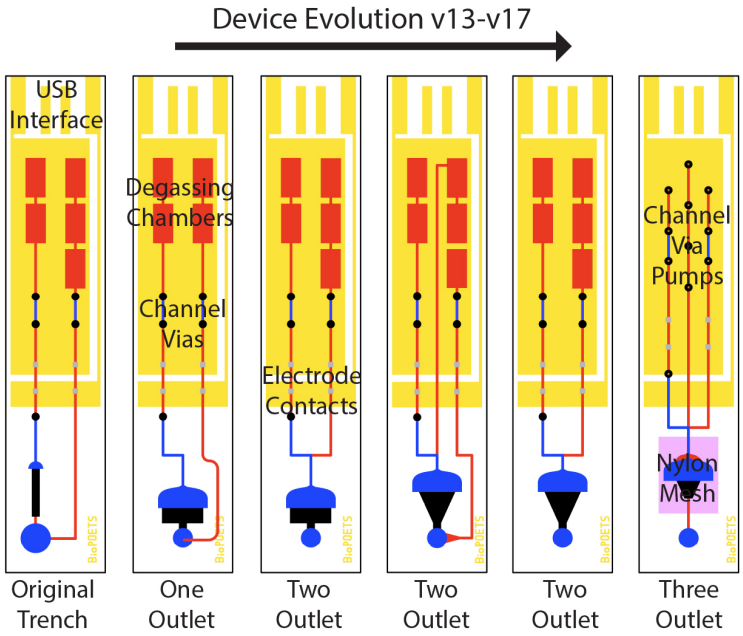

Figure B1: Example of the device evolution for the sample preparation module. Various trench and degassing pump geometries were assessed.

The fabrication of the new version of the sample preparation device is depicted in Fig. B2. This device is thinner as only six layers are used and an 800 µm silicone layer.

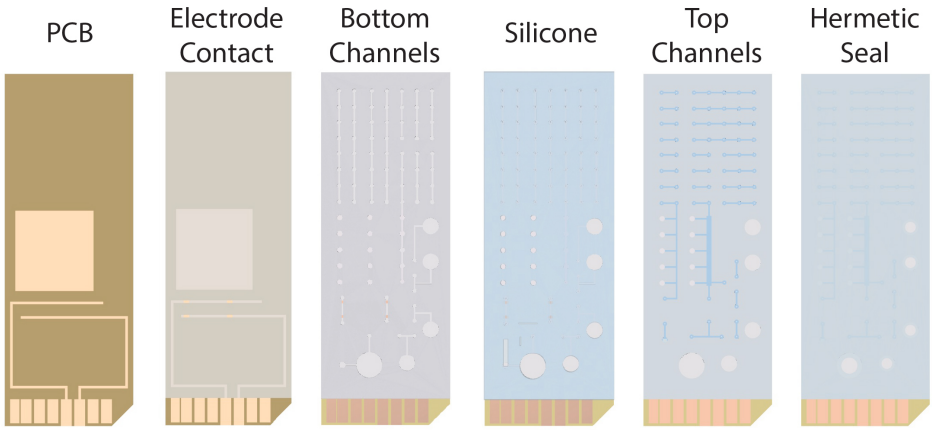

Figure B2: Fabrication of the SD-interface sample preparation device has only six layers and a thinner (800 µm) silicone layer. The bottom layer is thin copper electrodes on kapton (polyimide) film.

A schematic of utilizing the air gap at a channel junction between two fluids as a "timing valve." When the air dissolves into the porous silicone layer, the second fluid is "shorted" like an electrical circuit and loads into the channel displacing the first fluid.

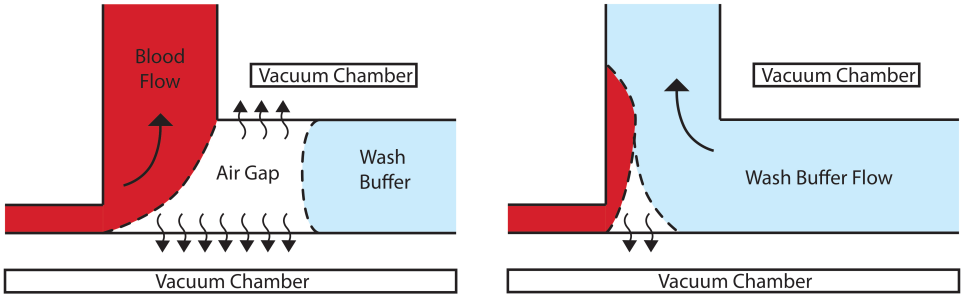

Figure B3: Illustration of the "timing valve" used in the sequential flow component of the sample preparation device. As two flows travel toward a junction, an air gap is created and one flow dominates. As the air gap dissolves into the porous silicone layer, the second fluid will effectively short and dominate flow in the channel as it temporarily has a larger pressure gradient.

BASIC Stamp Code for Programming Electrochemical Lysis Microcontroller

The screen shot of the BASIC Stamp II editor is shown in Fig. B3 allowing voltages range from 0 to 5.0V to be programed in 0.5V increments.

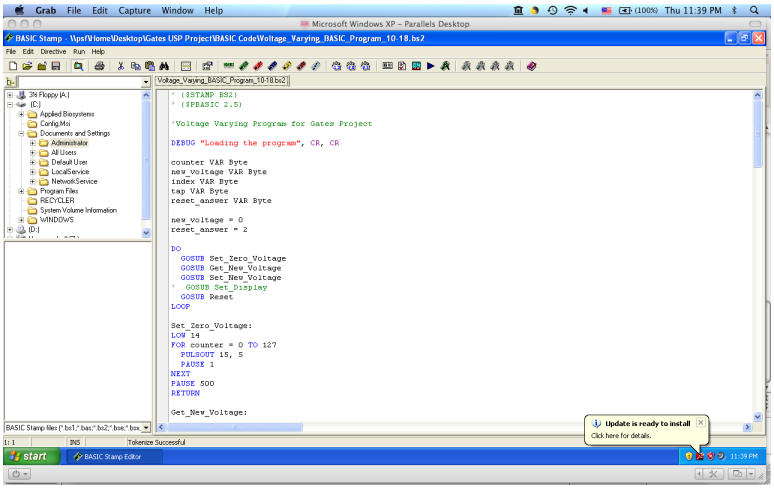

Figure B4: Screen shot of the BASIC Stamp editor used to program the portable electrochemical module.

```
' {$STAMP BS2}
' {$PBASIC 2.5}

'Voltage Varying Program for Gates Project

DEBUG "Loading the program", CR, CR

counter VAR Byte
new_voltage VAR Byte
index VAR Byte
tap VAR Byte
reset_answer VAR Byte

new_voltage = 0
reset_answer = 2

DO
  GOSUB Set_Zero_Voltage
```

```
  GOSUB Get_New_Voltage
  GOSUB Set_New_Voltage
  GOSUB Reset
LOOP

Set_Zero_Voltage:
LOW 14
FOR counter = 0 TO 127
  PULSOUT 15, 5
  PAUSE 1
NEXT
PAUSE 500
RETURN

Get_New_Voltage:

DEBUG "Voltage initialized to: ",
  DEC new_voltage, CR, CR
'DEBUG "Enter new voltage as index of the following:", CR, "0.5, 1, 1.5, 2, 2.5, 3, 3.5, 4, 4.5, or 4.84(max)", CR
DEBUG "Enter new voltage as index of the following:", CR,
"1   0.5V    6   3.0V", CR,
"2   1.0V    7   3.5V", CR,
"3   1.5V    8   4.0V", CR,
"4   2.0V    9   4.5V", CR,
"5   2.5V   10   4.8V", CR, CR
DEBUG "Input: "
DEBUGIN DEC new_voltage
PAUSE 500
RETURN

Set_New_Voltage:

LOOKDOWN new_voltage, [1, 2, 3, 4, 5, 6, 7, 8, 9, 10], index
LOOKUP index, [12, 25, 38, 51, 65, 77, 91, 104, 118, 127], tap
DEBUG "Voltage corresponds to ",
  DEC tap
DEBUG " taps.", CR, CR

HIGH 14
FOR counter = 0 TO tap
  PULSOUT 15, 5
  PAUSE 1
NEXT
PAUSE 1000
RETURN

Reset:

DEBUG "Reset USB voltage?", CR, "Yes: 1 or No: 2", CR, CR
DEBUG "Input: "
DEBUGIN DEC reset_answer
IF (reset_answer=2) THEN GOSUB LED_Blink
RETURN

LED_Blink:

DO
  HIGH 2
  PAUSE 500
  LOW 2
  PAUSE 500
LOOP
```

APPENDIX C: BLOOD COAGULATION CHIP FOR INR VALUE AND HEMATOCRIT DETERMINATION

Estimated Fabrication Cost of the Blood Coagulation Chip

A cost analysis was conducted to determine the average device cost for the production of 10 million blood coagulation chips. (Fig. C1)

Major Expense Areas	Type	Process/ details	Unit cost (USD)	Units needed	Vendor/ contractor	Model/process	Subtotal Cost	Cost per chip	Percentage of Total Cost
Injection Molding (polystyrene) for SIMBAS component	Outsourcing	Injection moulding of polystyrene microfluidic channels	$0.026/ part	10,000,000	Titoma Group (China)	Medical Parts Injection Molding	$258,491	$0.03	2.54%
	Material required	Polystyrene	$2.2/kg	37,818 kg	Nanjing Rising Chemical Industry Co (China)	Polystyrene	$83,199	$0.01	0.82%
	Material required	PDMS	$1442.94 per kit (19.9 Kg)	2,513 kits (50,008 Kg total)	Dow Corning (Shanghai branch)	184 SIL ELAST KIT 19.9KG	$3,626,108	$0.36	35.57%
Biochemical Reagents	Materials Rquired	Bovine Lung Thromboplastin	$1500/100mL	100,000mL (10uL per chip)	BioPharma Laboratories, LLC	Derived from US sourced animals	$1,500,000	$0.150	14.72%
	Materials Rquired	Heparin sodium salt	$720/100mL	100,000mL (10uL per chip)	Sigma-Aldrich	Derived from porcine intestinal mucosa	$720,000	$0.072	7.06%
Bonding and vacuum packaging	Outsourcing	Bonding polystyrene microfluidic channels to PDMS	$0.1/ assay	10000000 bondings	Titoma Group (China)	thermal bonding	$1,000,000	$0.10	9.81%
	Outsourcing	Die cutting	$0.1/ assay	10000000 dies	Taiwan Glass Industry Corp (Taiwan)	die cutting	$1,000,000	$0.10	9.81%
	Out sourcing	Vacuum packaging	$0.1/ assay	10000000 packages	Vanderstahl Inc (USA)	medical packaging	$1,000,000	$0.10	9.81%
Manpower	CEO	Manage Operation	$130k/year	1 person (1year)	(USA)		$130,000	$0.01	1.28%
	Design and Process Engineers	Perfrom quality checks on sublease manufacturers	$100K/year	5 persons (1year)	(USA)		$500,000	$0.05	4.91%
	IP Consultant	IP/Law consultant	$100K/year	1person	(USA)		$100,000	$0.01	0.98%
	Accountant	Administrative Work	$100K/year	1 person (1year)	(USA)		$100,000	$0.01	0.98%
Rent and Utilities	Space required	Office Space (200 square metters)	$3500/month	12 months	SF Bay Area		$42,000	$0.00	0.41%
	Utilities	Electricity/ Phone/ Internet/ Water	$1,000	12 months			$12,000	$0.00	0.12%
	Office Supplies	Computers/ Printers/ Hardware		12 months			$50,000	$0.01	0.49%
Transportation fees	Transportation of Components	International shipping for global chain manufacturing	$270/ 30kg airmail	1284kg			$11,559	$0.00	0.11%
	Staff transportation	Flights for staff to factory for initial set-up	$2000/ trip	30 trips			$60,000	$0.01	0.59%
						Subtotal	10,193,357.46		
						Estimated cost for single Chip	$1.02		

Shipping costs determined for transfer between China/ UK/ Germany/ USA/ Taiwan during manufacturing. Rates based on USPS First Class	Assume bonding/ dicing/ packaging process is equal to five 2N3415 transistor fabrication costs. (2N3415 0.5A 0.5 Amp 25V NPN Transistor dimension= 4.5mm x 4.5mm x 4mm, one unit= 0.06 USD)

Figure C1: Average device cost for the fabrication of 10 million blood coagulation chips.

APPENDIX D: HYBRID LATERAL FLOW ASSAY TO MONITOR TUBERCULOSIS PATIENT RESPONSE

BSA Blocking Buffer

Blocking of the nitrocellulose membranes with Bovine Serum Albumin (BSA) was found to greatly improve post-adsorption latex bead and AuNP migration. The following is an adaptation of a previously published recipe:[1] Nitrocellulose membranes (Millipore Hi-Flow Plus HF240) were blocked with a solution of 20mM PBS (1x) containing 2% BSA (US Biological; Low fatty acid, low endotoxin, low IgG), 2.5% sucrose (Sigma), 0.3% polyvinylpyrrolidone (Sigma), and 0.02% sodium azide (Sigma). The blocking buffer was adjusted to a pH of 7.4. The test strips were soaked for at least 5 min and dried in an oven at 37°C. This drying method deviates from industry standard, which is typically performed in a humid oven to minimize protein denaturation. Room temperature/air drying of the blocked nitrocellulose membranes was determined to yield decreased release of detection particles post-adsorption to the nitrocellulose membrane. Additionally, particle migration was maximized when the BSA used in the blocking buffer was less than 3 months old. The lifespan of the blocking buffer is less than 3 months.

Correlation between Cavitary Pulmonary Tuberculosis and Anti-phospholipid IgM

Evaluation of anti-phospholipid IgM levels in patients with cavitary pulmonary tuberculosis was performed in Sao Paulo, Brazil at the Universidade Federal do Rio de Janeiro by Dr. Seung-min Park. Preliminary results (n=20) indicate a possible correlation between cavity number and anti-cardiolipin IgM level. (Fig. D1) Further evaluation of the this hypothesis is needed.

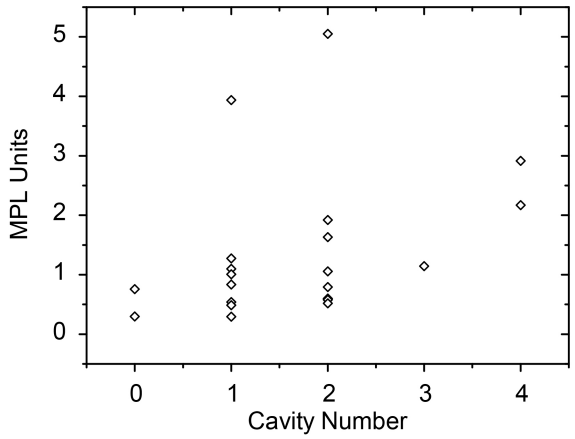

Figure D1: Preliminary ELISA tests suggest that anti-cardiolipin IgM levels correlate with the number of cavities patients have when suffering from cavitary pulmonary tuberculosis (unpublished data).

Preliminary Hybrid LFA Testing

Initial hybrid LFA device testing was performed with sheep blood, which was later determined to sediment at a much slower rate than human blood. Retesting of the device with human blood is pending. The device was created from multi-laminate fabrication as described previously in Chapter 5.

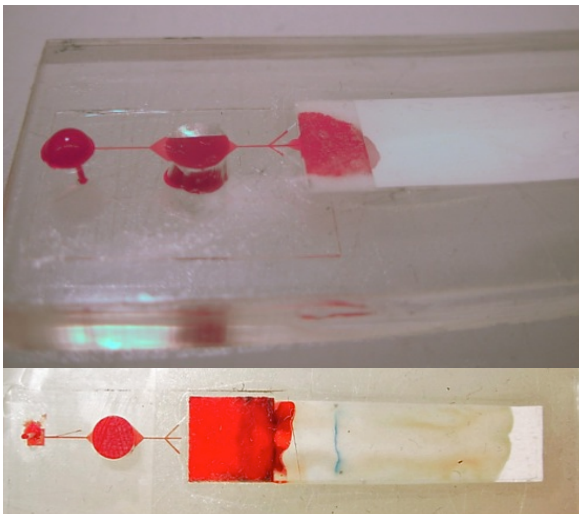

Figure D2: Preliminary Hybrid LFA device testing with sheep blood, which has a slower sedimentation rate than human blood.

APPENDIX E: A CORE-SATELLITE NANOASSEMBLED SUBSTRATE FOR COLORIMETRIC BIOMOLECULAR DETECTION

Core-Satellite Nanoassembled Substrate Fabrication

Droplet immobilizers were prepared by cutting 1 in. x 1 in. squares of cured, 4 mm thick PDMS (Dow Corning) and punching a 20 mm circle through the center. One droplet immobilizer was placed in the middle of a 1 in. x 3 in. 3-aminopropyltriethoxysilane (APTES) treated microscope slide (The Microscope Store). The slides were cleaned with a stream of nitrogen and immediately placed in a Petri dish. The surface adhesion of the PDMS to the APTES treated slide prevented liquid leakage and capillary remodeling due to surface dehydration. Gold colloid (800 μL, British Biocell International) at stock concentration was pipetted into the PDMS well and incubated at 4°C for 18 hrs. The wells were then washed multiple times with DI water (Milli-Q). A 50 μg/mL solution of the biotinylated peptide, biotin-GGRGDGKGGC-OH (Chi Scientific), in 1x PBS buffer (Gibco, Invitrogen) was prepared. The peptide solution was pipetted (800 μL) into the PDMS well and incubated at 4°C for 18 hrs. The wells were again washed with DI water. A 2 mM mPEG-SVA (M_W = 2kDa, Laysan Bio) solution was prepared in 100 mM $NaHCO_3$ (pH 8.25, Sigma-Aldrich) and sonicated briefly.[2] The mPEG-SVA solution was then pipetted (800 μL) into the PDMS well and incubated at room temperature (25°C) for 6 hrs. The wells were again washed with DI water. Finally, streptavidin conjugated AuNPs were pipetted (800 μL) into the well and incubated at 4°C for 12 hrs. The slides were then washed with DI water and stored at 4°C before exposure to 0.25% Trypsin-EDTA 1x (Gibco, Invitrogen).

Streptavidin Conjugation onto the Gold Nanoparticles

A modified version of a previous protocol was used.[3] A sodium borax buffer was prepared by titrating 10 mL of 200 mM H_3BO_3 (pH 5.4, Sigma-Aldrich) with 2 mM $Na_2B_4O_7$ (pH 8.9, Sigma-Aldrich) to a final pH 7.1 (~18 mL of 2 mm $Na_2B_4O_7$ was added). The pH of the buffer is essential as it must be above the isoelectric point of streptavidin (pI ≈ 5.0) such that streptavidin can displace the negatively charged citrate groups adsorbed on the surface the AuNPs, but not too high of a pH as excess salt ions from $Na_2B_4O_7$ will induce flocculation. 1 mL of 10 nm, 30 nm, and 50 nm AuNPs (stock concentration) were spun down at 14,000, 10,000, and 7,000 RPM for 10, 8, and 5 min, respectively. The supernatant was discarded and the particles were resuspended in an equal volume (1 mL) of 5 μg/mL streptavidin (SouthernBiotech) in the sodium borax buffer. The suspension was placed on a rocker for 15 min to allow physio-adsorption. The streptavidin conjugated AuNPs were spun down again and the supernatant was discard. The conjugated AuNPs were resuspended in DI water. A 1% w/v NaCl (Sigma-Aldrich) test was performed to ensure streptavidin conjugation. Conjugated AuNPs can withstand salt concentrations up to 2-3% before crashing out of solution, observed by the flocculation of the solution (turns blue) or sedimentation of a black speck to the bottom of the reaction vessel.

Dark Field Spectroscopy

The nanoassemblies were imaged in dark field with an inverted microscope (Carl Zeiss Axiovert 200) under illumination from a Xenon light source (Karl Storz). The scattered light was collected by a 20x microscope objective (Carl Zeiss, LD Achroplan) with a numerical aperture (NA = 0.40) smaller than that of the Nikon DF dry condenser lens (NA = 0.80 - 0.95). The spectra were acquired with a Princeton Instruments Acton SP2300 using WinSpec and images were taken with a true-color CCD (QImaging Micropublisher 3.3 RTV). All measurements were taken with the nanoassemblies immersed in DI water and at room temperature (25°C).

Scattering Properties of Gold Nanoparticles

The peak position and the FWHM for the four AuNPs core sizes was investigated. (Figure E1 and Table 6.1) Core sizes of 30 nm and 50 nm scattered green, whereas the 80 nm and 100 nm sizes appeared chartreuse and minimal redshift was observed upon satellite attachment. 50 nm core particles are optimal for the substrate as they have a larger scattering radius than the 30 nm core particles, which appeared very dim. Rayleigh and Mie theory are presented in Chapter 6 to describe the scattering properties of gold nanoparticles.

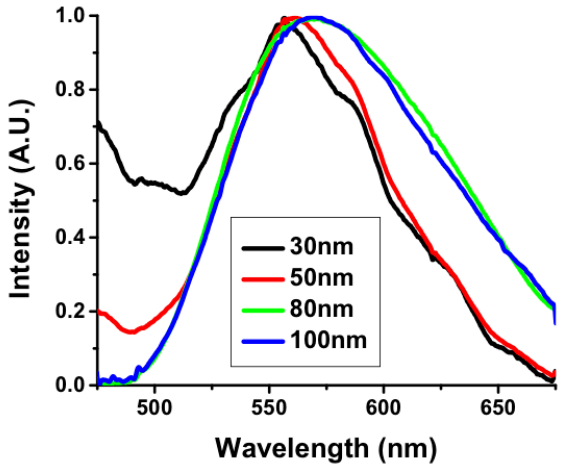

Figure E1: Average of n=10 scattering spectra taken for each of the core AuNPs before satellite attachment. The spectra were used to determine peak position and FWHM in Table 6.1.

Figure E2a demonstrates Rayleigh scattering in colloidal nanoparticles suspensions with different diameters. The scattering cross-section is related to the wavelength and radius of the nanoparticle by: $\sigma_s \propto r^6/\lambda^4$. Thus smaller nanoparticles (50 nm) have smaller scattering cross-sections and appear dim when imaged in DF, but selectively scatter blue light (short wavelengths) more than red light (longer

wavelengths). Larger nanoparticles (100 nm) scatter both red and blue wavelengths, thus appearing translucent. The scattering cross-section is simulated in Figure E2b using Rayleigh theory, which is valid when $r \leq 0.1\lambda$.

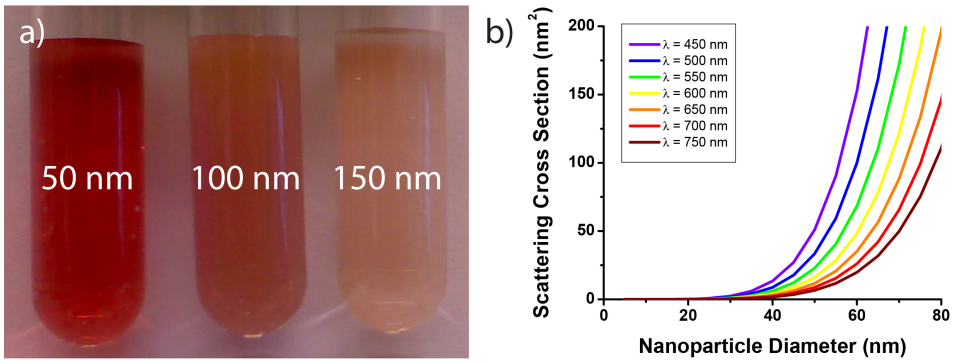

Figure E2: a) Visual scattering properties of colloidal nanoparticle suspensions. Particles with smaller diameters scatter only short (blue) wavelengths, whereas larger diameters scatter both short (blue) and long (red) wavelengths. b) Rayleigh simulation of nanoparticle scattering cross-section. This solution is only valid when $r \leq 0.1\lambda$.

The emitted spectrum for the Xenon light source (Karl Storz) used for illumination in during DF microscopy of the nanoassembled substrate.

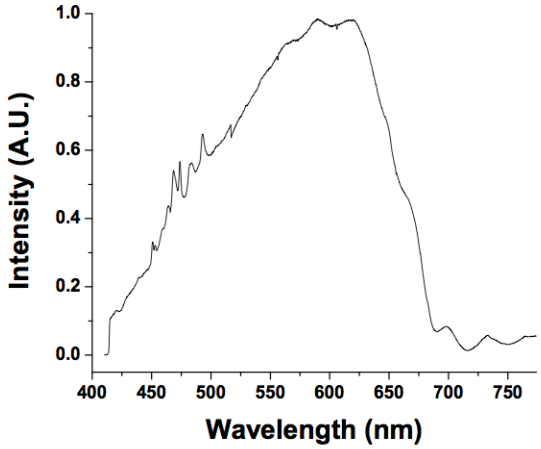

Figure E3: Emitted spectrum from the Xenon light source.

Optical Properties of Core-Satellite Assembly and Disassembly

Qualitative heat maps for both the peak shift and change in FWHM upon assembly and disassembly are shown in Figures E4 and E5. The largest changes came from core-satellite combinations of 30 and 50 nm gold nanoparticles. Two slides were fabricated for each geometrical variation and random, quintuplicate DF measurements were acquired per slide. A MATLAB script was used to normalize and identify spectral peak position and FHWM of the measurements.

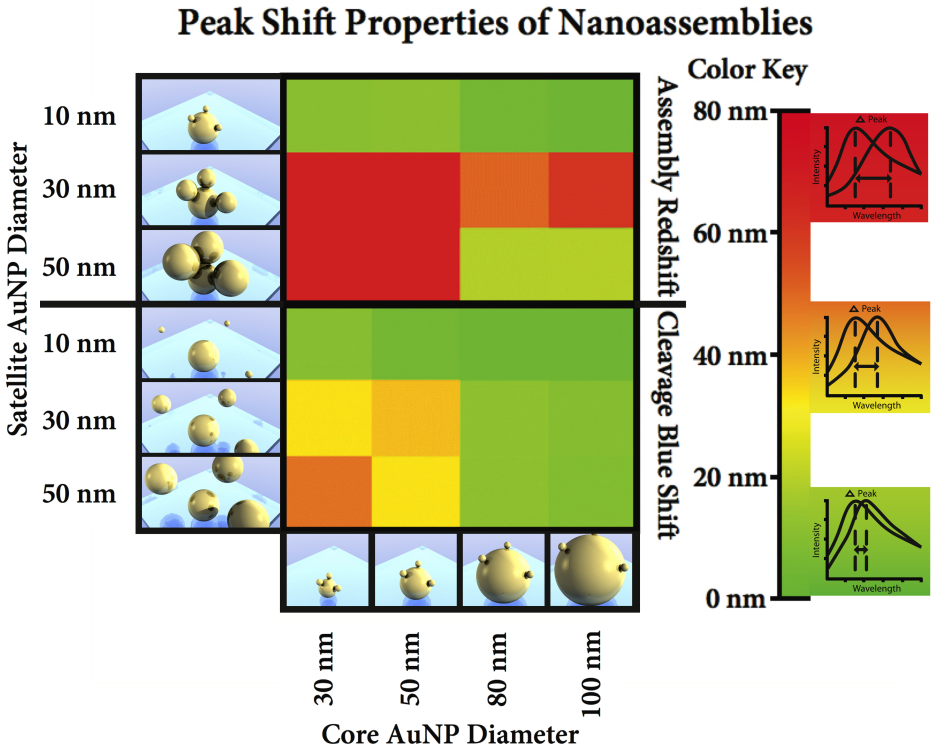

Figure E4: Large-scale characterization study of the DF peak shift properties for a combination of core and satellite diameters. Assembly redshift (top) and disassembly blue shift (bottom) are depicted.

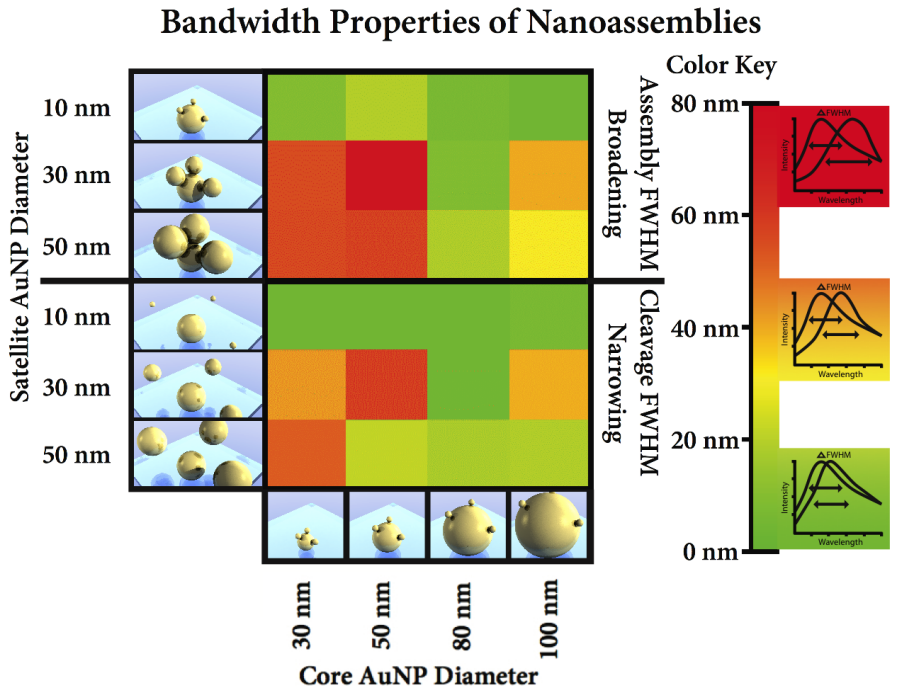

Figure E5: Large-scale characterization study of the FWHM properties for a combination of core and satellite diameters. Assembly FWHM broadening (top) and disassembly FWHM narrowing (bottom) are depicted.

Sample Standard Deviations for Experimental Data

The sample standard deviations for peak and FWHM measurements are presented in Tables E1 and E2. The calculated deviation is comparatively small given that both had fluctuations as large as 80 nm. Two slides were fabricated for each geometrical variation and random, quintuplicate measurements were acquired per slide.

Table E1: Sample Standard Deviation of Peak Shift Measurements

		Core AuNP Diameter				
		30 nm	**50 nm**	**80 nm**	**100 nm**	
Satellite AuNP Diameter	**10 nm**	1.7	0.8	3.5	3.4	Core Deposition (nm)
	30 nm	0.7	1.5	2.6	1.0	
	50 nm	1.8	1.8	7.4	1.5	
	10 nm	5.0	4.3	4.0	4.2	Satellite Attachment (nm)
	30 nm	2.4	5.7	3.8	5.0	
	50 nm	3.4	4.1	6.9	12.7	
	10 nm	2.8	2.9	6.6	1.5	Satellite Release (nm)
	30 nm	4.2	5.3	2.4	3.6	
	50 nm	2.9	4.0	3.8	2.1	

Table E2: Sample Standard Deviation of FWHM Measurements

		Core AuNP Diameter				
		30 nm	**50 nm**	**80 nm**	**100 nm**	
Satellite AuNP Diameter	**10 nm**	13.6	12.6	5.4	3.3	Core Deposition (nm)
	30 nm	6.2	11.7	5.0	2.6	
	50 nm	13.4	3.5	10.5	3.4	
	10 nm	24.1	15.5	4.7	2.7	Satellite Attachment (nm)
	30 nm	10.6	8.0	7.0	15.9	
	50 nm	14.2	7.7	8.3	11.1	
	10 nm	18.4	14.3	6.0	4.0	Satellite Release (nm)
	30 nm	3.4	6.4	3.2	5.5	
	50 nm	4.7	12.2	4.3	4.1	

Integration of the Nanoassembled Substrate for Microfluidic Point-of-care Diagnostics

Figure E6 depicts an example of a PDMS microfluidic device bonded onto the nanoassembled core-satellite substrate. Traditional soft-lithography techniques were employed to create the microfluidic device with channels 150 μm wide and 50 μm high. The PDMS device was oxygen plasma treated and irreversibly bonded to the substrate.

The empty microchannels and the assembled core-satellite AuNP substrate appear as the wider, vertical yellow lines.

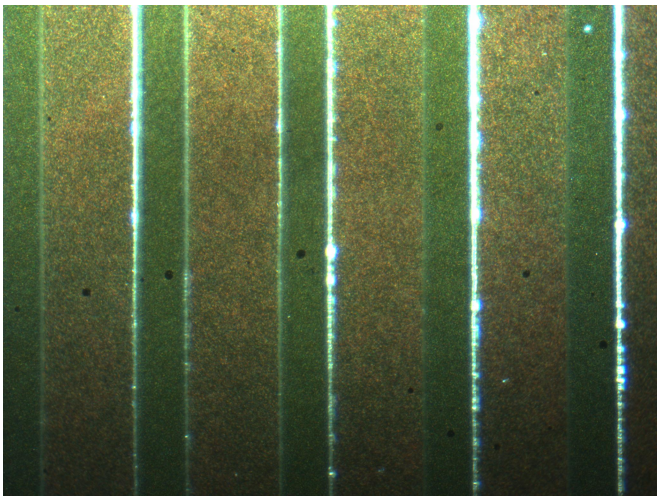

Figure E6: An example of a PDMS microfluidic device bonded onto a AuNP core-satellite substrate. The yellow scattered channels are regions where the core-satellites are assembled.

Characterization of the gold nanoparticles is presented in Table E3, as obtained from the supplier (British Biocell International).

Physical Properties of the Gold Nanoparticles

Table E3: Fabrication Data for Gold Nanoparticles

AuNP Size (nm)	Mean Diameter (nm)	Concentration (particles/mL)	Coefficient of Variation (%)
30	31.1	2.0×10^{11}	< 8
50	49.3	4.5×10^{10}	< 8
80	78.8	1.1×10^{10}	< 8
100	100.4	5.6×10^{9}	< 8

MATLAB Script for the Determination of Peak Position and FWHM

MATLAB scripts were written to normalize and analyze the collected spectral data. Particle density analysis was achieved by employing a particle counting MATLAB script to analyze SEM images taken of the AuNP cores.

```
%Clear all previous screens
close all
clear all
clc

[filenameLS, pathnameLS] = uigetfile('*.txt','Select Background Lightsource','/Users/ Desktop/');
infoLS = dlmread([pathnameLS filenameLS]);
[rowsizeLS colsizeLS] = size(infoLS);

[filenameFF, pathnameFF] = uigetfile('*.txt','Select Flatfield','/Users/Desktop/');
```

```
infoFF = dlmread([pathnameFF filenameFF]);
[rowsizeFF colsizeFF] = size(infoFF);

%Open ASCII-delimited spectra data
[filename, pathname, filterindex] = uigetfile({'*.txt'},'Select Spectra to Analyze','/Users/Desktop/','MultiSelect','on');
numfiles = max(size(filename));

result = ones([numfiles 3]);

for iter = 1:1:numfiles

   filename(iter)
   info = dlmread([pathname char(filename(iter))]);
   [rowsize colsize] = size(info);
   normdata = (info(1:rowsize,colsize)-infoFF(1:rowsizeFF,colsizeFF))./(infoLS(1:rowsize,colsize)-infoFF(1:rowsizeFF,colsizeFF));

   fig = figure;
   hold on;
   smoothdata = smooth(normdata(1:rowsize));
   smoothplot = plot(info(1:rowsize,1), smoothdata(1:rowsize),'Color', 'r','LineWidth',2);
   rawdata = plot(info(1:rowsize,1), normdata(1:rowsize));

   %[maxyaxis,maxI] = max(smoothdata(300:900));
   [maxyaxis,maxI] = max(smoothdata(300:900));

   maxI = maxI + 299;
%    [minyaxis,minI] = min(smoothdata(147:977));
   [minyaxis,minI] = min(smoothdata(54:977));
   minI = minI + 146;
   ylim([minyaxis maxyaxis]);
   xlim([info(1,1) info(rowsize,1)]);

   halfmax = ((maxyaxis - minyaxis)./2) + minyaxis;
   refline(0,halfmax);

%    [localmin, locminI] = min(smoothdata(237:400));
   [localmin, locminI] = min(smoothdata(30:400));
%    locminI = locminI + 236;
   locminI = locminI + 29;

   xlabel('Wavelength (nm)');
   ylabel('Semi-Normalized Intenisty');

   %Search for intersects with halfmax
   for itera = locminI:1:977
      if (smoothdata(itera) < halfmax && smoothdata(itera + 1) > halfmax) | (smoothdata(itera) > halfmax && smoothdata(itera + 1) <
halfmax)
         itera;
         wavelength = info(itera,1)
         intensity = smoothdata(itera);

         ref(1:rowsize,1) = wavelength;
         for iteration = 1:1:rowsize
            ref(iteration,2) = iteration./rowsize;
         end

         refplot = plot(ref(1:rowsize,1), ref(1:rowsize,2),'Color','g','Linewidth',2);

        %Fill in results matrix; elseif prevents excess right intersect points written to matrix
         if result(iter,1) == 1;
            result(iter,1) = wavelength;
         elseif result(iter,2) < 500
            result(iter,2) = wavelength;
         end
      end
   end

   %If leftside spectrum does not intersect halfmax, applies linear extrapolation
   if result(iter,1) > 600;
      i1 = 255
```

```
        i2 = 310
%       i1 = 439;
%       i2 = 476;
        result(iter,2) = result(iter,1);
        slopedif = smoothdata(i2) - smoothdata(i1);
        slopeleft = slopedif./(info(i2) - info(i1));
        distleft = (smoothdata(i2) - halfmax)./slopeleft;
        actwavelengthleft = info(i2) - distleft;
        result(iter,1) = actwavelengthleft;
        actrefleft(1:rowsize,1) = actwavelengthleft;

        for actiteration = 1:1:rowsize;
            actrefleft(actiteration,2) = actiteration./rowsize;
        end

        actrefplotleft = plot(actrefleft(1:rowsize,1), actrefleft(1:rowsize,2),'Color','g','Linewidth',2);
        plot([actwavelengthleft info(i2)],[halfmax smoothdata(i2)],'Color','y','Linewidth',2);
    end

%If rightside spectrum does not intersect halfmax before LS fluctuations, applies linear extrapolation
    if result(iter,2) > info(970) | result(iter,2) ==1;
        slopediff = smoothdata(958) - smoothdata(939);
        slope = slopediff./(info(958)-info(939));
        dist = (smoothdata(958) - halfmax)./-slope;
        actwavelength = dist + info(958);
        result(iter,2) = actwavelength;
        actref(1:rowsize,1) = actwavelength;

        for actiteration = 1:1:rowsize;
            actref(actiteration,2) = actiteration./rowsize;
        end

        actrefplot = plot(actref(1:rowsize,1), actref(1:rowsize,2),'Color','g','Linewidth',2);
        plot([info(958) actwavelength],[smoothdata(958) halfmax],'Color','y','Linewidth',2);
        xlim([info(1,1) (actwavelength + 10)]);
    end

    result(iter,3) = result(iter,2)-result(iter,1);
end

%Result is matrix of left, right intercepts, and FWHM
result
FWHM = sum(result(1:5,3))./5
SD = std(result(:,3),1)
%SD1 = sqrt(sum((result(:,3) - FWHM).^2)./numfiles)
```

MATLAB Script for the Determination of Core Density from SEM Images

```
clear all
close all
clc

[filename, pathname] = uigetfile('*.tif','Select SEM Image','/Users/Waldie/Desktop/MMP GNP Detection Data/SEM/');
I = imread([pathname filename]);

figure
imshow(I)

figure
BW = im2bw(I);
imshow(BW)

hold on
[L,num] = bwlabel(BW)
area = regionprops(L,'Area')

count = 0
```

```
for iter = 1:num
   if area(iter).Area > 25
      count = count +1
   end
end


for row = 1:512
   for col = 1:512
      if L(row, col) > 0 & area(L(row,col)).Area > 25
         plot(col, row)
      end
   end
end
```

APPENDIX F: A REAL-TIME PCR ANTIBIOGRAM FOR DRUG-RESISTANT SEPSIS

Preanalytic Removal of Heme and Human DNA Protocol

Defibrinated sheep blood (Hemostat Laboratories) was spiked with serial dilutions of bacteria and plated onto LB-Agar (Fisher Scientific) plates to determine initial bacteria concentrations in CFU/mL. Susceptible bacteria: Escherichia coli (ATCC No. 53338), Pseudomonas fluorescens (ATCC No. 13525), Proteus vulgaris (ATCC No. 33420), Micrococcus luteus (ATCC No. 49732), and Streptococcus lactis (ATCC No. 11454) (Fisher Scientific), and resistant E. coli (donated by J. Christopher Anderson Laboratory) were spiked into blood at concentrations ranging between 50-200 CFU/mL. 1 mL of spiked blood was added to 9 mL of LB Broth (Fisher Scientific, Miller) and grown in a shaker at 37°C in the presence of kanamycin, spectinomycin, or chloramphenicol (Sigma-Aldrich). The blood/LB mixture was then fractionated with a Beckman Coulter Allegra X-22R centrifuge for 10 min at 1500 rpm (524 g). This important step enables the removal of the PCR inhibiting Heme from the sample. 9.5 mL of supernatant, which consisted of bacteria, white blood cells, platelets, and serum, was collected and pelleted down for 10 min at 4500 rpm (4713 g). The supernatant (~9 mL), which contained serum and platelets, was decanted and the remaining pellet was resuspended. 125 μL of RIPA buffer (Thermo Scientific) was added to lyse the mammalian cells, the solution was vortexed, and incubated at 25°C for 5 min. 20 μL of DNase 10x reaction buffer and 20 μL (1 U/μg) of DNase (Fisher Scientific) were added to remove human background DNA. The sample was vortexed and incubated at 37°C for 30 minutes. 20 μL of DNase stop solution was then added to inhibit the reaction. The bacterial cells were then pelleted from the lysate for 10 min at 4500 rpm (4713 g). It is important to note that no actual pellet was visible after centrifugation as the bacterial cell volume was inappreciable. The supernatant (~600 μL) was decanted and the pellet was washed with 0.5 mL of reticulocyte saline (RS) buffer with 25 mM EDTA (4500 rpm, 5 min). A second wash was performed with 0.5 mL of RS buffer (4500 rpm, 5 min). The sample was resuspended in 25 μL of RS buffer and sonicated for 1 min before use as template for real-time PCR. Results obtained by the real-time PCR antibiogram were verified by culture in LB broth and on LB-agar plates with antibiotic discs. Antibiotic discs were created by cutting circular pieces of Whatman filter paper and soaking each in an antibiotic. (Table F1)

Reticulocyte Saline Buffer

A solution consisting of 130 mM NaCl, 7.4 mM $MgCl_2$, and 5 mM KCl was buffered to a pH of 7.35 with 10 mM Na-HEPES.

Antibiotic 1x Concentrations

The 1x antibiotic concentrations used for the purposes of this investigation were as follows: chloramphenicol: 25 μg/mL in ethanol, kanamycin: 25 μg/mL in DI water, and spectinomycin: 50 μg/mL in water.

Real-time PCR

Colony PCR was performed with a Bio-Rad iQ5 Real-time PCR Detection System and Stratagene Brilliant SYBR Green qPCR Core Kit. The 16S rRNA gene primers (Invitrogen) used are shown in Table 7.1 and a 58°C melting temperature was determined optimal for annealing. In accordance with the Stratagene Manual, 2 μL of template was used, taken directly from the prepared protocol described above.

Table F1: Verification of real-time PCR antibiogram

			Time to Visual (Hours)					
			0	**12**	**24**	**36**	**48**	**60**
Susceptible E. coli	LB Broth	Spect.	-	-	-	-	-	-
		Chlor.	-	-	-	-	-	-
		Kan.	-	-	-	-	-	-
		Untreat	-	-	-	X	X	X
		Neg.	-	-	-	-	-	-
	Antibiotic Discs	Spect.	-	-	-	-	-	-
		Chlor.	-	-	-	-	-	-
		Kan.	-	-	-	-	-	-
		Untreat	-	-	-	-	-	X
		Neg.	-	-	-	-	-	-
Spectinomycin Resistant	LB Broth	Spect.	-	-	-	X	X	X
		Chlor.	-	-	-	-	-	-
		Kan.	-	-	-	-	-	-
		Untreat	-	-	-	X	X	X
		Neg.	-	-	-	-	-	-
	Antibiotic Discs	Spect.	-	-	-	-	-	X
		Chlor.	-	-	-	-	-	-
		Kan.	-	-	-	-	-	-
		Untreat	-	-	-	-	-	X
		Neg.	-	-	-	-	-	-
Kanamycin Resistant	LB Broth	Spect.	-	-	-	-	-	-
		Chlor.	-	-	-	-	-	-
		Kan.	-	-	-	X	X	X
		Untreat	-	-	-	X	X	X
		Neg.	-	-	-	-	-	-
	Antibiotic Discs	Spect.	-	-	-	-	-	-
		Chlor.	-	-	-	-	-	-
		Kan.	-	-	-	-	-	X
		Untreat	-	-	-	-	-	X
		Neg.	-	-	-	-	-	-
MIC Determination	Microdilution in LB Broth	10x Spect.	-	-	-	-	-	-
		1x Spect.	-	-	-	-	-	-
		1/10x Spect.	-	-	-	-	-	X
		1/100x Spect.	-	-	-	X	X	X
		Untreat	-	-	-	X	X	X
		Neg.	-	-	-	-	-	-
	Antibiotic Discs	10x Spect.	-	-	-	-	-	-
		1x Spect.	-	-	-	-	-	-
		1/10x Spect.	-	-	-	-	-	-
		1/100x Spect.	-	-	-	-	-	X
		Untreat	-	-	-	-	-	X
		Neg.	-	-	-	-	-	-

Comparison of spectinomycin ΔC_t values between susceptible and spectinomycin resistant E. coli in Figure 2D and 2E:

A Gaussian ratio distribution was performed between the spectinomycin and negative ΔC_t values in both Figures 2D (susceptible) and 2E (spectinomycin resistant). The distributions are assumed to be normal and not correlated. Since the ΔC_t values both have a non-zero mean, the Hinkley distribution was utilized where the probability density function of the ratio between two normal variables (Z=X/Y) is given by:[4]

$$P(z)=\frac{b(z)\cdot c(z)}{a^3(z)}\frac{1}{\sigma_X\sigma_Y\sqrt{2\pi}}\left[2\Phi\left(\frac{b(z)}{a(z)}\right)-1\right]+\frac{1}{\pi\sigma_X\sigma_Y a^2(z)}e^{-\frac{1}{2}\left(\frac{\mu_X^2}{\sigma_X^2}+\frac{\mu_Y^2}{\sigma_Y^2}\right)} \tag{F.1}$$

where

$$a(z)=\sqrt{\frac{1}{\sigma_X^2}z^2+\frac{1}{\sigma_Y^2}} \tag{F.2}$$

$$b(z)=\frac{\mu_X}{\sigma_X^2}z+\frac{\mu_Y}{\sigma_Y^2} \tag{F.3}$$

$$c(z)=e^{\frac{1}{2}\frac{b^2(z)}{a^2(z)}-\frac{1}{2}\left(\frac{\mu_X^2}{\sigma_X^2}+\frac{\mu_Y^2}{\sigma_Y^2}\right)} \tag{F.4}$$

$$\Phi(z)=\int_{-\infty}^{z}\frac{1}{\sqrt{2\pi}}e^{-\frac{1}{2}u^2}du=\frac{1}{2}\mathrm{erfc}\left(-\frac{z}{\sqrt{2}}\right) \tag{F.5}$$

Figure F1 depicts the probability density functions for the comparison of Figures 7.3c and 7.3d. A two-sample Kolmogorov-Smirnov test was performed in MATLAB to compare the distributions. The null hypothesis for this test states that the distributions are from the same, continuous distribution. Our analysis rejects the null hypothesis at a significance level much less than 0.001%. Thus spectinomycin ΔC_t values between susceptible and spectinomycin resistant E. coli confirmed a significant statistical difference.

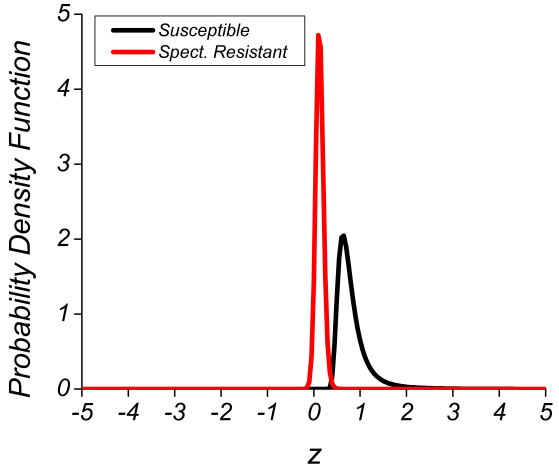

Figure F1: Probability Density Function for statistical comparison of spectinomycin ΔC_t values in Figure 7.3c and 7.3d.

Sequencing of Amplicons

16S rDNA amplicons were purified with a QUIquick PCR Purification Kit (Qiagen) and sequencing was performed at the UC Berkeley DNA Sequencing Facility using a 48-capillary Applied Biosystems 3730xl DNA Analyzer. The forward primer of the PCR reaction was utilized as the sequencing primer and results were analyzed using the Basic Local Alignment Search Tool (BLAST), provided by the National Center for Biotechnology Information (NCBI).

Sequences used for BLAST Determination

EC: Score: 285 E-Value: 2e-74 (215 Bases)
CTGGNAAACTGCCTGATGGAGGGGGATAACTACTGGAAACGGNAGCTAATA
CCGCATAACGNCGCAAGANCAAAGAGGGGGACCTTCCGGCCTCTTGCCATCN
GATGNGCCCAGANGGGANNAGNTAGNAGGTGGGGTAANGGNTCANCNAGNN
NANGATCCCTAGNTGGNCTGAGAGGATGANCAGNCACNNTGNAANTGANAN
ACGGTCCAGA

PF: Score: 226 E-Value: 1e-56 (196 Bases)
ACGGNCGCNAGNTNNCTCTCGTAGGACGTATGCNGNATTAGCGNCCGTTTCC
GAANGNTATCCCCCACTACCAGGNAGATTCCTAGGCTTTACTCACCCGTCCG
CCGNNCTCAAGAGAAGCAAGCTTCTCTCTACCGCTCGANTNGNNTGTGNNAG
GNCTGCCGACAGCGTTCNCTCAGANCCATGANAANAANCT

PV: Score: 129 E-Value 5e-30 (216 Bases)
ATGGGGATCTGCCCGATAGAGGGGGANAACTANTGNAAACGNNAGNTNATA
CCGAATGACGTCNACGGANCAAAGAAGGNGNTCTNCNGANCTTGNNCTATC
NGATGAACNCCTCTGNNANNAGCTAGCAGGTGAGGTAATGGNTCACCNANN
NNANGATCTCTANCTGGACTGAGAGGATGATCAGNCNCANTGGNGCTGANA
CANGGCCCACAG

ML: Score 363 E-Value: 1e-97 (257 Bases)
GGNGAANGGGNGAGTAANANGTGAGTAACCTGNNCTTAACTCTGGGATAAG
CCTGGGAAANTGGGTCTAATANCGGATAGGAGNGTCCACCGNATGGNGGGT
GTTGGAAAGATTTATCGGNTTTGGATGGACTCGNGGNCTATCAGNTTGTTGGT
GAGGTAATGGCTCANCAAGGNGACGACGGGNAGCCGGNCTGAGAGGGTGAC
CGGNCACACTGGGACTGAGACACGGCCCAGANTCCNANNGNANGNAGNAGA

SL: Score: 105 E-Value: 8e-23 (234 Bases)
GACTAANATGCGGGTAANCNGGNNATCNNAAGGGGNNAACAAAAGGAAAA
AGGTGCNAANACCGGATAACAATCGAAACCNCATGGNTTCGTTTNGAAAGG
NGCTTTACNGGGNCNCCGATGNATGGANNCGNGGTGCNTNAGATAGTNGGT
GAGGTAANGGCTCACCAAGGNCACNANGNATANNNGANCTGAGAGGNNGAT
CGGGCANATTGGGACTGACANACGGNCNAAA

MATLAB Script for Simulation of Real-time PCR Antibiogram Threshold

The simulation depicted in Fig. 7.2 was established using parameters for a typical real-time PCR detection system with decreasing polymerase efficiency, depleting reagent concentrations, and the saturation of fluorescent signal. Simulation parameters were optimized using experimental data and the MATLAB code is shown below.

```
close all
clear all
clc

%-------------Initial Growth----------------

doublingtime = 190; %minutes
t = ones(4320,1);
DNA = ones(4320,1);
t(1) = 0;
DNA(1) = 100; %starting copies of DNA/mL

for iter = 1:1:4320;
   t(iter) = iter-1;
   DNA(iter) = DNA(1).*2.^(t(iter)./doublingtime);
end

t;
DNA;

hour = t./60;
day = hour./24;
semilogy(hour, DNA);
%plot(t, DNA)
hold on

s = xlswrite('Main time', hour)
s = xlswrite('Incubated DNA CFU', DNA)

%-------------PCR Simulation----------------
for incubation = 180:180:900;

%incubation = 900

cycle = ones(45,1);
PCRDNA = ones(45,1);
A = ones(45,1);
PCRDNA(1) = DNA(incubation+1);
cycle(1) = 0;
A = (1.45).*A;
ct = 23;
tau = [1.27 1.25 1.23 1.21 1.19 1.17 1.14 1.12 1.10 1.08 1.06 1.055 1.05 1.045 1.04 1.035 1.03 1.025 1.02 1.015 1.01 1.01 1.01 1 1 1 1
1 1 1 1 1 1 1 1 1 1 1 1];
for iter = 1:1:45;
   cycle(iter+1) = iter;
   if iter > ct;
      A(iter) = tau(iter-ct);
      if A(iter) < 1;
         A(iter) = 1;
      end
   end
PCRDNA(iter+1) = PCRDNA(iter).*A(iter);
iter;
PCRDNA(iter+1);
A(iter);

end
tau;
A;
```

```
cycle;
PCRDNA;
maxDNA = max(DNA);
%Norm = (DNA-100000)./maxDNA;

%Arbitrary value of 6.5min selected to extend PCR to ~5hrs and prep of 180min
plot((incubation+13+180+(cycle.*6.5))./60, PCRDNA, 'g');
axis([0 72 0 5e8]);

timecycle(:,1) = (incubation+13+180+(cycle.*6.5))./60

%xlswrite('PCR_DNA_900', PCRDNA)
%xlswrite('Timecycle_900', timecycle)

%plot(cycle, Norm)
%axis([0 45 0 1.05]);

end
```

MATLAB Script used to Perform Two-Sample Kolmogorov-Smirnov Test

A two-sample Kolmogorov-Smirnov test was performed in MATLAB to compare the distributions between the spectinomycin ΔC_t values between susceptible (Fig. 7.3c) and spectinomycin resistant E. coli. (Fig. 7.3d) A significant statistical difference was confirmed validating the concept of the real-time PCR antibiogram.

```
close all;
clear all;
clc

%Susceptible Bacteria
spectmean = 5.985;
spectsigma = 0.128;
negmean = 8.1625;
negsigma = 2.528;

spectmean2 = spectmean^2;
spectsigma2 = spectsigma^2;
negmean2 = negmean^2;
negsigma2 = negsigma^2;

z = [-10:.05:10];

a=sqrt((1/spectsigma2)*(diag(z'*z))+(1/negsigma2));
b=(spectmean/spectsigma2)*z+(negmean/negsigma2);
a2=diag(a*a');
b2=diag(b'*b);

for iter = 1:max(size(z))
   b2a2(iter) = b2(iter)/a2(iter);
   ba(iter) = b(iter)/a(iter);
   a3(iter) = a(iter)^3;
end

c=exp((.5*b2a2)-(.5*((spectmean2/spectsigma2)+(negmean2/negsigma2))));
psi=.5*erfc(-(ba')/sqrt(2));

bc = diag(b'*c);

for iter = 1:max(size(z))
   part1(iter) = bc(iter)/a3(iter);
   part2(iter) = exp(-.5*((spectmean2/spectsigma2)+(negmean2/negsigma2)))/(a2(iter)*pi*spectsigma*negsigma)
end

probdist1=diag(((part1)/(sqrt(2*pi)*spectsigma*negsigma))'*(2*psi-1)')+part2'
```

```
%----------Second Graph

%Spectinomycin Resistant Bacteria
spectmean = 1.256
spectsigma = 0.7955
negmean = 9.986
negsigma = 1.503

spectmean2 = spectmean^2;
spectsigma2 = spectsigma^2;
negmean2 = negmean^2;
negsigma2 = negsigma^2;

%z = [-10:.05:10];

a=sqrt((1/spectsigma2)*(diag(z'*z))+(1/negsigma2));
b=(spectmean/spectsigma2)*z+(negmean/negsigma2);
a2=diag(a*a');
b2=diag(b'*b);

for iter = 1:max(size(z))
   b2a2(iter) = b2(iter)/a2(iter);
   ba(iter) = b(iter)/a(iter);
   a3(iter) = a(iter)^3;
end

c=exp((.5*b2a2)-(.5*((spectmean2/spectsigma2)+(negmean2/negsigma2))));
psi=.5*erfc(-(ba')/sqrt(2));

bc = diag(b'*c);

for iter = 1:max(size(z))
   part1(iter) = bc(iter)/a3(iter);
   part2(iter) = exp(-.5*((spectmean2/spectsigma2)+(negmean2/negsigma2)))/(a2(iter)*pi*spectsigma*negsigma)
end

probdist2=diag(((part1)/(sqrt(2*pi)*spectsigma*negsigma))'*(2*psi-1)')+part2'

figure
hold on
plot(z,probdist1)
plot(z,probdist2)
axis([-5 5 0 5])

kstest2(probdist1,probdist2,1e-130)

output = [z' probdist1 probdist2];

dlmwrite('/Users/Waldie/Desktop/Sepsis Paper/PLoS One/PLoS One Response/Sepsis_Stat.txt',output,'delimiter','\t')
```

REFERENCES:

1. Wang, X. *et al.* Development of an immunochromatographic lateral-flow test strip for rapid detection of sulfonamides in eggs and chicken muscles. *J Agric Food Chem* **55**, 2072–2078 (2007).
2. Kim, Y.-P., Oh, Y.-H. & Kim, H.-S. Protein kinase assay on peptide-conjugated gold nanoparticles. *Biosensors and Bioelectronics* **23**, 980–986 (2008).
3. Oliver, C. *Immunocytochemical Methods and Protocols*. **115**, 327–339 (Humana Press: Totowa, New Jersey, 1999).
4. Hinkley, D. V. On the ratio of two correlated normal random variables. *Biometrika* **56**, 635–639 (1969).

~ FIN ~